

UNIVERSITY OF CALGARY

Intercellular Gap Junction Communication in the Bovine Annulus Fibrosus

by

Russell McWhae

A THESIS

SUBMITTED TO THE FACULTY OF GRADUATE STUDIES
IN PARTIAL FULFILMENT OF THE REQUIREMENTS FOR THE
DEGREE OF MASTER OF SCIENCE

GRADUATE PROGRAM IN BIOMEDICAL ENGINEERING

CALGARY, ALBERTA

FEBRUARY, 2019

© Russell McWhae 2019

Abstract

The intervertebral disc has a complex, anisotropic structure. The annulus fibrosus, the fibrous outer layer of the intervertebral disc, consists of fifteen to twenty-five concentric layers of collagen fibers at alternating orientations. Cells inside and between these lamellae are known to communicate with each other through gap junctions, protein channels that directly couple the membranes of adjacent cells and form interconnected networks that may be used to coordinate a response to mechanical stimuli. These fibroblastic cells fall into three distinct morphologies: spindle-shaped lamellar cells, round lamellar cells, and interlamellar cells. With confocal microscopy methods, gap-junctional intercellular signal propagation between groups of interconnected cells was examined. While the anisotropic microenvironment of the outer annulus was hypothesized to manifest in non-homogenous signal-propagation patterns, it was demonstrated that no clear directional biases or non-homogenous behavior existed among different cell morphologies and orientations; instead, intercellular signal propagation appears to be primarily proximity based.

Keywords: intervertebral disc, gap junctions, intercellular communication, confocal microscopy, bovine model, fluorescence loss in photobleaching

Preface

This thesis is original, unpublished, independent work by the author, R. McWhae.

Acknowledgements

I would like to thank the following individuals for their assistance in the completion of this thesis:

My supervisor, Dr. Neil Duncan, for his guidance, support, and deep knowledge of the intervertebral disc and related topics;

Dr. John Matyas for serving on my committee and for his guidance;

Dr. Arindom Sen for serving on my committee;

Dr. Leping Li and Dr. Paul Salo for participating in my defense;

Dr. Jane Desrochers for showing me laboratory techniques on cow-tail disc-sample preparation and confocal microscopy;

Dragana Ponjevic and May Chung for discussing ideas and providing assistance on laboratory techniques.

I would also like to thank the McCaig Institute and all of its members for providing me with the opportunity to research in such a collaborative community.

Table of Contents

Abstract.....	ii
Preface.....	iii
Acknowledgements	iv
Table of Contents	v
List of Tables	vii
List of Figures and Illustrations	viii
List of Symbols, Abbreviations and Nomenclature	xiii
Chapter One: Introduction	1
1.1 Research Problem	1
1.2 Motivation.....	2
1.3 Hypothesis.....	3
1.4 Overview	4
Chapter Two: Background and Literature Review.....	5
2.1 Anatomy of the Intervertebral Disc	5
2.1.1 Tissue organization.....	5
2.1.2 Cells.....	6
2.2 Disc Biomechanics.....	9
2.3 Mechanotransduction	10
2.4 Gap Junctions.....	13
2.5 Fluorescence Microscopy Techniques to Study Gap Junctions.....	18
2.6 Pathologies of the Disc	21
2.6.1 Aging and degeneration.....	21
2.6.2 Injury.....	22
2.6.3 Spinal deformities.....	23
2.7 Animal Models	23
2.8 Tissue Engineering.....	24
2.9 Summary.....	25
Chapter Three: Intercellular Signal Propagation	26
3.1 Introduction.....	26
3.2 Methods.....	26
3.2.1 Circumferential disc strip preparation.	26
3.2.2 Live-cell assay and cell morphology.	28
3.2.3 Applied tension.	29
3.2.4 One-photon-excitation imaging settings.	32
3.2.5 Two-photon-excitation imaging settings....	34
3.2.6 Image processing.	35
3.3 Results	39
3.3.1 Live-cell assay and cell morphology.	40
3.3.2 1% Strain.	43
3.3.2.1 <i>Non-photobleached control.</i>	43
3.3.2.2 <i>Open gap junctions.</i>	45
3.3.2.3 <i>Blocked gap junctions.</i>	46

<i>3.3.2.4 Overall results, 1% strain.</i>	48
3.3.3 Higher strain levels.....	49
3.3.4 Intercellular signal propagation.....	50
<i>3.3.4.1 Interlamellar cells.</i>	51
<i>3.3.4.2 Round lamellar cells.</i>	54
<i>3.3.4.3 Spindle-shaped lamellar cells.</i>	56
<i>3.3.4.4 Images perpendicular to the imaging plane.</i>	60
<i>3.3.4.5 Overall results, signal propagation.</i>	62
3.3.5 Time effects.	64
3.4 Discussion	68
<i>3.4.1 Live-cell assay and cell morphology.</i>	68
<i>3.4.2 1% strain.</i>	69
<i>3.4.3 Higher strain levels.....</i>	75
<i>3.4.4 Signal propagation.....</i>	80
<i>3.4.5 Time effects.</i>	87
Chapter Four: Conclusions	89
<i>4.1 Introduction.....</i>	89
<i>4.2 Limitations.....</i>	90
<i>4.3 Future Work.....</i>	92
Chapter Five: References	94
Appendix A: FLIP-Image-Set data	109

List of Tables

Table 3.1: Cell morphology categories in the outer bovine annulus fibrosus. Adapted from McMillan (2009)	38
Table 3.2: Overview of experimental data.....	40
Table 3.3: End-point fluorescent intensity values at different strain levels.....	49
Table 3.4: Intra-lamellar signal-propagation patterns among spindle-shaped lamellar cells	57
Table 3.5: Gap-junctional intercellular communication signal-propagation patterns among FLIP image sets from the outer bovine annulus fibrosus	62
Table A.1: FLIP-image-set data.....	109

List of Figures and Illustrations

Figure 1.1: Experimental design flow chart. *See Figure 3.3 for an explanation of the imaging plane orientation.	4
Figure 2.1: Anatomy of the intervertebral disc. Note the alternating collagen-fiber orientation among the concentric annulus fibrosus lamellae, which become interwoven in the circumferential direction. Not to scale.	6
Figure 2.2: Organization of cells in the outer annulus fibrosus. Lamellar cells are aligned in parallel linear arrays with alternating orientations between adjacent layers. Interlamellar cells exists between these layers. (Duncan, 2006).....	8
Figure 2.3: Gap junctions. (Ruiz, 2006)	14
Figure 2.4: Laser-scanning fluorescence-microscopy excitation-laser-beam paths (side view). A) One-photon excitation (also known as confocal laser-scanning microscopy) illuminates an hourglass-shaped path. B) Two-photon excitation illuminates only a precise focal volume, greatly reducing out-of-plane photodamage and also allowing deeper imaging penetration into a specimen. Not to scale.....	21
Figure 3.1: An oxtail. A) As received from the abattoir. B) Exposed disc with two parallel lines drawn about 15 mm apart on the ventral surface.	27
Figure 3.2: Custom tension-loading apparatus for an upright confocal microscope.	30
Figure 3.3: Strip sample orientation on the custom tension-loading apparatus on a confocal microscope (see photo in Figure 3.2). The clamps translate along the positive and negative x-axes to tension the sample. The confocal imaging plane corresponds to the x- y plane. The inset cubic representative volumes show sample layer orientation with respect to the global coordinate system. A) Sample layers parallel to the imaging plane; the positive z-direction (the global z-direction) goes from the inner toward the outer annulus fibrosus. This is considered the default orientation, unless otherwise specified. B) Sample layers perpendicular to the imaging plane; the positive y-direction goes from the inner toward the outer annulus fibrosus.	32
Figure 3.4: Overlapping 10 μm -thick z-slices (side view). Starting with slice 1 on the bottom, slices 2 and 3 are each shifted up in the z-direction by 5 μm . The middle of slice 2 forms the centerline of the image in the z-plane. Each slice maintains its X and Y (horizontal) location, though the black bars representing individual slices here are horizontally staggered for clarity. Fluorescent intensities measured at each of the three z levels were combined according to Equation 3.2.	33
Figure 3.5: Nearest neighbors to the photobleached target cell. Cells that had a majority of their area within about one cell diameter of the bleached cell were considered nearby neighbors (Cells 1, 2 and 3 in this example). Typically, one of these nearest-neighbor cells had a slightly larger fluorescent intensity drop over the six-minute imaging period than the others and was thus named the “nearest neighbor.” Not to scale.....	36

Figure 3.6: Vertical neighbors. The “radial-direction window” applies only to image sets where the imaging plane was perpendicular to the parallel annulus fibrosus lamellae (as in Figure 3.3B). In this diagram, nearby-neighbor cells (see Figure 3.5) to the photobleached target cell are considered to be in the radial direction if they are predominantly in this page’s positive or negative y-direction (vertical) from the photobleached target cell and are thus labelled “vertical neighbors” (Cell 1 in this example). Cells located laterally to the photobleached target cell are outside the radial-direction window. Not to scale.	37
Figure 3.7: Inclusion criteria for intra-lamellar communication within spindle-shaped lamellar cells (for image sets where the imaging plane was parallel to the annulus lamellae as in Figure 3.3A only). Cells 2 and 6 are within the same longitudinal linear array as the bleached cell, and cells 1 and 3–5 are in parallel lateral arrays. At least one cell in both the longitudinal and lateral directions was required for image sets to be analyzed for intra-lamellar communication. Not to scale.	39
Figure 3.8: Typical confocal images of bovine outer annulus fibrosus stained with 5 μM calcein AM. A) Tissue imaged a few hours post slaughter. Note the presence of interlamellar cells with branching processes B) Tissue imaged after overnight freezing, thawing, then staining. Note the lack of cells. Scale bar represents 100 μm	41
Figure 3.9: Distribution of cell morphologies across 135 FLIP image sets of outer bovine annulus fibrosus. Each image set contained up to 9 cells that were considered for fluorescent intensity analysis.	42
Figure 3.10: Z-stack of confocal images from the bovine outer annulus fibrosus. A) Spindle-shaped lamellar cells in linear arrangement. B–F) Images taken at 4.4 μm intervals show the transition to interlamellar cells with branching processes (shown with arrows). Scale bar represents 50 μm	43
Figure 3.11: Non-photobleached control. Fluorescence loss in photobleaching of bovine outer annulus fibrosus cells in the control experimental group without specific target-cell photobleaching, at 1% strain: A) $t = 0$; B) $t = 6$ minutes. C) Fluorescent intensity profiles for labelled cells. Note how all cells retain a normalized intensity around 1.0. Scale bars represent 100 μm	45
Figure 3.12: Open gap junctions. Fluorescence loss in photobleaching of bovine outer annulus fibrosus cells with specific target-cell photobleaching, at 1% strain: A) $t = 0$; B) $t = 6$ minutes. C) Fluorescent intensity profiles for labelled cells. Note the large drops in fluorescent intensity in both the bleached cell and cell 1. Scale bars represent 100 μm	46
Figure 3.13: AGA-blocked gap junctions. Fluorescence loss in photobleaching of bovine outer annulus fibrosus cells with chemical gap-junction blocker AGA and specific target-cell photobleaching, at 1% strain: A) $t = 0$; B) $t = 6$ minutes. C) Fluorescent intensity profiles for labelled cells. Note the large drop in fluorescent intensity in the bleached cell only. Scale bars represent 100 μm	47

Figure 3.14: Effect of specific-target-cell photobleaching and chemical gap-junction blocking with the FLIP experimental protocol in the bovine outer annulus at 1% strain. The relative end-point ($t = 6$ min) fluorescent intensity of the photobleached target cell's nearest neighbor (as defined in Figure 3.5) is shown. Lower values indicate enhanced gap-junctional intercellular communication. Mean-comparison p-values between the different groups are shown on the plot. *As there was no specific target-cell photobleaching in this case, single cells were used as the nearest neighbor (35 cells from eight FLIP image sets).	48
Figure 3.15: Effect of strain on gap junctional intercellular signaling using the FLIP experimental protocol in the bovine outer annulus. The relative end-point ($t = 6$ min) fluorescent intensity of the photobleached target cell's nearest neighbor (as defined in Figure 3.5) is shown. Lower values indicate enhanced gap-junctional intercellular communication. * $p < 0.05$ against the overall mean.	50
Figure 3.16: Interlamellar cells with no nearby neighbors communicating. Confocal images of interlamellar cells in the outer bovine annulus fibrosus before and after 120 FLIP imaging steps where not all nearby neighbor cells to the photobleached target cell appeared to communicate with the target cell: A) $t = 0$; B) $t = 6$ minutes. C) Fluorescent intensity profiles for labelled cells. Note the fluorescent intensity drop in the bleached cell only. Cells 1 through 4 maintained similar fluorescent intensity profiles. As cells 1 and 2 are the only nearby neighbors to the target cell, this image is conservatively classified as having 0 of 2 eligible nearby neighbors involved in intercellular communication. Scale bars represent 100 μm	52
Figure 3.17: Interlamellar cells with all nearby neighbors communicating. Confocal images of interlamellar cells in the outer bovine annulus fibrosus before and after 120 FLIP imaging steps where all nearby neighbor cells to the photobleached target cell appeared to communicate with the target cell: A) $t = 0$; B) $t = 6$ minutes. C) Fluorescent intensity profiles for labelled cells. Note how both nearby-neighbor cells (cells 1 and 2) exhibit drops in fluorescent intensity below all other cells. This image is therefore classified as having 2 of 2 nearby neighbors involved in intercellular communication. Scale bars represent 100 μm	53
Figure 3.18: Round lamellar cells with no nearby neighbors communicating. Confocal images of round lamellar cells in the outer bovine annulus fibrosus before and after 120 FLIP imaging steps where not all nearby neighbor cells to the photobleached target cell appeared to communicate with the target cell: A) $t = 0$; B) $t = 6$ minutes. C) Fluorescent intensity profiles for labelled cells. Note the fluorescent intensity drop in the bleached cell only. Cells 1 through 4 maintained high fluorescent intensities. As cell 1 is the only nearby neighbor to the target cell, this image is conservatively classified as having 0 of 1 nearby neighbor involved in intercellular communication. Scale bars represent 100 μm	55

Figure 3.19: Round lamellar cells will all nearby neighbors communicating. Confocal images of round lamellar cells in the outer bovine annulus fibrosus before and after 120 FLIP imaging steps where all nearby neighbor cells to the photobleached target cell appeared to communicate with the target cell: A) t = 0; B) t = 6 minutes. C) Fluorescent intensity profiles for labelled cells. Note how all three nearby-neighbor cells (cells 1, 2 and 3) exhibit drops in fluorescent intensity below all other cells. This image is therefore classified as having 3 of 3 nearby neighbors involved in intercellular communication. Scale bars represent 100 μ m.....	56
Figure 3.20: Spindle-shaped lamellar cells with only a fraction of nearby neighbors communicating. Confocal images of spindle-shaped lamellar cells in the outer bovine annulus fibrosus before and after 120 FLIP imaging steps where not all nearby neighbor cells to the photobleached target cell appeared to communicate with the target cell: A) t = 0; B) t = 6 minutes. C) Fluorescent intensity profiles for labelled cells. Note how cell 2 has a large drop in fluorescent intensity compared to all other cells. As cells 1, 2, and 3 are nearby neighbors to the target cell, this image is classified as having 1 of 3 nearby neighbors involved in intercellular communication, in the longitudinal direction only. Scale bars represent 100 μ m.....	58
Figure 3.21: Spindle-shaped lamellar cells with all nearby neighbors communicating. Confocal images of spindle-shaped lamellar cells in the outer bovine annulus fibrosus before and after 120 FLIP imaging steps where all nearby neighbor cells to the photobleached target cell appeared to communicate with the target cell: A) t = 0; B) t = 6 minutes. C) Fluorescent intensity profiles for labelled cells. Note how all three nearby-neighbor cells (cells 1, 2, and 3) exhibit clear drops in fluorescent intensity below most other cells. This image is therefore classified as having 3 of 3 nearby neighbors involved in intercellular communication, in both longitudinal and lateral directions. Scale bars represent 100 μ m.....	59
Figure 3.22: Radial-direction communication. Confocal images of spindle-shaped lamellar cells in the outer bovine annulus fibrosus before and after 120 FLIP imaging steps when the imaging plane is perpendicular to the disc lamellae (per Figure 3.3B): A) t = 0; B) t = 6 minutes. C) Fluorescent intensity profiles for labelled cells. Note how cells 1 and 2 show the largest drops in fluorescent intensity, suggesting intercellular communication in the radial disc direction (normal to parallel lamellae; see Figure 3.6). Scale bars represent 100 μ m.....	61
Figure 3.23: Gap-junctional intercellular communication signal propagation in the outer bovine annulus fibrosus. For each of the 111 FLIP image sets taken at different strain levels, the fraction of nearby neighbor cells (per Figure 3.5) appearing to communicate with the photobleached target cell was compared to the total number of communication-eligible nearby neighbor cells.	63
Figure 3.24: Radial-direction signaling results. For each of 17 FLIP image sets at 1% strain, the fraction of communication-eligible nearby vertical neighbor cells (per Figure 3.6) appearing to communicate with the target cell is compared to the total number of nearby vertical neighbor cells.	64

Figure 3.25: Time effects on gap-junctional intercellular communication in IVD samples loaded in static tension. Each point represents one FLIP image set, and FLIP image sets from similar disc strips are connected by lines (e.g. 9 FLIP image sets of different cell clusters were taken in IVD specimen “May9A” at 1% strain, with increasing time spent in tension). End-point fluorescent intensities for nearest neighbor cells to the photobleached target cell are shown. Lower values indicate enhanced gap-junctional intercellular communication. A) 1% strain B) 5% strain C) 10% strain D) 15% strain E) 20% strain F) 25% strain..... 67

List of Symbols, Abbreviations and Nomenclature

Symbol	Definition
AGA	18 α -Glycyrrhetic acid
ε	Strain
FRAP	Fluorescence recovery after photobleaching
FLIP	Fluorescence loss in photobleaching
f_x	Normalized fluorescent intensity, at time x
$f_{t=x, z=n}$	Fluorescent intensity, at time x , for z-slice n
IP3	Inositol trisphosphate
IVD	Intervertebral disc
L_0	Initial sample length
ΔL	Change in sample length
MAPK	Mitogen-activated protein kinase
NF- κ B	Nuclear factor kappa-light-chain-enhancer of activated B cells
NO	Nitric oxide
PKA	Protein kinase A
ROI	Region of interest

Chapter One: Introduction

1.1 Research Problem

With a lifetime prevalence of 60–90% (Frymoyer, 1988), low back pain is a leading disability with major economic impact: up to 32% of back-pain patients have not returned to work after one month (Wynne-Jones et al., 2014). Though exact numbers are difficult to calculate, the economic burden resulting from low back pain in the United States alone has been estimated in the tens to hundreds of billion dollars annually (Dagenais, Caro, & Haldeman, 2008). While low back pain can originate from a number of sources within the anatomical structures of the spine such as nerves, muscle, bones, and the intervertebral disc (IVD) (Allegri et al., 2016), degeneration of the intervertebral disc is a prevalent source of low back pain (Cheung et al., 2009; De Schepper et al., 2010; Kelsey, White, & Sci, 1980; Luoma et al., 2000), though a clear cause of degeneration initiation and progression remains elusive, owing to the numerous, interdependent factors affecting intervertebral disc regulation.

Mechanical loading is known to affect extracellular matrix turnover in connective tissue, such as in tendon and bone, where mechanical loading promotes collagen synthesis (Kjær, 2004; Kjær et al., 2006, 2009). Cells within the IVD are similarly regulated by mechanical and chemical stimuli, and improper regulation can initiate a positive feedback loop of IVD degeneration (Vergroesen et al., 2015). IVD degeneration corresponds to radiographic signs such as decreased signal intensity, disc-height narrowing, disc-bulging, herniations, osteophytes and end-plate irregularities (Battié, 2006).

Cells in connective tissue such as bone, tendons, and ligaments are connected to each other through a network of transmembrane channels called gap junctions (Neidlinger-Wilke et al., 2014). Ions can pass through these channels, which could be a means of establishing a coordinated response among interconnected cells (Desrochers & Duncan, 2012). Extreme

mechanical loading and aging have been shown to affect this intercellular signaling (Desrochers & Duncan, 2012; Gruber, Ma, Hanley, Ingram, & Yamaguchi, 2001; Maeda et al., 2012; Maeda & Ohashi, 2015). The goal of this study is to further understand cell-to-cell signaling in the healthy annulus fibrosus and the response to mechanical stimuli. Confocal microscopy with live-cell staining will be used to examine the propagation of intercellular signals. Understanding communication between interconnected cells in the normal state may help elucidate the biomechanical process of IVD degeneration.

1.2 Motivation

Previous work has looked at intercellular communication across gap junctions in live bovine and human tissue using fluorescence recovery after photobleaching (FRAP) techniques (Desrochers & Duncan, 2012; McMillan, 2009); however, a complementary technique known as fluorescence loss in photobleaching (FLIP) has yet to be applied to the intervertebral disc. FLIP can be used to track the mobility of tagged molecules between cells (Maeda et al., 2012; Maeda, Pian, & Ohashi, 2017; Maeda & Ohashi, 2015), and it will be applied here to examine signal propagation within the cells of the IVD. Tendon has demonstrated non-homogeneous intercellular signal propagation: the dominant direction of intercellular signaling was along the main longitudinal tissue axis, where rectangular cells are lined up in parallel rows, but not laterally between adjacent rows (Maeda et al., 2012). Cells in the IVD are organized in a unique, anisotropic microenvironment consisting of concentric layers of parallel fibers (see Figure 2.2), so signal propagation among cells both within and between these layers will be investigated to see if there are any patterns or non-homogeneities. Prior work had found extreme mechanical loading to disrupt gap-junctional intercellular signaling (Desrochers & Duncan, 2012), though the effect of moderate load has yet to be investigated.

1.3 Hypothesis

It is hypothesized that cells in the intervertebral disc communicate with each other along linear arrays but not between adjacent rows or layers. The objective of this study is to measure gap-junctional intercellular signal propagation among interconnected cells of the outer annulus fibrosus of the intervertebral disc. This will be investigated using the fluorescence loss in photobleaching (FLIP) technique on a confocal and multi-photon microscope with a bovine model. Specifically, this study will attempt to examine the following aims:

- Determine the effect of low, moderate, and high mechanical load on gap-junctional intercellular signaling in the outer annulus fibrosus
- Identify if there are patterns or directionality to intercellular-signal-propagation patterns among interconnected networks of outer annulus fibrosus cells

A flow chart detailing the experimental design can be found in Figure 1.1.

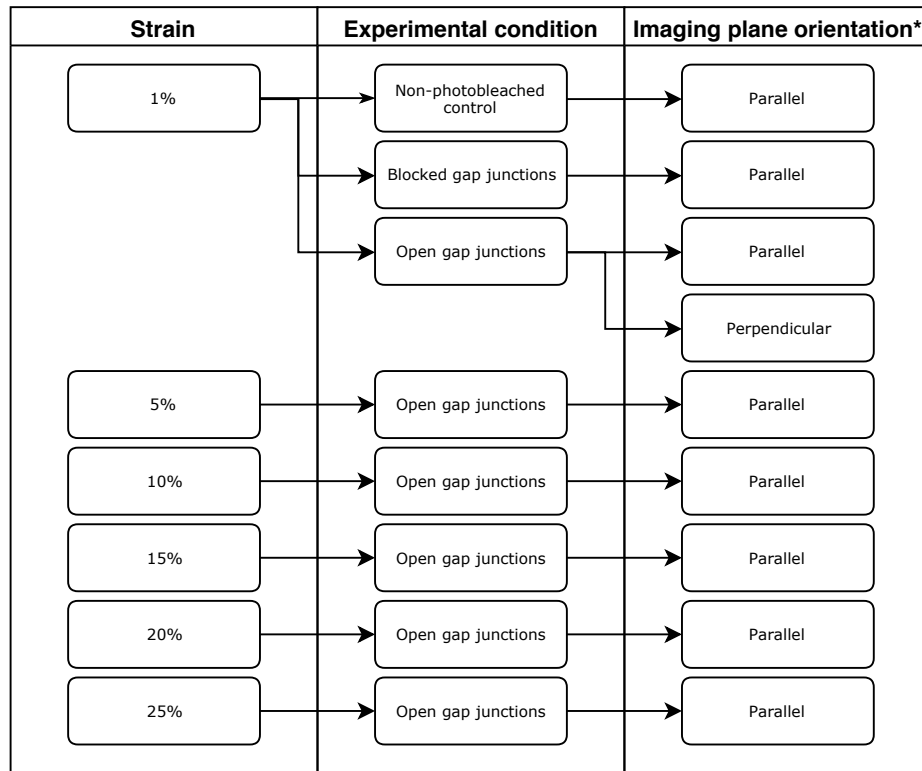


Figure 1.1: Experimental design flow chart. *See Figure 3.3 for an explanation of the imaging plane orientation.

1.4 Overview

After this introduction, Chapter Two provides background information and a literature review on the current understanding of gap-junctional intercellular communication in the intervertebral disc. Chapter Three details the experiments performed in this study, and Chapter Four summarizes its conclusions and limitations. References and appendices follow.

Chapter Two: Background and Literature Review

2.1 Anatomy of the Intervertebral Disc

2.1.1 Tissue organization.

Joining adjacent bony vertebrae, intervertebral discs (IVDs) are fibro-cartilage connective tissue structures that allow motion between vertebrae and cushion the spine. The IVD has three different functional regions: the nucleus pulposus, the annulus fibrosus, and a superior and inferior cartilaginous endplate. The inner, gelatinous nucleus pulposus is surrounded by the tough, fibrous annulus fibrosus.

The nucleus pulposus is 70% to 90% water (Cramer, 2014). An irregular network of collagen type II and elastin fibers support a water and proteoglycan matrix in the nucleus pulposus, similar to that found in hyaline cartilage (Olsen, Kang, Vo, & Sowa, 2018). Aggrecan is the most abundant proteoglycan, and a number of others are present in smaller quantities (Melrose & Roughley, 2014). Negatively charged keratan and chondroitin sulfate chains in aggrecan bind positively charged Na⁺ ions, creating an unbalance of cations and consequently an osmotic swelling pressure inside the nucleus (Cortes & Elliott, 2014).

The annulus fibrosus is composed of 15 (posterior side) to 25 (lateral side) concentric, interwoven layers of type I collagen in alternating orientations (Figure 2.1). This structure enables the disc to withstand torsional stresses (Mwale, 2014). The fiber-direction angle increases from about 60° relative to the spinal axis in the outer annulus fibrosus to 90° in the inner annulus fibrosus (Cortes & Elliott, 2014). Between individual layers, space called the interlamellar septae contains linking elements, ensuring cohesion between adjacent layers (Bron, Helder, Meisel, Van Royen, & Smit, 2009; Pezowicz, Robertson, & Broom, 2006). The annulus fibrosus can be further divided into two regions, the outer and inner annulus, where cells can be characterized by different phenotypic markers: fibroblastic cells in the outer region and

chondrocyte-like cells in the inner region (Ghannam et al., 2017; van den Akker et al., 2017). The fibroblastic cells primarily produce type I collagen as well as types III, V, and VI (Ghannam et al., 2017), with type I collagen exclusively forming the outside edge of the annulus (Eyre & Muir, 1976). Collagen fibers in the outer annulus are deeply anchored into the bony vertebral endplates, while inner fibers gradually merge into the cartilaginous endplates (Newell et al., 2017).

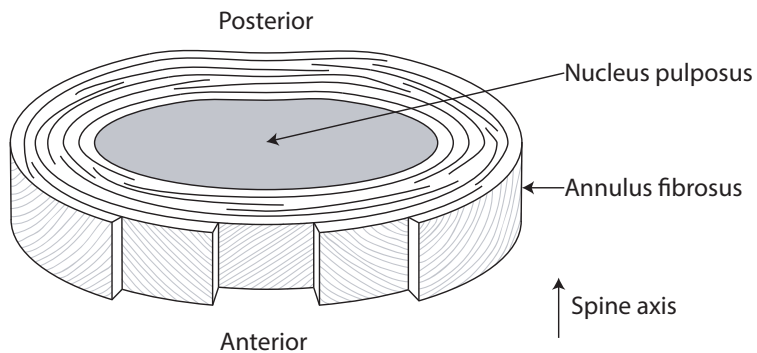


Figure 2.1: Anatomy of the intervertebral disc. Note the alternating collagen-fiber orientation among the concentric annulus fibrosus lamellae, which become interwoven in the circumferential direction. Not to scale.

The cartilaginous endplates are thin layers of hyaline cartilage between the bony vertebral endplates and the nucleus pulposus. They measure between 0.1–1.6 mm thick and are thickest in the center of the nucleus pulposus while terminating before the outer annulus fibrosus (Ghannam et al., 2017; Newell et al., 2017). The endplates have the important role of providing nutrients and oxygen to the avascular disc tissues via diffusion (S.R.S. Bibby & Urban, 2004).

2.1.2 Cells.

Cells in the disc are relatively sparse, making up only 1% of the disc by volume, yet have the notable role of being responsible for extracellular matrix synthesis and breakdown (Susan R.S. Bibby, Jones, Lee, Yu, & Urban, 2001). Cell density in adult human annulus fibrosus tissue ranges from 3000–9000 cells/mm³, which is much lower than the 16,000–60,000 cells/mm³ in

hyaline cartilage (Torre, Mroz, Bartelstein, Huang, & Iatridis, 2018). Cell density in the nucleus is 4000 cells/mm³ or less (Kandel, Santerre, Massicotte, & Hurtig, 2014). With low density and also low metabolic demands, the disc cells have a limited capacity to repair the extracellular matrix beyond homeostatic turnover (S. M. Richardson, Freemont, & Hoyland, 2014). Cells are highly involved in disc degeneration (Adams & Roughley, 2006; Olsen et al., 2018) and undergo many biologic changes including alterations in cell type, density, and phenotype during aging and degeneration (Zhao, Wang, Jiang, & Dai, 2007). Though the cause is unclear, a reduction in nutrient delivery is thought to drive progressive disc degeneration (S. M. Richardson et al., 2014).

Different cell morphologies exist in the annulus fibrosus: cells in the outer annulus are mostly fibroblasts with fusiform bodies, while cells in the inner annulus are mostly fibrochondrocytes with spherical shapes; additionally, cellular processes among cells in the outer annulus are long and thin at the outside surface of the disc yet become shorter deeper inside the outer annulus and ultimately disappear near the border to the inner annulus (Bruehlmann, Rattner, Matyas, & Duncan, 2002; Hsieh & Twomey, 2010). Cells toward the extremity of the outer annulus are interconnected via their long processes, forming a communication network; however, deeper cells without interconnected processes have no apparent intercellular connections (Bron et al., 2009). Cell density drops toward the inner annulus (Hastreiter, Ozuna, & Spector, 2001).

In the annulus fibrosus, cells inside the concentric collagen layers are aligned within the collagen fibrils in groups of up to twelve cells in a linear array (Duncan, 2006). Cells also exist in the interlamellar septae and have a flattened morphology, though their relationship to inner and outer annulus fibrosus cells is unclear (Hsieh & Twomey, 2010). Figure 2.2 shows the organization of cells in the outer annulus fibrosus.

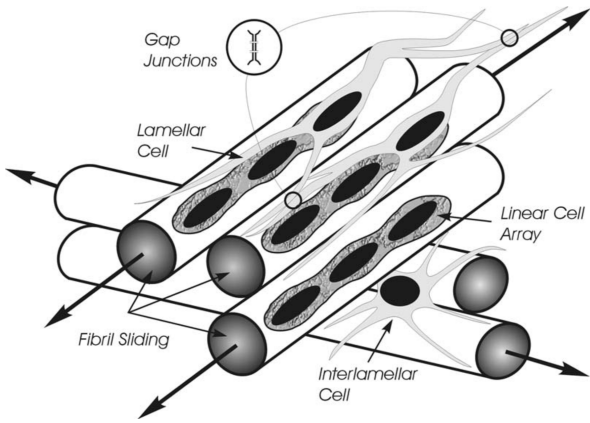


Figure 2.2: Organization of cells in the outer annulus fibrosus. Lamellar cells are aligned in parallel linear arrays with alternating orientations between adjacent layers. Interlamellar cells exists between these layers. (Duncan, 2006)

There has been some debate as to the embryological origin of cells in the nucleus pulposus. After the formation of the three primary germ layers (ectoderm, mesoderm, and endoderm) during gastrulation of the human embryo, the notochord forms (Ghannam et al., 2017). Nucleus pulposus cells are largely thought to be of notochordal origin, yet some argue that they come from peri- or extra-notochordal tissues (Risbud, Schaer, & Shapiro, 2010). These cells decrease after birth and disappear almost entirely within the first decade in humans (Pazzaglia, Salisbury, & Byers, 1989), while smaller, round chondrocyte-like cells, thought to be of a different origin, increase in number (Sive et al., 2002). The origin of nucleus pulposus cells has implications for tissue engineering as residual notochordal cells have been considered for conducting *in vivo* repairs (Hunter, Matyas, & Duncan, 2003). It has been argued that degenerative disc disease is not simply due to the selective loss of only notochordal cells (Risbud et al., 2010).

Following notochord formation in the human embryo, paraxial mesoderm cells form the bilateral somites, which in turn divide into the ventromedial sclerotome and the dorsolateral dermomyotome (Ghannam et al., 2017). The annulus fibrosus and cartilaginous endplates are of

mesenchymal origin, deriving from these sclerotomes (Christ & Wilting, 1992; Risbud & Shapiro, 2012). The notochord and sclerotomes together form the origin of the intervertebral disc (Colombier, Clouet, Hamel, Lescaudron, & Guicheux, 2014; Ghannam et al., 2017). Certain cells from the sclerotomes migrate toward the notochord and form the perinotochordal sheath, a precursor to the vertebral bodies (Ghannam et al., 2017). The vertebral bodies subsequently undergo chondrogenesis, and cells in the outer annulus fibrosus differentiate into the fibroblasts found within the highly organized, parallel lamellae of the outer annulus (Ghannam et al., 2017).

Cells in the IVD have relatively low nutrient demand due to the nearly avascular nature of IVDs. In vivo, nutrients and waste removal are provided by blood vessels in the vertebrae bordering the cartilaginous endplates (Grunhagen, Wilde, Soukane, Shirazi-Adl, & Urban, 2006). Locally, extracellular oxygen and pH regulate individual cell metabolism in IVDs (Grunhagen et al., 2006). It was found that a lack of glucose reduced cell viability with or without oxygen, though glucose deprivation is unlikely to occur *in vivo* without a corresponding drop in oxygen and pH (S.R.S. Bibby & Urban, 2004). With aging, sclerosis and gradual calcification of the cartilaginous endplates can disrupt IVD nutrition, thereby inhibiting extracellular-matrix synthesis and causing apoptosis (González Martínez et al., 2017).

2.2 Disc Biomechanics

Within spinal motion segments (one IVD attached to a superior and inferior vertebrae), each IVD provides six degrees of freedom and is subject to complex loading and deformation schemes, with different behaviour at different vertebral levels (Li et al., 2009). As a motion-permitting joint between two bony vertebrae, the intervertebral disc is subject to compression, flexion/extension, lateral bending, and torsion (Cortes & Elliott, 2014). Discs are constantly under load, even in relaxed, supine positions (Nachemson, 1966).

From supporting the weight of the upper body, a major form of physiological loading in the spine is axial compression. Compressive loads are transmitted predominantly through the vertebrae and intervertebral discs depending on the posture: 100% of the load is transmitted through the discs while sitting in an erect posture, but up to 16% of this load can be transmitted in the zygapophysial joints while standing (Adams & Hutton, 1980). The immediate response of the disc to compressive load is incompressible fluid pressurization, wherein the interstitial fluid inside the nucleus pulposus supports a fraction of the applied load, and radial expansion of the nucleus pulposus tensions the annulus fibrosus in the circumferential direction (Cortes & Elliott, 2014; Hsieh & Twomey, 2010). Hydrostatic pressurization is thus the dominant physiological loading mechanism among the nucleus, while biaxial tensile strain and shear (both within and between lamellae) are dominant in the annulus (Lotz & Hsieh, 2014; Neidlinger-Wilke et al., 2014).

Whole-body mechanical loads on the IVD affect cells in different regions of the IVD asymmetrically. There is a load-redistribution mechanism as tissue-level macroscale strain translates to cellular-level microscale strain (Desrochers & Duncan, 2010). Due to the linear arrangement of lamellar cells in the outer annulus fibrosus, these cells appear to be protected from tensile strains, yet their connected processes are subject to shear loading due to the shearing between collagen fibrils, suggesting a complex load-transduction mechanism in annular cells (Duncan, 2006). The magnitude, frequency, and duration of loads within the intervertebral disc affect cell function (Lotz & Hsieh, 2014), which will be discussed in the following section.

2.3 Mechanotransduction

Cells in many types of tissue are known to sense and respond to physical stimuli such as stretch, hydrostatic pressure, compression, and shear in their local microenvironment and dynamically adapt by translating these stimuli into biochemical signals that modify their

behavior (Butcher, Alliston, & Weaver, 2009). This process is termed mechanotransduction and generally involves three coupled procedures: mechanosensing, activation of signal-transduction pathways, and effector-cell responses (Neidlinger-Wilke et al., 2014). Mechanotransduction has been well studied in chondrocytes (C. Chen, Tambe, Deng, & Yang, 2013; Guilak et al., 1994), bone (Uda, Azab, Sun, Shi, & Pajevic, 2017), and tendon (Kjær, 2004), and has lately received attention in the intervertebral disc (González Martínez et al., 2017; Hsieh & Twomey, 2010; Lotz & Hsieh, 2014; Neidlinger-Wilke et al., 2014; Tsai, Cheng, Chen, & Lai, 2014; K. T. Weber et al., 2015).

Cells sense mechanical stimuli in their surrounding microenvironment, both the extracellular matrix and adjacent cells, through complex sensing mechanisms. Such mechanisms are thought to be: mechanically activated ion channels, modified electrical potentials, receptors linked to G proteins, receptor tyrosine kinases, and integrins, among others, including perhaps as yet unknown factors (González Martínez et al., 2017; Neidlinger-Wilke et al., 2014; Tsai et al., 2014). These mechanosensors then activate intracellular signaling pathways including: mitogen-activated protein kinase (MAPK), nuclear factor kappa-light-chain-enhancer of activated B cells (NF-κB), protein kinase A (PKA), inositol trisphosphate (IP₃), nitric oxide (NO), and others (Neidlinger-Wilke et al., 2014; Tsai et al., 2014).

Downstream, these pathways can affect protein synthesis, cytoskeletal organization, and even apoptosis (Shivashankar, Sheetz, & Matsudaira, 2015; Tsai et al., 2014). Mechanical stimulation is thus critical for tissue homeostasis, especially the development and maintenance of the cellular cytoskeleton and extracellular matrix in load-bearing connective tissue. In tendon, physiological mechanical loading promotes collagen synthesis, an important structural protein (Kjær et al., 2006; Maeda, Shelton, Bader, & Lee, 2007). In bone, a sensor-effector paradigm is commonly proposed wherein osteocytes relay mechanical signals to osteoblasts (for bone

formation) and osteoclasts (for bone resorption) (Jacobs, Temiyasathit, & Castillo, 2010). Improper mechanotransduction has been implicated in diseases including cardiomyopathies and cancer (Jaalouk & Lammerding, 2009) as well as degeneration in the intervertebral disc (Zhao et al., 2007).

Mechanical loading plays an important role in intervertebral disc's extracellular matrix assembly during initial development: pressure from the nucleus pulposus generates stress-fiber formation in annular fibroblasts, which in turn help pattern the complex lamellar structure of the annulus (Hayes, Benjamin, & Ralphs, 1999). In the mature disc, load magnitude, frequency and duration affect the disc cells' mechanobiologic response (Lotz & Hsieh, 2014; Sowa et al., 2011). Generally, physiological loading conditions (for pressure loads in the nucleus: <1 MPa magnitude, <3 Hz frequency, and <24-hour duration; and for stretch loads in the annulus: <1% strain, 1 Hz, <48 h) induce an anabolic response among disc cells, while non-physiological conditions are catabolic (Lotz & Hsieh, 2014). Anabolic responses include an increased expression of anabolic matrix proteoglycans, including collagen I and aggrecan, among others (J. Chen, Yan, & Setton, 2004; Wenger et al., 2005). Catabolic responses include decreased proteoglycan production, increased nitric oxide (NO) production, and enhanced matrix metalloproteinase-3 (a matrix-degrading protein) expression (Rannou et al., 2003; Sowa et al., 2011). Mechanobiologic interactions in the disc are likely involved in age-related degenerative changes (Lotz & Hsieh, 2014; Neidlinger-Wilke et al., 2014).

Calcium ions are known to be particularly important in mechanotransduction: in bone, cartilage, tendon and ligament, cells release calcium ions internally in response to mechanical perturbation (Adachi, Aonuma, Ito, et al., 2009; Elfervig, Minchew, Francke, Tsuzaki, & Banes, 2001; Guilak et al., 1994; S.-K. Han, Wouters, Clark, & Herzog, 2012; W. M. Han et al., 2014; Yellowley, Li, Zhou, Jacobs, & Donahue, 2000). Calcium ions reach a peak intracellular

concentration as an initial response to mechanical stimuli that leads to downstream molecular activity such as specific gene expression (Elfervig et al., 2001; Pingguan-Murphy, Lee, Bader, & Knight, 2005). Calcium ions are a ubiquitous secondary messenger, which affect many different intracellular functions (Berridge, Bootman, & Roderick, 2003).

Loading schemes, either static or dynamic, and temperature can affect calcium signaling. Under identical loading conditions, calcium-ion responses in chondrocytes are faster and more intense at 37°C relative to 21°C (S.-K. Han et al., 2012). Dynamic compressive loading schemes produced different metabolic responses in chondrocytes compared to static compression (Pingguan-Murphy et al., 2005); additionally, a desensitization mechanism exists whereby cells become less sensitive to mechanical stimuli with increasing loading cycles (J. F. Weber & Waldman, 2014).

Microenvironment is important in cellular mechano-regulation. Early studies found cultured chondrocytes, enzymatically removed from their host cartilage, to demonstrate transient increases in intracellular calcium ion concentration in both a cell deformed by a micropipette and its surrounding neighbors, suggesting intercellular signal propagation via functional gap junctions, with intracellular calcium concentration reaching a peak in the first 3–5 s (Guilak et al., 1994). Later work examined the effect of different cellular microenvironments on signaling, finding differences in calcium-signaling activity in meniscus fibrochondrocytes between native tissue, cells cultured on silicone membranes, and nanofibrous scaffolds (W. M. Han et al., 2014), highlighting the importance of physiological microenvironments in accurately understanding cellular mechanobiologic behavior.

2.4 Gap Junctions

Gap junctions (Figure 2.3) are connections between two adjacent cells formed by protein channels spanning across their plasma membranes (Bruzzone, White, & Paul, 1996). Multiple

gap junctions usually cluster together in similar regions, forming what are called gap junction plaques (Goldberg et al., 1996; M. U. Hussain, 2014b). Six connexin protein subunits oligomerize to form a connexon hemi-channel inside a single cell, which then moves to the cell surface and docks with a connexon hemi-channel from an adjacent cell (Goodenough & Paul, 2009). Once docked, channels open and create hydrophilic pathways between cell interiors (Bao, Sachs, & Dahl, 2004). It has also been suggested that non-docked hemi-channels could be involved in intra- and extracellular signaling (Bray et al., 2005; Goodenough & Paul, 2003). Connexin subunits are named according to their predicted molecular mass in kDa; for example, connexin 26 has a molecular weight of 26 kDa (Kumar & Gilula, 1996).

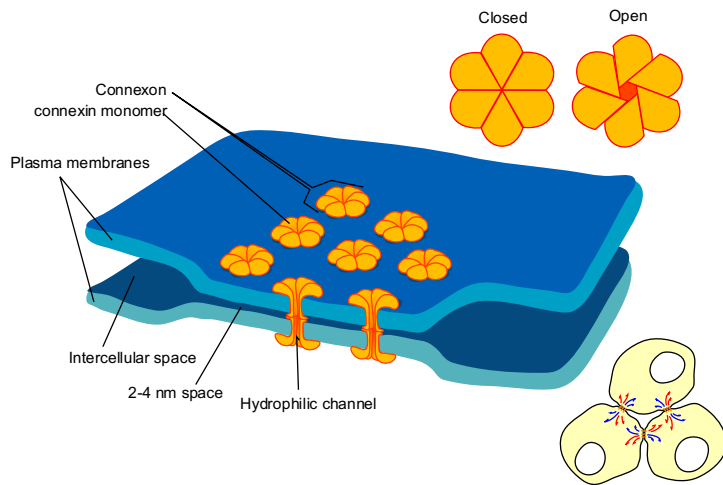


Figure 2.3: Gap junctions. (Ruiz, 2006)

Connexin 43 is an important gap-junction protein in the bovine and human intervertebral disc (Desrochers & Duncan, 2012; Gruber et al., 2001; McMillan, 2009). It has been found on both cell bodies and processes in cells throughout the annulus fibrosus, including in isolated cells that did not form physical connections with neighboring cells, making the exact location of functional gap junctions unclear (Bruehlmann et al., 2002; Duncan, 2006). Connexin 43 was first found in myocardial gap junctions (Bruzzone et al., 1996) and has been extensively studied in

cardiac tissue (Salameh & Dhein, 2013; Severs et al., 2004) and other mechanically sensitive tissue such as tendon and bone (Kjær, 2004). Connexin 43 is the most abundant connexin in the human body (Evans & Martin, 2002; M. U. Hussain, 2014c; Laird, 2006) and has been found to exhibit mechanosensitive expression, particularly upregulation in response to mechanical stimulation, in cells such as tenocytes (Maeda et al., 2012, 2017; Maeda & Ohashi, 2015) and endothelial cells (DePaola et al., 1999). Mutations in the gene encoding connexin 43 can cause diseases such as oculodentodigital dysplasia when autosomal dominant; however, patients carrying this mutation are considerably less ill than should be predicted on account of the ubiquity of connexin 43 (Laird, 2006).

In response to mechanical perturbation, gap junctions are not directly involved in signal transduction; however, they can relay such signals to interconnected neighboring cells (Guilak et al., 1994). A disruption in gap-junction signaling could therefore occur anywhere on the signaling pathway from initial mechanosensing up to the gap junction channel.

Channels may open or close and allow the free passage of small molecules up to 1 kDa in size such as ions and other metabolites when open (Bennett & Verselis, 1992; Bruzzone et al., 1996). This enables the sharing of metabolic demands across interconnected cells, thereby buffering the spatial gradients of nutrients and signaling molecules than can diffuse through gap junctions (Goodenough & Paul, 2009). Gating of the central pore can be regulated by rapid changes in voltage, pH, and calcium levels between transjunctional cells (Goodenough, Goliger, & Paul, 1996). Regulation of channel opening occurs on multiple time scales: immediate, where individual channels may be opened or made more likely to open, and longer term, where the number of channels may be altered by changing channel protein synthesis, assembly, posttranslational modification, and degradation rates (Goodenough & Paul, 2009). The turnover

of connexins is quite fast: their half-life does not exceed a few hours (Goodenough & Paul, 2009; M. U. Hussain, 2014a).

Gap junctional intercellular communication in connective tissue is frequently studied using confocal fluorescence microscopy. Fluorescent stains can be selected that label the entire cytosol of live cells such as calcein AM (Chi, Rattner, & Matyas, 2004; Chi, Rattner, Sciore, Boorman, & Lo, 2005; Desrochers & Duncan, 2012; Maeda et al., 2012; Maeda & Ohashi, 2015; Maeda et al., 2017; McMillan, 2009; Suadicani, Flores, Urban-Maldonado, Beelitz, & Scemes, 2004; Sugawara et al., 2011), or may be selected to label more specific molecular targets such as calcium ions with Fluo-3 (Guilak et al., 1994) or Fura Red and Fluo-4 (Adachi, Aonuma, Taira, Hojo, & Kamioka, 2009), or nitric oxide with DAR-4M (Vatsa, Smit, & Klein-Nulend, 2007).

Gap junctions and intercellular signaling have been studied in many forms of connective tissue: tendon (Banes et al., 1999; Maeda et al., 2012, 2017; Maeda & Ohashi, 2015), bone (Adachi, Aonuma, Ito, et al., 2009; Ishihara et al., 2012; Lu, Huo, Park, & Guo, 2012; Sugawara et al., 2011; Taylor et al., 2006; Yellowley et al., 2000), cartilage (Guilak et al., 1994; Mayan et al., 2015), ligament (Bray et al., 2005; Chi et al., 2005), and the intervertebral disc (Desrochers & Duncan, 2012; Gruber et al., 2001; Hunter, Matyas, & Duncan, 2004). It has been suggested that the networks formed by gap junctions enable cells inside connective tissue to effect a coordinated response to external stimuli such as mechanical loading (Desrochers & Duncan, 2012; Gruber et al., 2001), though the nature of signal propagation between upstream and downstream cells in the IVD remains unclear.

Of particular interest to the current study is the work of Maeda et al. (2012) and Maeda and Ohashi (2015). Maeda et al. (2012) developed a fluorescence loss in photobleaching (FLIP) technique with confocal microscopy to quantify rates of gap-junction signaling in rat tendon, developing a permeability parameter that quantified gap-junction communication. They found

that a static 1 N tensile load had no effect on gap junction permeability over a time period of 10 minutes, while the same load applied for 1 hour significantly reduced gap junction permeability, suggesting that tenocyte gap-junction permeability is directly regulated by mechanical loading when applied over a long enough time period. Connexin 43 was found to be the dominant connexin involved in gap junction communication according to immunofluorescence, and it demonstrated suppressed protein expression with the corresponding drop in gap-junction permeability at 1 hour, suggesting increased turnover of gap junctions in response to the disrupted communication. Interestingly, connexin 43 mRNA was upregulated, which perhaps indicated a cellular response of attempting to re-establish functional gap junctions at a subsequent time. Another finding was that the dominant direction of intercellular signaling in tenocytes was along the main longitudinal axis of the tendon, where rectangular cells were lined up in close parallel rows within collagen fibers, but not laterally between adjacent parallel rows.

Ligament also demonstrated a similar bipolar expression of functional gap junctions: cells in rabbit medial collateral ligament were found to express connexin-43 gap junctions only in areas of close cell-cell contact, where they formed non-uniform rows (Chi et al., 2005). This bipolarity was lost when the same cells were cultured outside their native microenvironment (Chi et al., 2005), further highlighting the importance of microenvironment in studying gap-junction intercellular communication.

Maeda and Ohashi (2015) performed a FLIP study in rabbit tendon, using applied tensile strains of 0%, 4% (a physiological amplitude), and 8% (beyond physiological amplitude). They found an increase in gap-junction intercellular communication at 4% strain relative to 0%, suggesting an increase in gap-junction permeability via tenocyte-mechanotransduction events at physiological strain levels, and an inhibition of gap-junction intercellular communication at 8%

strain, suggesting mechanical disruption of gap-junction functioning. Together, these results demonstrated that the magnitude of tensile strain affects gap-junction mechano-regulation, an effect that the current study aims to examine in the intervertebral disc.

2.5 Fluorescence Microscopy Techniques to Study Gap Junctions

Two confocal microscopy methods are used to study the motion of fluorescently labelled molecules through gap junctions between interconnected cells: fluorescence recovery after photobleaching (FRAP) and fluorescence loss in photobleaching (FLIP) (Ishikawa-Ankerhold, Ankerhold, & Drummen, 2012). FRAP and FLIP experiments are run on confocal microscopes using one-photon-excitation laser-scanning imaging techniques, also known as confocal laser-scanning microscopy.

Confocal laser-scanning microscopy is a form of fluorescence microscopy. In fluorescence microscopy a fluorochrome (or fluorophore), a chemical compound capable of re-emitting light after excitation, is excited using light of a certain wavelength. As a quantum of light is absorbed by the fluorochrome, an electron in the fluorochrome moves to a higher energy state temporarily before falling back to its original orbit. The energy of this return to ground state is dissipated by the emission of a photon of lower energy (but longer wavelength, as energy and wavelength are inversely proportional according to Planck's law) from the fluorochrome (Ishikawa-Ankerhold et al., 2012). The difference between absorption and emission wavelengths is known as the Stokes shift, and the longer-wavelength emitted light is detected thus enabling visualization of the fluorochromes. In confocal laser-scanning microscopy, point-by-point illumination is combined with simultaneous detection, creating an image pixel-by-pixel as opposed to wide-field fluorescence microscopy where the entire imaging area is illuminated all at once (Ishikawa-Ankerhold et al., 2012). This has the advantage of being able to acquire images below the surface of a sample with higher resolution than conventional wide-field

imaging and can be used to create three-dimensional representations of samples through the use of optical sectioning or z-stacks (Ishikawa-Ankerhold et al., 2012).

Both FLIP and FRAP involve selectively photobleaching a given region of interest, such as a target cell or a subcellular compartment (depending on the magnification of the lens used), usually with much higher laser power (up to 100%) than the power used during imaging illumination (often less than 5%), then using digital image analysis to quantify fluorescent intensity changes representing the motion of fluorescently labelled molecules. In the study of gap-junctional intercellular communication, a microscope objective lens is selected such that multiple cells may be seen in the imaging field, and, during subsequent image analysis, regions of interest (ROI) are sized to encompass entire cells for fluorescent intensity changes.

Photobleaching (photodestruction) refers to the photochemical modification of a fluorochrome that irreversibly removes its ability to fluoresce. Photodestruction is a complex, poorly understood process thought to be caused by photolysis of the fluorescent molecule or chemical reactions involving other nearby molecules (Diaspro, Chirico, Usai, Ramoino, & Dobrucki, 2006). Once photobleached, previously fluorescent molecules are no longer able to be visualized (Ishikawa-Ankerhold et al., 2012).

Fluorescence recovery after photobleaching (FRAP) involves specific photobleaching of a selected target cell such that its fluorescent intensity drops. Specific photobleaching is then stopped, and fluorescent dye from adjacent cells diffuses into the target cell thus increasing its fluorescent intensity over time, which can then be quantified (Ishikawa-Ankerhold et al., 2012). A limitation of FRAP is that it shows only how much fluorescent stain is entering a bleached target cell but not where this stain is coming from.

Fluorescence loss in photobleaching, alternately fluorescence loss induced by photobleaching, is a complementary technique to FRAP. FLIP involves repeated photobleaching

of a selected target cell such that its fluorescent intensity drops and remains low, creating a concentration sink for fluorescently labelled molecules from adjacent cells to diffuse into. Fluorescent intensity changes are then measured in adjacent cells, not the target cell as in FRAP, with high temporal resolution to examine the movement of fluorescently labelled molecules out of these cells (Ishikawa-Ankerhold et al., 2012). FLIP can thus be used to examine gap-junctional intercellular-signal propagation as measuring losses in fluorescent intensity represents the motion of fluorescently labelled molecules into a target cell out of nearby gap-junction-connected cells. Applying FLIP to cells in intact tissue like tendon has allowed the quantification of gap-junctional intercellular communication with high agreement with a theoretic mathematical compartment model of diffusion (Maeda et al., 2012; Maeda & Ohashi, 2015). FLIP in the intervertebral disc has yet to be performed, one of the goals of the current study.

As shown in Figure 2.4A, the excitation laser beam in confocal laser-scanning microscopy has an hourglass-shaped path, so overall photobleaching and photodamage can occur throughout this shape, both during regular imaging as well as during specific high-laser-power photobleaching of a region of interest (Potter, 1996). In the latter case, high-intensity photobleaching also occurs in planes immediately above and below the region of interest, with reducing intensity as distance increases from the focal plane.

Two-photon laser-scanning microscopy, a similar fluorescence microscopy technique using a pulsed laser, involves the simultaneous excitation of a fluorochrome by two photons of roughly double the excitatory wavelength (half the energy) as used in one-photon excitation. It has the practical advantages of heavily reduced overall photobleaching and deeper tissue imaging depth (Helmchen & Denk, 2005; Ishikawa-Ankerhold et al., 2012). Figure 2.4B shows the laser beam path in two-photon excitation, where only a precise focal volume is illuminated. This

fluorescence excitation volume is usually less than one femtoliter, giving accurate $<1\text{ }\mu\text{m}$ imaging resolution in the z direction (Rubart, 2004).

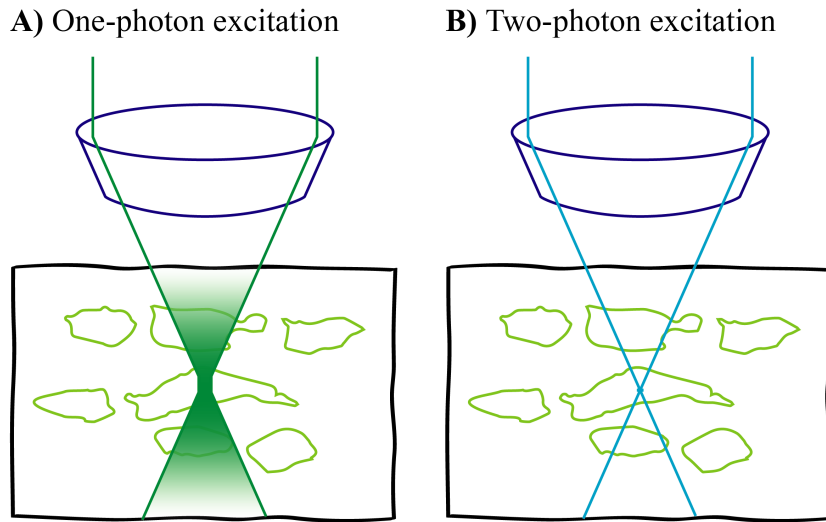


Figure 2.4: Laser-scanning fluorescence-microscopy excitation-laser-beam paths (side view). **A)** One-photon excitation (also known as confocal laser-scanning microscopy) illuminates an hourglass-shaped path. **B)** Two-photon excitation illuminates only a precise focal volume, greatly reducing out-of-plane photodamage and also allowing deeper imaging penetration into a specimen. Not to scale.

Chemical gap-junction blockers such as 1-octanol (Pappas, Rioult, & Ransom, 1996) and 18 α -Glycyrrhetic acid (AGA) (Davidson, Baumgarten, & Harley, 1986) are often used to inhibit gap-junctional intercellular communication in control experiments to ensure that measured fluorescent intensity changes are the result of the movement of fluorescently labelled molecules through gap junctions and not overall photobleaching or other effects. Pharmacological gap-junction blockers uncouple existing gap-junction channels and can be partially reversed (Davidson et al., 1986; Rozental, Srinivas, & Spray, 2001).

2.6 Pathologies of the Disc

2.6.1 Aging and degeneration.

With age, discs gradually lose their fluid content, reaching peak hydration around the age of 30 before beginning to decline (Coventry, 1969). Other age-related changes include a

reduction in proteoglycan content, changes in collagen type and distribution, and an increase in protein cross-linking (Cortes & Elliott, 2014). With aging, the balanced biochemical regulation of the cells in the disc and their surrounding extracellular matrix is upset. The turnover rate for collagen, a dominant extracellular-matrix-constituent protein, is especially slow, which may result in diminished structural integrity of the extracellular matrix (Sivan et al., 2014).

Disc degeneration has been defined as an aberrant cell-mediated response to progressive, irreversible structural failure and accelerated signs of aging (Adams & Roughley, 2006; Olsen et al., 2018; Zhao et al., 2007). Genetics, age, insufficient metabolite transport, and loading can weaken discs such that structural failure becomes possible during daily activities (Adams & Roughley, 2006). Degeneration was found to increase radial tensile and compressive strains during bending of the spine (Tsantrizos, Ito, Aebi, & Steffen, 2005). Additionally, connexin 43 and 45 have decreased expression with aging, correlating to decreased intercellular communication (Chung, Khan, & Diwan, 2003).

As homeostasis of the disc is maintained by complex interactions of the cells, extracellular matrix, and biomechanical stress, this balance becomes disturbed in degeneration. Disc cells stop producing extracellular matrix proteoglycans without proper chemical and mechanical cues, resulting in a reduction of matrix proteoglycans and thereby intradiscal pressure, which in turn alters biomechanical stresses on the cells in what has been termed the “degenerative circle” (Vergroesen et al., 2015).

2.6.2 Injury.

Traumatic injury can cause discs to herniate or slip. This can range from a small bulge, where the outer annular lamellae remain intact, to tearing or rupturing of the disc wall, and even to sequestrations, where the herniation becomes completely detached from the disc (Roberts, Evans, Trivedi, & Menage, 2006). Such injuries cause altered internal stress and strain

distribution in the disc, altering its normal functioning and enhancing the likelihood of incurring further degenerative effects (Cortes & Elliott, 2014).

2.6.3 Spinal deformities.

Kyphosis and scoliosis are large-scale deformities of the spine where abnormal curvature is present. Calcification of the cartilage end-plate was found in scoliotic IVDs (Roberts, Menage, & Eisenstein, 1993), which can disrupt the flow of nutrients through the end-plate (Roberts, Urban, Evans, & Eisenstein, 1996). Such deformities alter the mechanical loading conditions of the disc and may lead to eventual degenerative effects (Stokes & Iatridis, 2004).

2.7 Animal Models

Many animal models have been used to study the intervertebral disc, especially degenerative disc disease, including the mouse (Ohnishi et al., 2016; Sahlman et al., 2001), rat (Jeong et al., 2010), rabbit (Masuda et al., 2005), dog (Bergknut et al., 2012), sheep (Oehme et al., 2014), goat (Zhang et al., 2011), primate (Lauerman, Platenberg, Cain, & Deeney, 1992; Platenberg, Hubbard, Ehler, & Hixson, 2001), and cow (Desrochers & Duncan, 2012; Roberts, Menage, Sivan, & Urban, 2008; Vergari et al., 2017). Considerations in selecting an animal model for studying the intervertebral disc include: IVD and overall animal size compared to humans, magnitudes of biomechanical forces, and ethics (Daly, Ghosh, Jenkin, Oehme, & Goldschlager, 2016). Larger animals, such as the cow, provide anatomical dimensions that more closely represent the human spine compared to smaller animals. Bovine models have previously been studied in our group (Bruehlmann et al., 2002; Desrochers & Duncan, 2012; McMillan, 2009) and by many others (Demers, Antoniou, & Mwale, 2004; Furtwängler, Chan, Bahrenberg, Richards, & Gantenbein-Ritter, 2013; Razaq, Wilkins, & Urban, 2003; Roberts et al., 2008; Vergari et al., 2017; Walter, Illien-Jünger, Nasser, Hecht, & Iatridis, 2014). While bovine tails may experience less *in situ* loading compared to human spines and thus slightly altered

biochemistry, they have been proposed as a suitable model for studying young (<40 years old), healthy human lumbar intervertebral discs (Demers et al., 2004).

The current study is concerned with normal tissue function and the effects of mechanical load, not diseased or degenerated states, and thus prioritizes animal models with similar dimensions to human IVDs. As human tissue is sourced from either from surgery or cadavers, such tissue is often associated with diseased or degenerative changes. Oxtails are readily available each week during cattle slaughter at slaughterhouses near the city of Calgary, and are either sold independently or discarded, thus not requiring animal sacrifice solely for tail harvest. Given the strong supply of cattle in the province of Alberta, previous experience working with bovine IVDs, and the similar dimensions between bovine and human IVDs, a bovine model is ideal for this study.

2.8 Tissue Engineering

Treatment of symptomatic diseased discs can involve surgical interventions such as spinal fusions, discectomies, and even total disk replacements (Salari & McAfee, 2012). In treating lumbar degenerative disc disease, fusing two or more motion segments has long been considered the gold standard. A newer alternative approach of total disc replacement has gained popularity in recent years, though one review found no clinically relevant differences between fusion and total disc replacement (Van Den Eerenbeemt, Ostelo, Van Royen, Peul, & Van Tulder, 2010).

These surgical approaches are invasive, however, and tissue-engineered strategies may ultimately provide more biocompatible and biomimetic solutions. Much progress has been made in developing tissue-engineered IVDs, though current progress is limited to a few early animal models (Yang, Xu, Hurday, & Xu, 2016). Multiple studies had previously looked at tissue-engineering replacement strategies for either the nucleus pulposus or the annulus fibrosus alone,

but entire discs proved more challenging due to the different mechanical and biochemical properties of the annulus fibrosus and nucleus pulposus (Bron et al., 2009; Nerurkar, Elliott, & Mauck, 2010). More recently, biphasic scaffolds have been investigated, consisting of silk (Du et al., 2014), collagen (Choy & Chan, 2015), and native extracellular matrix (Wu et al., 2013). Such scaffolds typically consist of an internal core representing the nucleus pulposus and a surrounding outer core acting as the annulus fibrosus and have become better at replicating the mechanical properties of native discs.

Another design consideration for tissue-engineered disk replacements is how intracellular and intercellular signaling is facilitated within tissue-engineered scaffolds. In meniscus fibrochondrocytes, differences in calcium signaling were found between fibrochondrocytes in native tissue, in aligned nanofibrous scaffolds, and in flat silicone membranes (W. M. Han et al., 2014), demonstrating the importance of cellular microenvironment in cellular response to mechanical stimuli. Thus, a deeper understanding of mechanotransduction and cell signaling could benefit tissue-engineering approaches to IVD repair or regeneration.

2.9 Summary

Cells in the outer annulus fibrosus have been shown to communicate with each other via gap junctions, which are known to be mechanically regulated; however, the signal-propagation patterns among these interconnected cells is unknown. Ligament (Chi et al., 2005), tendon (Maeda et al., 2012) and bone (Adachi, Aonuma, Taira, et al., 2009), all types of load-bearing connective tissue, have demonstrated non-homogeneous or asymmetrical intercellular-signaling behavior, which may also occur in the annulus fibrosus given its unique tissue structure. This study will investigate intercellular signal-propagation patterns in the bovine annulus fibrosus and the effect of varying levels of mechanical load on intercellular gap-junction signaling. This knowledge will enhance understanding of the disc's normal functioning in the healthy state.

Chapter Three: Intercellular Signal Propagation

3.1 Introduction

The unique anatomy of the intervertebral disc, concentric layers of collagen fibers at alternating orientations, is an anisotropic environment. Gap-junctional intercellular signal propagation in this environment may thus also exhibit non-homogenous behavior. In this study, signal propagation both within a single layer as well as between adjacent layers of outer annulus fibrosus tissue will be examined using one- and two-photon-excitation confocal microscopy and fluorescence loss in photobleaching (FLIP), a technique that can be used to investigate the movement of fluorescently labelled molecules. Samples will be orientated such that individual annulus fibrosus layers are either parallel or perpendicular to the imaging plane to examine signaling patterns in the three-dimensional cellular microenvironment. The objective of this study is to measure gap-junctional intercellular signal propagation among interconnected cells of the outer annulus fibrosus of the intervertebral disc.

3.2 Methods

3.2.1 Circumferential disc strip preparation.

Tails from 12–30-month-old Angus or Hereford steers were collected from an abattoir approximately two hours post slaughter (Figure 3.1A). The four upper caudal discs (CC1–CC4) were excised, and either one or two strips per disc of outer annulus fibrosus were prepared, measuring roughly 30–60 mm long by 5 mm wide by 3 mm thick. Strips were immediately placed in calcium-free phosphate-buffered saline (Dulbecco's phosphate-buffered saline; without calcium, magnesium, or phenol red; ThermoFisher Scientific; Grand Island, New York) to both prevent dehydration and to allow osmotic equalization (for a total of at least two hours post preparation).

A)**B)**

Figure 3.1: An oxtail. **A)** As received from the abattoir. **B)** Exposed disc with two parallel lines drawn about 15 mm apart on the ventral surface.

Samples were immersed in 5 μ M calcein AM (ThermoFisher Scientific; Grand Island, New York) for 60 min at 37°C and 5% CO₂. Calcein AM, the acetomethoxy form of calcein, is a green fluorescent stain which freely crosses cell membranes in its non-fluorescent form to then be cleaved by intracellular esterases and become fluorescent, thus fluorescently labelling the entire cytosol of live cells only. Intracellular calcein binds to intracellular calcium (Moran, 2000), making it important in the study of mechanotransducive events. Samples were then rinsed

three times in approximately 20 mL of calcium-free phosphate-buffered saline (PBS) for five to ten minutes per rinse to remove any excess stain. Samples were incubated at 37°C until imaging time.

An experimental control group where gap-junctional intercellular communication was blocked was prepared by incubating samples in a 100 µM 18 α -Glycyrrhetic acid (AGA)-PBS solution for one hour at 37°C prior to imaging. AGA is a known gap junction inhibitor that can be reversed quickly enough such that existing junctions are thought to be re-opened rather than re-formed (Davidson et al., 1986). The mechanism behind this has been proposed to be an altered connexon configuration or conformational change as a result of AGA binding to gap junction connexons (Goldberg et al., 1996). The imaging bath used for samples in this group also contained 100 µM AGA. AGA was preferred instead of 1-octanol, another known gap junction blocker (Pappas et al., 1996), as AGA created a homogeneous solution with PBS. Octanol, an alcohol, is not miscible with water and formed a separate layer above PBS in the imaging bath, making the concentration of octanol highly variable surrounding submerged tissue samples, depending on which layer (or fraction thereof) a sample resided in.

3.2.2 Live-cell assay and cell morphology.

To check the functioning of the fluorescent label calcein AM, a live-cell assay, a control experiment was run. An intervertebral disc sample was frozen overnight after excision to kill any live cells, then thawed and stained with calcein AM per the same protocol as live samples.

Image sets of cell clusters in live tissue samples were collected without paying specific attention to cell morphology until later analysis. Collecting images randomly in this fashion likely gave a rough representation of the overall cell morphology distribution.

3.2.3 Applied tension.

When isolated and flattened, the concentric layers within each circumferential intervertebral disc strip sample became parallel sheets. Samples were loaded to their respective tension level (1, 5, 10, 15, 20, or 25%) in their longitudinal direction, corresponding to the circumferential direction in the intact disc. Physiologic circumferential strain usually does not exceed about 10% due to various combined loads of axial compression and bending (Ambard & Cherblanc, 2009; Desrochers & Duncan, 2010; Tsantrizos et al., 2005). Additionally, residual circumferential strains exist in the outer annulus fibrosus that vary by region: $0.63 \pm 2.1\%$ in the anterior quadrant, $8.3 \pm 1.5\%$ in lateral quadrants, and $4.4 \pm 2.1\%$ in the posterior quadrant (Duclos & Michalek, 2017). These residual strains were likely at least partially released during disc-strip excision. 1 through 25% strain at 5% increments should therefore cover a range circumferential strain values from below physiological levels through to magnitudes that exceed normal physiological values but are below failure values.

Studies were performed in a room-temperature, calcium-free phosphate-buffered-saline (PBS) imaging bath with a custom loading apparatus on an upright laser-scanning confocal microscope (Zeiss LSM 710, 20 \times 1.0 numerical aperture water immersion objective, 488 nm argon laser), as shown in Figure 3.2. In the loading apparatus, custom-machined metal clamps were attached to two opposed Siskiyou 100cri motorized roller-bearing translation stages with 0.1-micron resolution, as shown on Siskiyou DR1000 digital readouts (Siskiyou Corporation, Grants Pass, Oregon, USA).

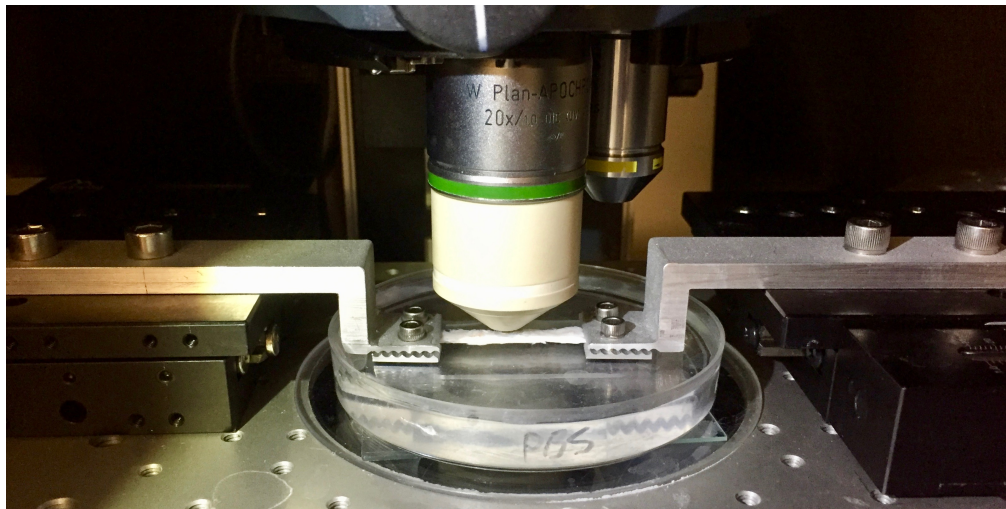


Figure 3.2: Custom tension-loading apparatus for an upright confocal microscope.

Initial efforts to standardize sample strain measurements involved marking two black parallel lines in the axial direction on the disc about 15 mm apart on the ventral surface (corresponding to the anterior surface in humans) prior to disc removal (Figure 3.1B). The distance between these lines was measured while hanging the tail to give an estimate of *in vivo* length. However, due to flattening of the circumferential strip after excision and osmotic equalization (swelling), this length was consistently found to be a few mm longer once in the imaging bath without any applied tension. Maintaining measured *in vivo* length would have therefore required compressing the samples. Thus, when samples were loaded into the clamps in the imaging bath, the motorized stages were translated such that sample tension was just taut: not loose nor under appreciable tension but enough to hold samples steady. Using digital calipers, initial sample length was measured as the distance separating the opposing grips (L_0). Samples were then manually tensioned to their desired tension level as quickly as possible, at a rate not slower than about 2%/s. Strain levels were calculated according to Equation 3.1, where ΔL is the distance to extend the sample by on a zeroed digital readout ($\Delta L/2$ for each of the two motorized stages in opposite directions) for strain ε (1, 5, 10, 15, 20, or 25%).

$$\Delta L = \varepsilon \cdot L_0 \quad (3.1)$$

Stress relaxation (creep; the continuous deformation of a material in response to applied mechanical load) tended to stabilize after about 30 minutes to one hour at each strain level (such that translation of visible cells in any direction was less than 5 μm), after which consecutive series of six-minute image sets were taken (one pre-FLIP image then 120 FLIP images). FLIP image sets that exhibited lateral cell movement greater than about 5 μm or a minimum end-point intensity drop in all tracked cells exceeding 0.40 (i.e. the highest end-point intensity among all cells [target cell, nearby neighbors, and otherwise] was below 0.60) were excluded from analysis as these image sets were too affected by drift to be reliable. Drift in confocal microscopy can happen in all three axes and often results from small temperature fluctuations (Adler & Pagakis, 2003).

Imaging in a PBS bath (>80% water) without a coverslip ensured minimal spherical aberration with the water-immersion objective lens. Prior confocal microscopy techniques involved the use of glass coverslips and oil-immersion lenses, where increasing imaging depth increased spherical aberration (image distortion) (Keller, 2006). High-numerical-aperture water-immersion objective lenses permit images to be collected at working depths of up to 240 μm with minimal spherical aberration (Keller, 2006).

Samples were aligned such that their layers were either parallel (Figure 3.3A) or perpendicular to the confocal imaging plane (Figure 3.3B). Most FLIP image sets were taken with sample layers parallel to the confocal imaging plane, so this will be considered the default orientation unless otherwise noted.

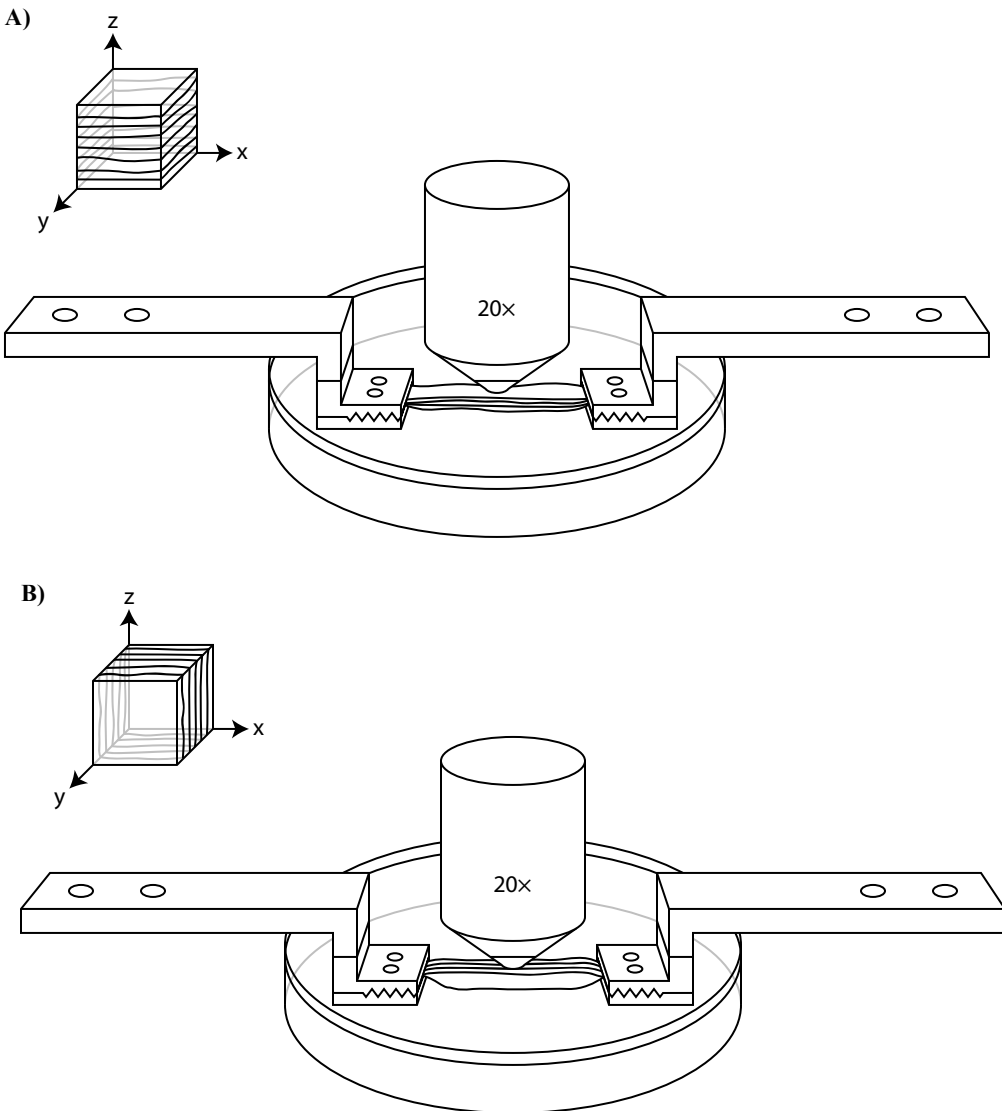


Figure 3.3: Strip sample orientation on the custom tension-loading apparatus on a confocal microscope (see photo in Figure 3.2). The clamps translate along the positive and negative x-axes to tension the sample. The confocal imaging plane corresponds to the x-y plane. The inset cubic representative volumes show sample layer orientation with respect to the global coordinate system. **A)** Sample layers parallel to the imaging plane; the positive z-direction (the global z-direction) goes from the inner toward the outer annulus fibrosus. This is considered the default orientation, unless otherwise specified. **B)** Sample layers perpendicular to the imaging plane; the positive y-direction goes from the inner toward the outer annulus fibrosus.

3.2.4 One-photon-excitation imaging settings.

Image dimensions were set to 300×100 pixels in the x- and y-directions, respectively (according to Figure 3.3), corresponding to 425.10×141.70 μm^2 , with 12-bit pixel depth (4096

levels). Each individual pixel represented $2.008 \mu\text{m}^2$. Laser power was set to 2%, and the band pass filter was set to allow light of wavelength 493–616 nm through. A thick optical slice section of $10.0 \mu\text{m}$ was used (7.62 Airy Units) in order to minimize the effects of z-plane image drift. Images were oversampled in the z-plane with three-slice z-stacks, separated by $5 \mu\text{m}$ in the z-direction to ensure overlap (Figure 3.4), collected at each time point. In typical confocal images where three z-slices were taken (in the Results section, starting with §3.3.2), only the middle z-slice (slice 2 of 3) is shown.

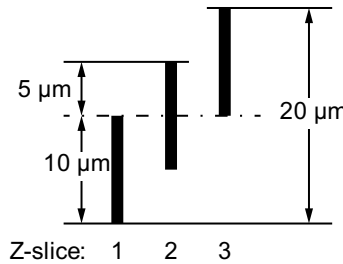


Figure 3.4: Overlapping $10 \mu\text{m}$ -thick z-slices (side view). Starting with slice 1 on the bottom, slices 2 and 3 are each shifted up in the z-direction by $5 \mu\text{m}$. The middle of slice 2 forms the centerline of the image in the z-plane. Each slice maintains its X and Y (horizontal) location, though the black bars representing individual slices here are horizontally staggered for clarity. Fluorescent intensities measured at each of the three z levels were combined according to Equation 3.2.

In the experimental groups that involved photobleaching of a specific target cell, the target cell was bleached at 100% laser power at its middle z-slice (slice 2/3 per Figure 3.4) with an increased laser-dwell time over the bleached region of interest ($21.61 \mu\text{s}$).

Images were captured at a depth of roughly $50\text{--}150 \mu\text{m}$ below the exposed annulus fibrosus surface in order to find cells below the dissection surface and inside intact extracellular matrix. One-photon-excitation confocal microscopy usually allows for a maximum imaging depth of about $100\text{--}200 \mu\text{m}$ in biological tissues (Helmchen & Denk, 2005; D. S. Richardson &

Lichtman, 2015), so imaging depth was a balance between finding undisturbed cells and signal intensity, which decreases with depth.

The imaging time period of six minutes was selected such that fluorescent intensity reductions in both the photobleached target cell as well as any gap-junction-connected nearby neighbors could be detected by the end-point of the FLIP experiment. The largest normalized fluorescent intensity drop should appear in the photobleached target cell (from 1.0 down to 0.2 or less), while nearby neighboring cells should exhibit a less pronounced drop in fluorescent intensity. The rate of gap-junctional intercellular communication has been examined on the minute time-scale (between one and ten minutes) assuming a compartment model of diffusion through gap junctions (Kanaporis, Brink, & Valiunas, 2011; Maeda et al., 2012; Maeda & Ohashi, 2015).

Only images that used one-photon excitation are shown in this study (see discussion in §3.4.4).

3.2.5 Two-photon-excitation imaging settings.

Experiments involving two-photon excitation used the same microscope, loading apparatus, and image dimensions as in one-photon excitation but with a different laser (Zeiss LSM 710, 20 \times 1.0 numerical aperture water immersion objective, Coherent Ultra FS Pulsed IR Laser set to 920 nm, MBS 690 dichroic mirror, 500–550 nm bandpass filter). While not exactly double calcein's one-photon-excitation wavelength of 495 nm (corresponding to 990 nm), 920 nm gave a stronger emission signal (Bush, Wokosin, & Hall, 2007). The optical slice thickness was 1.4 μ m, owing to the nature of non-linear optics, which cannot be adjusted via changing the pinhole diameter as in one-photon excitation. For specific target-cell photobleaching, the region of interest was photobleached with 100% laser power at the maximum allowable laser-dwell time of 173 μ s (per the Zeiss ZEN microscope software).

3.2.6 Image processing.

Images were processed using the Fiji distribution of ImageJ (Version 1.52d). Cellular fluorescent intensity values at each of the 120 time points were measured as the mean intensity value of an oval or polygonal region of interest (ROI) large enough to encompass each entire cell (Chi et al., 2004, 2005; Desrochers & Duncan, 2012). Oval ROIs were preferred; however, polygonal regions were used in cases where oval regions would have caused overlap with adjacent cells. Within a given FLIP image set, ROIs were selected to be the same size where possible, as measuring the mean intensity of a given ROI would be affected by its size (and thus the number of black pixels with zero fluorescent intensity).

Normalizing was performed to standardize measurements across different FLIP image sets. Each ROI had three z-plane measurements, one from each of its three z-slices (per Figure 3.4). Each z-slice was normalized to its respective pre-FLIP z-slice (taken at $t = 0$) according to Equation 3.2, where f_x is the normalized fluorescent intensity of a given cell at time x ; $f_{t=x, z=1}$, $f_{t=x, z=2}$, and $f_{t=x, z=3}$ are the measured intensity values at all three different z-heights of the given cell at time x ; and $f_{t=0, z=1}$, $f_{t=0, z=2}$, and $f_{t=0, z=3}$ are the measured intensity values of the given cell in its initial pre-FLIP image ($t = 0$) at the three z-heights. Each cell's fluorescent intensity profile thus starts at 1.0 (arbitrary units) at $t = 0$.

$$f_x = \left(\frac{f_{t_x z_1}}{f_{t_0 z_1}} + \frac{f_{t_x z_2}}{f_{t_0 z_2}} + \frac{f_{t_x z_3}}{f_{t_0 z_3}} \right) / 3 \quad (3.2)$$

Relative end-point ($t = 6$ min) fluorescent intensities were calculated for three to nine cells (including the target cell, if applicable) in each image set, depending on the total number of visible cells (three to more than nine). Cells were numbered arbitrarily, with lower cell numbers (Cells 1–4) generally corresponding to cells closest to the target cell and higher cell numbers (Cells 5 and higher) generally corresponding to cells farther away from the target cell. All

tracked cells had to demonstrate non-zero initial fluorescent intensity values across all three z-slices in order to ensure triple oversampling. Cells with initial fluorescent intensity values of zero in one or more z-slices were excluded from analysis as they would be highly sensitive to z-plane image drift. For example, a z-direction shift of 1 μm toward the outside of the imaging plane in a cell initially visible only 2 μm -deep inside the outside edge of an upper or lower z-slice (slice 1 or 3 in Figure 3.4) could incorrectly appear to have a 50% change in fluorescent intensity as half of its volume would have moved outside the imaging plane.

In the case of specific target-cell photobleaching, a “nearest neighbor” cell was assigned, defined as the cell that demonstrated the biggest fluorescent intensity drop within an approximately one-cell-diameter distance of the bleached target cell (usually Cell 1 or 2), as shown in Figure 3.5. As gap junctions form a channel between two connected cell membranes, cells or their processes must be in close contact to perform gap-junctional intercellular signaling, so cells outside this one-cell diameter distance of the target cell were unlikely to have connected processes that participated in gap-junctional intercellular signaling, unless they were part of an interconnected chain of cells.

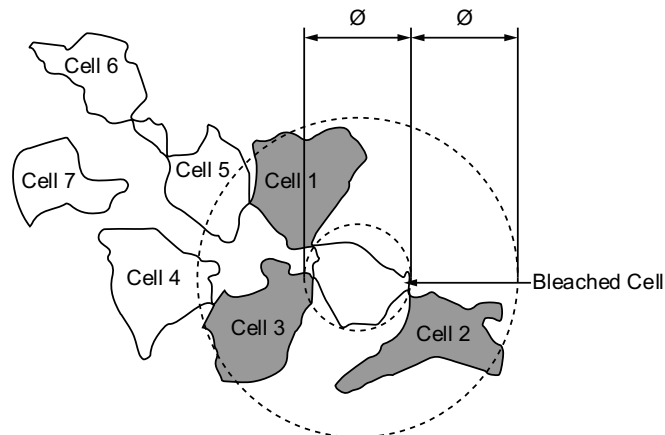


Figure 3.5: Nearest neighbors to the photobleached target cell. Cells that had a majority of their area within about one cell diameter of the bleached cell were considered nearby neighbors (Cells 1, 2 and 3 in this example). Typically, one of these nearest-neighbor cells had a slightly larger

fluorescent intensity drop over the six-minute imaging period than the others and was thus named the “nearest neighbor.” Not to scale.

For image sets where the imaging plane was perpendicular to the parallel annulus fibrosus lamellae as in Figure 3.3B, nearest-neighbor cells were defined as being “vertical neighbors” if they were located predominantly in the vertical direction in relation to the target cell (corresponding to the normal direction to the parallel annulus fibrosus lamellae), as shown in Figure 3.6. Such vertical-neighbor cells could perhaps be in separate concentric annulus layers (see Figure 2.1).

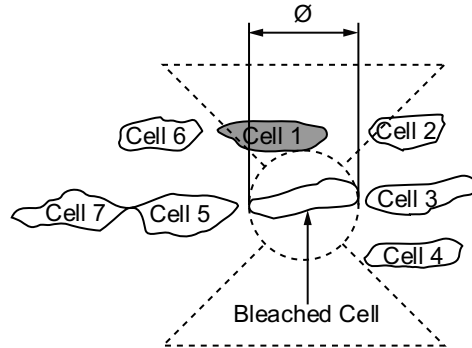


Figure 3.6: Vertical neighbors. The “radial-direction window” applies only to image sets where the imaging plane was perpendicular to the parallel annulus fibrosus lamellae (as in Figure 3.3B). In this diagram, nearby-neighbor cells (see Figure 3.5) to the photobleached target cell are considered to be in the radial direction if they are predominantly in this page’s positive or negative y-direction (vertical) from the photobleached target cell and are thus labelled “vertical neighbors” (Cell 1 in this example). Cells located laterally to the photobleached target cell are outside the radial-direction window. Not to scale.

Cell shape was classified according to the three categories in Table 3.1. Each FLIP image set was assigned one of the three cell morphology types depending on the predominant cell type counted in the image. For example, a majority of spindle-shaped lamellar cells in an image set would result in the image set being classified as spindle-shaped lamellar.

Table 3.1: Cell morphology categories in the outer bovine annulus fibrosus. Adapted from McMillan (2009)

Morphology	Definition
Spindle-shaped lamellar	Cell has two opposing pointed processes and a major axis 1.5 times larger than the minor axis
Round lamellar	Cell has a major axis less than 1.5 times larger than the minor axis
Interlamellar	Cell has a fusiform shape with three or more processes

Intercellular signal propagation was examined by determining the total number of nearest neighbors to a photobleached target cell (per Figure 3.5) that appeared to be close enough to transmit their fluorescently labelled molecules into the target cell through open gap junctions, either by direct contact across cellular membranes or by connected processes. The fraction of such neighboring cells that appeared to be involved in communication was compared to the total number of eligible cells within the roughly one-cell-diameter distance of the target cell. For example, if only cell 1 in Figure 3.5 had a clear drop in fluorescent intensity at the end of the six-minute FLIP experiment versus most other non-photobleached cells (cells 2–7), then the image would be described as having “1 of 3” nearest neighbors responding. In order for cells to be considered involved in communicating with the target cell, they had to demonstrate clear fluorescent intensity drops below more distant cells. In some image sets it was unclear if a certain nearby neighboring cell was involved in intercellular communication with the target cell; such cells were conservatively considered to be non-communicating as it was found that the majority of cells within the nearby-neighbor distance usually appeared to be involved in communication. Images where the photobleached target cell had zero nearby neighbors were excluded from analysis as only the photobleached target cell exhibited a significant reduction in fluorescent intensity in such cases (“0 of 0” responding neighbors).

FLIP image sets that were classified as having “spindle-shaped lamellar” cell morphologies were further analyzed to examine signal-propagation patterns within the highly organized parallel-collagen-fiber layout of individual outer annulus lamellae. The objective of this analysis was to examine intercellular-signaling patterns within a given lamellae (intra-lamellar communication). Of all the FLIP image sets identified as “spindle-shaped lamellar,” only those where the photobleached target cell had at least one adjacent neighbor both laterally and longitudinally were included for analysis, per Figure 3.7.

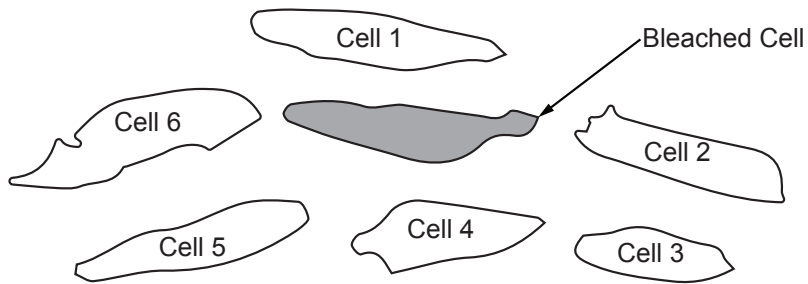


Figure 3.7: Inclusion criteria for intra-lamellar communication within spindle-shaped lamellar cells (for image sets where the imaging plane was parallel to the annulus lamellae as in Figure 3.3A only). Cells 2 and 6 are within the same longitudinal linear array as the bleached cell, and cells 1 and 3–5 are in parallel lateral arrays. At least one cell in both the longitudinal and lateral directions was required for image sets to be analyzed for intra-lamellar communication. Not to scale.

3.3 Results

Table 3.2 shows the breakdown of FLIP image sets by experimental condition and oxtail source. Seven unique oxtails were used, with up to three discs harvested from each tail. In each strip, up to 14 individual cell clusters were imaged, with each unique cell cluster corresponding to one FLIP image set in all experimental conditions except for the non-photobleached control group, where the end-point intensities of multiple cells within the same image were used in order to minimize experiment run times as no cells in these images were expected to change significantly (35 cells were tracked for fluorescent-intensity changes across eight FLIP image

sets, instead of running 35 FLIP image sets for 35 cells). A complete breakdown of experimental data is available in Appendix A.

Table 3.2: Overview of experimental data

Strain (%)	Condition	Imaging-plane orientation	Oxtails	Disc strips	FLIP image sets
1	Non-photobleached control	Parallel	3	4	8
1	Blocked gap junctions	Parallel	3	4	16
1	Open gap junctions	Parallel	2	3	29
1	Open gap junctions	Perpendicular	1	3	17
5	Open gap junctions	Parallel	3	3	15
10	Open gap junctions	Parallel	2	2	16
15	Open gap junctions	Parallel	1	1	10
20	Open gap junctions	Parallel	1	1	14
25	Open gap junctions	Parallel	1	2	10
Totals			7 unique ¹	16 unique ¹	135 total; 111 open gap junctions

¹ Not sums of the above numbers; certain oxtails and strips were used in multiple different experimental groups. See Appendix A for a complete list of results.

3.3.1 Live-cell assay and cell morphology.

Figure 3.8A shows a typical cell cluster of spindle-shaped cells in a live sample stained with calcein within a few hours post slaughter, and Figure 3.8B shows a typical area within the frozen sample, where no clearly stained cells could be found.

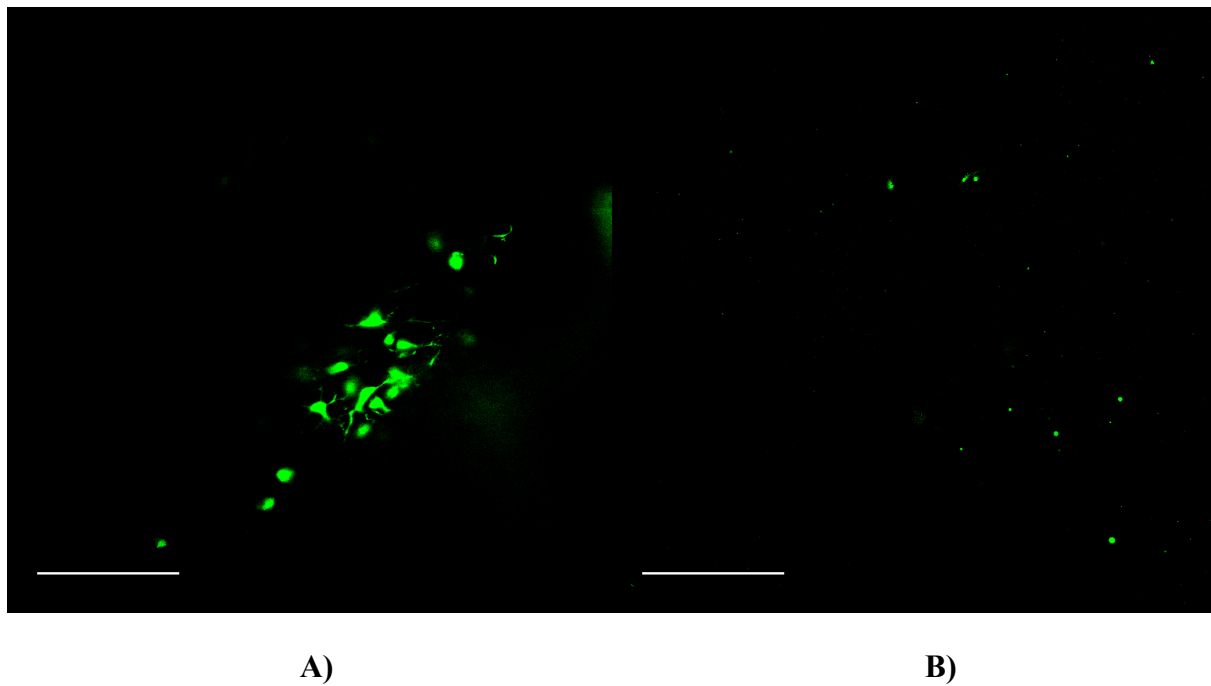


Figure 3.8: Typical confocal images of bovine outer annulus fibrosus stained with 5 μM calcein AM. **A)** Tissue imaged a few hours post slaughter. Note the presence of interlamellar cells with branching processes **B)** Tissue imaged after overnight freezing, thawing, then staining. Note the lack of cells. Scale bar represents 100 μm .

The distribution of cell categories for all 135 FLIP image sets (each with up to 9 analyzed cells) according to the cell types defined in Table 3.1 (spindle-shaped lamellar, round lamellar, and interlamellar) are shown in Figure 3.9. All experimental groups were included, including non-photobleached controls, AGA-blocked gap junctions, and different strain levels. Cells were fairly evenly split between interlamellar (39.3%) and lamellar (60.7%). Among the two sub-categories of lamellar cells, spindle-shaped lamellar cells were about twice as common (43.0% of total images) as round lamellar cells (17.8% of total images). Figures 3.12 and 3.16–3.17 show confocal microscope images of interlamellar cells; Figures 3.18–3.19 show confocal microscope images of round lamellar cells; and Figures 3.11, 3.13 and 3.20–3.21 show confocal images of spindle-shaped lamellar cells.

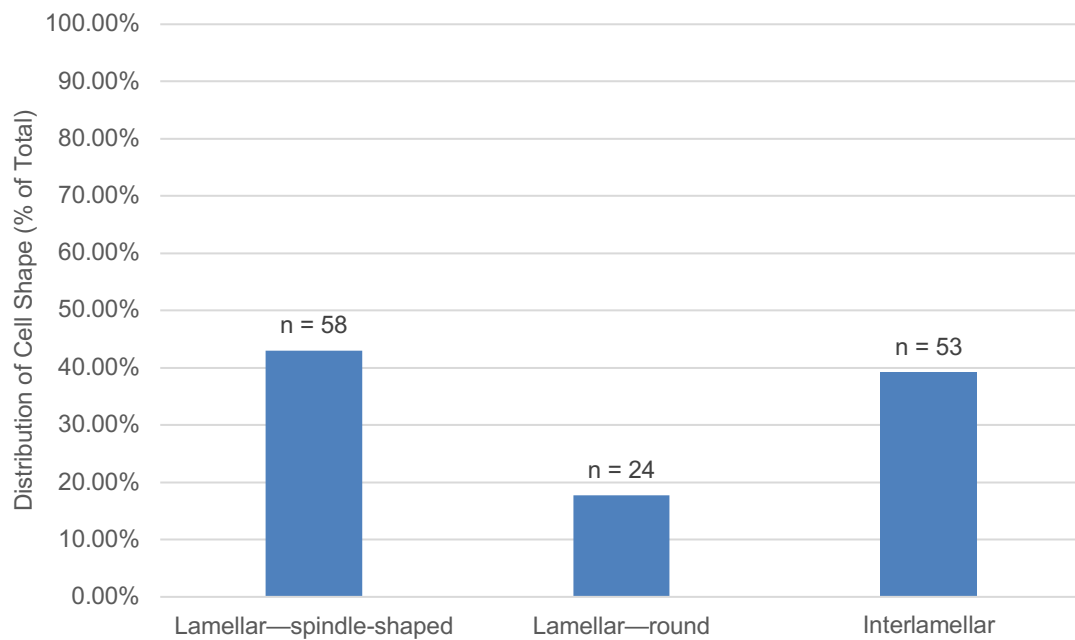


Figure 3.9: Distribution of cell morphologies across 135 FLIP image sets of outer bovine annulus fibrosus. Each image set contained up to 9 cells that were considered for fluorescent intensity analysis.

Per the work of McMillan (2009), interlamellar cells can be found within close proximity of spindle-shaped lamellar cells (within about 5 μm). Figure 3.10 shows a z-stack of the transition between spindle-shaped lamellar cells (Figure 3.10A) to interlamellar cells (starting in Figure 3.10D). Viewed in three dimensions, these spindle-shaped lamellar cells and interlamellar cells are possibly close enough to each other to be considered nearby neighbors (per Figure 3.5), with less than about 10 μm separating the membranes of these two cell types in the z-direction.

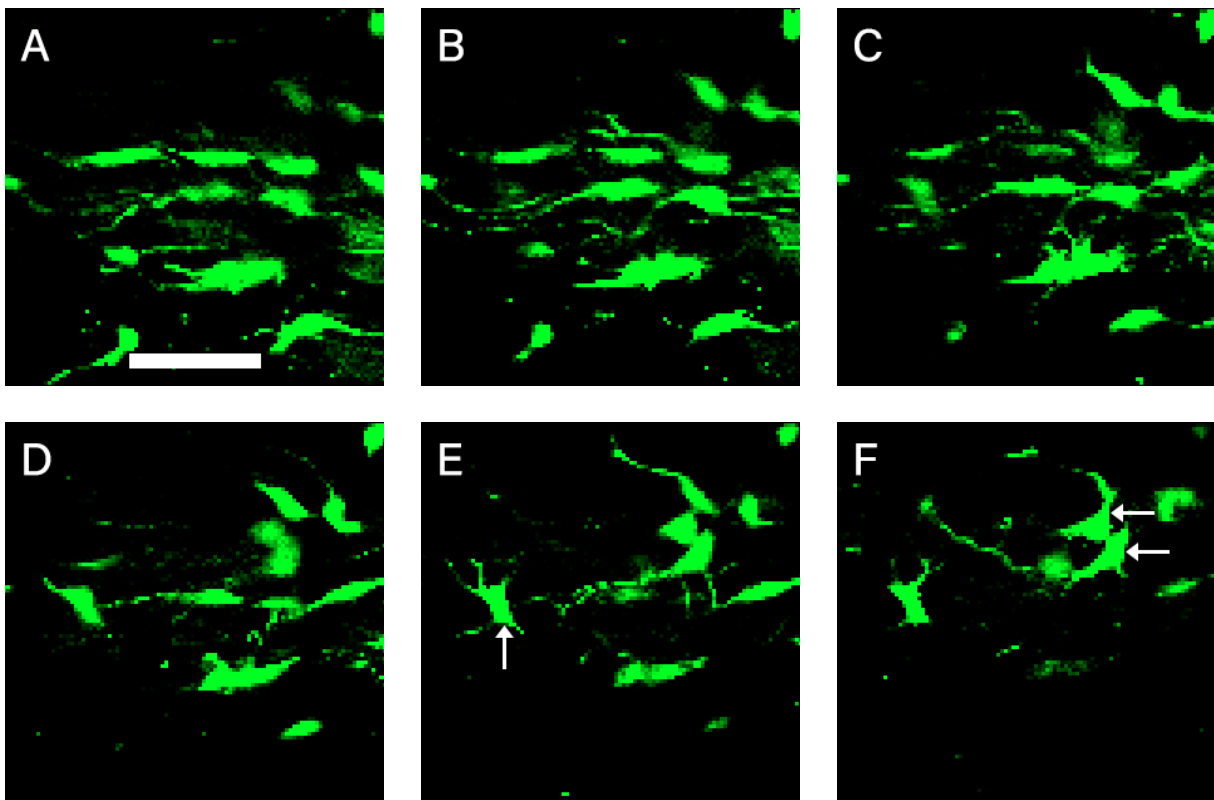


Figure 3.10: Z-stack of confocal images from the bovine outer annulus fibrosus. **A)** Spindle-shaped lamellar cells in linear arrangement. **B–F)** Images taken at 4.4 μm intervals show the transition to interlamellar cells with branching processes (shown with arrows). Scale bar represents 50 μm .

3.3.2 1% Strain.

With the FLIP experimental protocol and samples oriented such that their layers aligned with the confocal imaging plane (per Figure 3.3A), three experimental groups at 1% strain were examined (see flow chart in Figure 1.1): a non-photobleached control group without specific target-cell photobleaching, a group with specific target-cell photobleaching, and a group with both specific target-cell photobleaching and the use of chemical-gap-junction-inhibitor AGA.

3.3.2.1 Non-photobleached control.

Typical confocal images of the experimental control group without specific target-cell photobleaching are shown in Figure 3.11A and B. Fluorescent intensity profiles of each labelled cell over the course of six minutes (120 imaging steps) are shown in Figure 3.11C. End-point

fluorescent intensities for all five cells in this sample ranged from 0.877 to 1.074. Thirty-five individual cells from eight FLIP image sets across four different IVD specimens were analyzed in this experimental group. End-point ($t = 6$ min) cellular fluorescent intensities for all cells in this group ranged from 0.660 to 1.074, averaging 0.835 ± 0.021 (SEM).

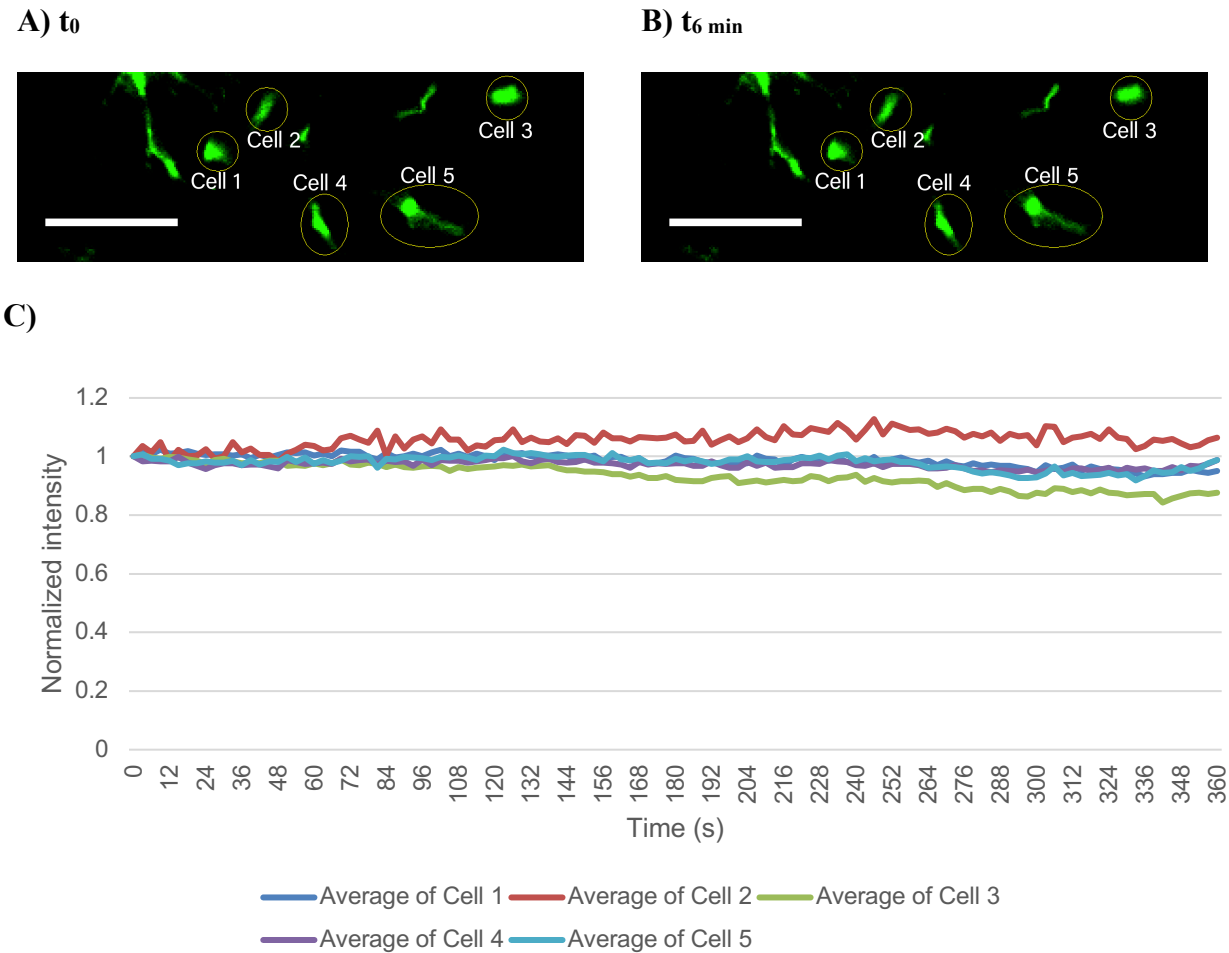


Figure 3.11: Non-photobleached control. Fluorescence loss in photobleaching of bovine outer annulus fibrosus cells in the control experimental group without specific target-cell photobleaching, at 1% strain: **A)** $t = 0$; **B)** $t = 6$ minutes. **C)** Fluorescent intensity profiles for labelled cells. Note how all cells retain a normalized intensity around 1.0. Scale bars represent 100 μm .

3.3.2.2 Open gap junctions.

Typical confocal images of the experimental group with 100% laser power photobleaching of a specific target cell are shown in Figure 3.12A and B. Fluorescent intensity profiles of each labelled cell over the course of six minutes (120 imaging steps) are shown in Figure 3.12C. The end-point fluorescent intensity of the photobleached target cell was 0.000 in this sample. Across 30 cell clusters from three different IVD strips, end-point fluorescent

intensities of the photobleached target cell ranged from 0.000 to 0.407, averaging 0.144 ± 0.022 (SEM). The end-point fluorescent intensity of the nearest neighbor to the photobleached target cell (Cell 1 in Figure 3.12) was 0.321. Across 30 cell clusters, the nearest-neighbor end-point fluorescent intensities ranged from 0.081 to 0.787, averaging 0.504 ± 0.035 (SEM).

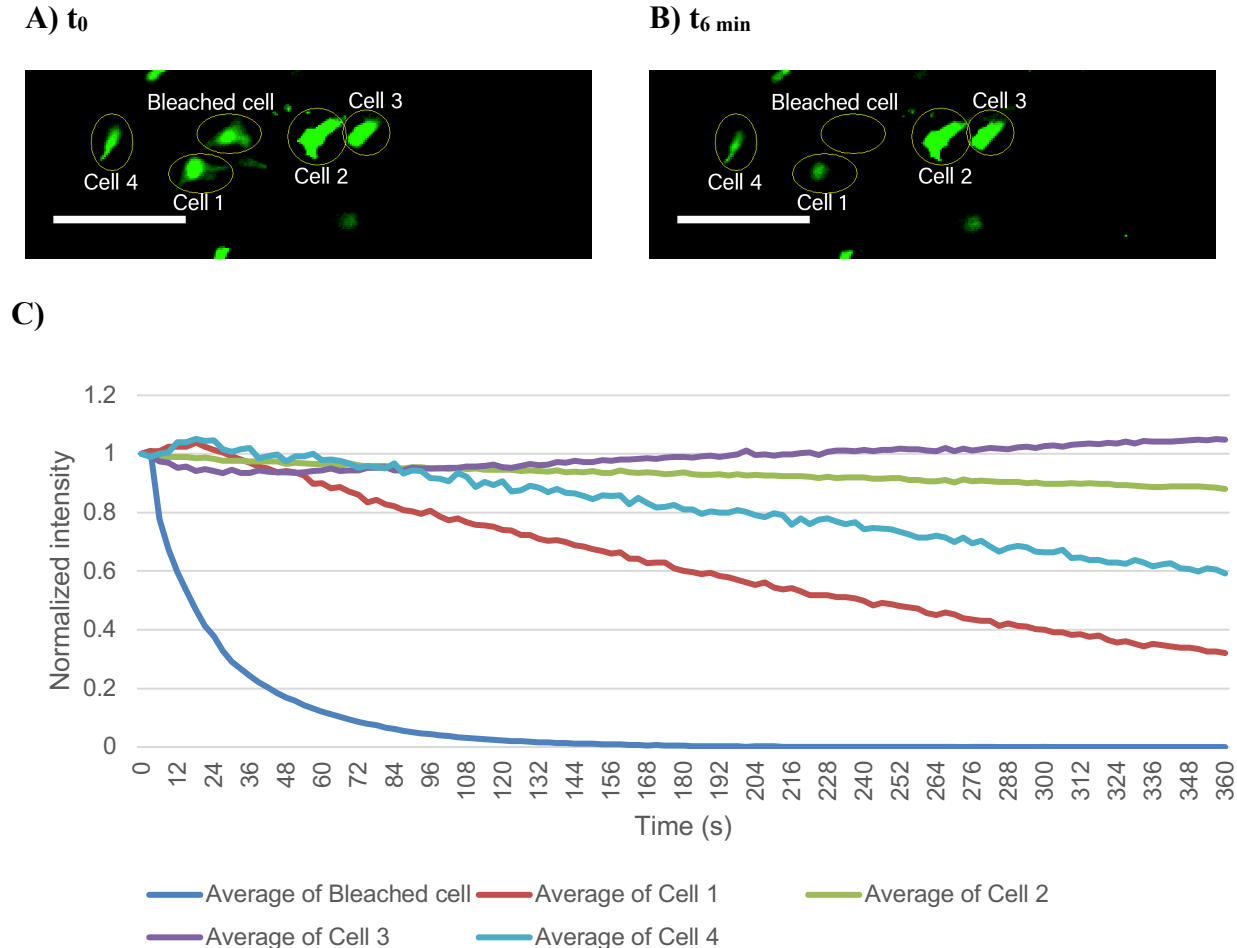


Figure 3.12: Open gap junctions. Fluorescence loss in photobleaching of bovine outer annulus fibrosus cells with specific target-cell photobleaching, at 1% strain: **A)** $t = 0$; **B)** $t = 6$ minutes. **C)** Fluorescent intensity profiles for labelled cells. Note the large drops in fluorescent intensity in both the bleached cell and cell 1. Scale bars represent 100 μm .

3.3.2.3 Blocked gap junctions.

Typical confocal images of the experimental group with 100% laser power photobleaching of a specific target cell while using gap-junction inhibitor AGA are shown in

Figure 3.13A and B. Fluorescent intensity profiles of each labelled cell over the course of six minutes (120 imaging steps) are shown in Figure 3.13C. The end-point fluorescent intensity of the photobleached target cell was 0.166 in this sample. Across 16 cell clusters in four different IVD strips, end-point fluorescent intensities of the photobleached target cell ranged from 0.000 to 0.465, averaging 0.097 ± 0.027 (SEM). The end-point fluorescent intensity of the nearest neighbor to the photobleached target cell (Cell 1 in Figure 3.13) was 0.807. Across 16 cell clusters, the nearest-neighbor end-point fluorescent intensities ranged from 0.306 to 0.910, averaging 0.661 ± 0.047 (SEM).

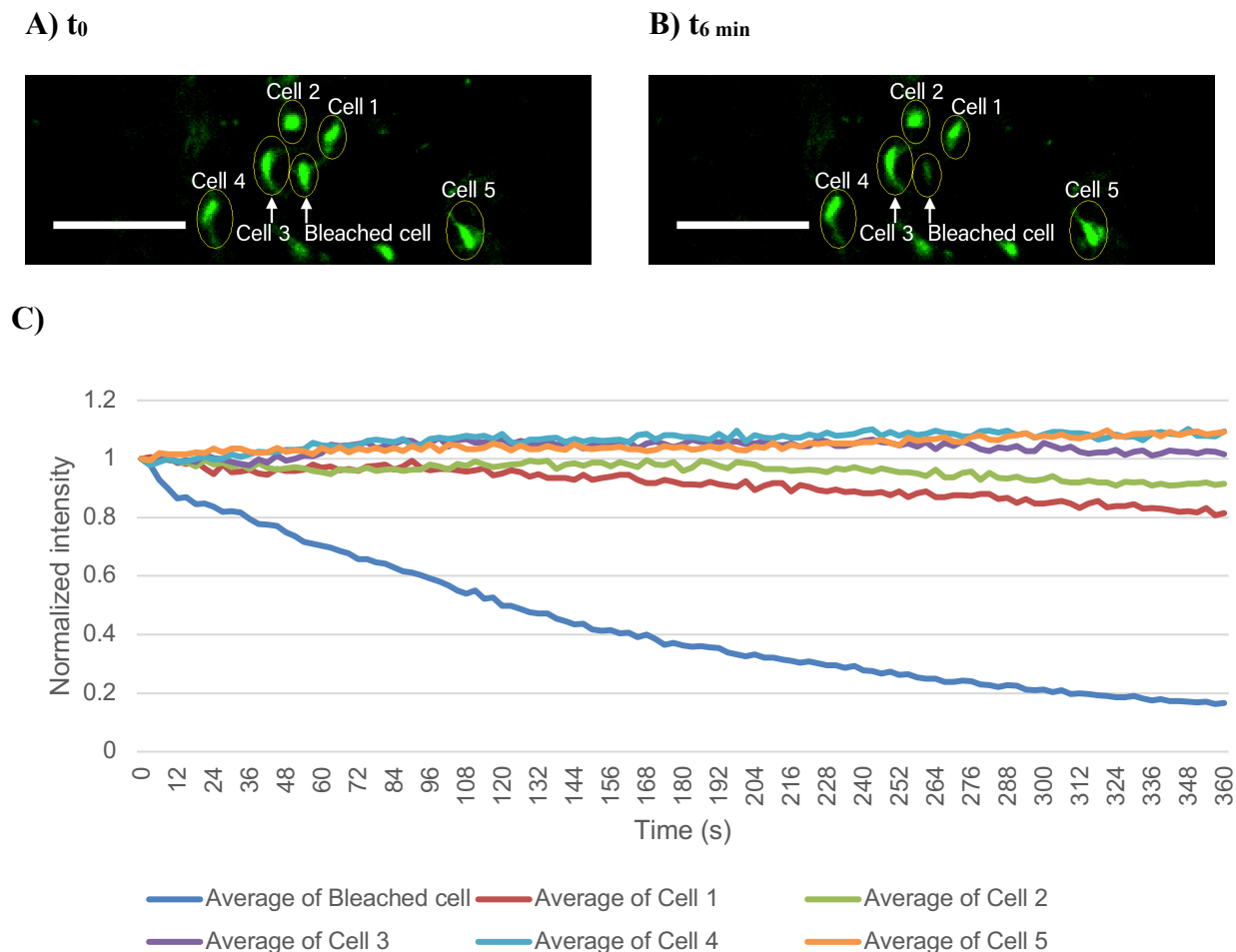


Figure 3.13: AGA-blocked gap junctions. Fluorescence loss in photobleaching of bovine outer annulus fibrosus cells with chemical gap-junction blocker AGA and specific target-cell

photobleaching, at 1% strain: **A)** $t = 0$; **B)** $t = 6$ minutes. **C)** Fluorescent intensity profiles for labelled cells. Note the large drop in fluorescent intensity in the bleached cell only. Scale bars represent 100 μm .

3.3.2.4 Overall results, 1% strain.

Figure 3.14 shows the relative end-point ($t = 6$ min) fluorescent intensities of the nearest neighbor to the photobleached target cell (per Figure 3.5) for the three preceding experimental groups (open gap junctions, blocked gap junctions with AGA, and non-bleached control) at 1% strain. Mean-comparison p-values are indicated on the plot, with all group means being significantly different at $p < 0.05$.

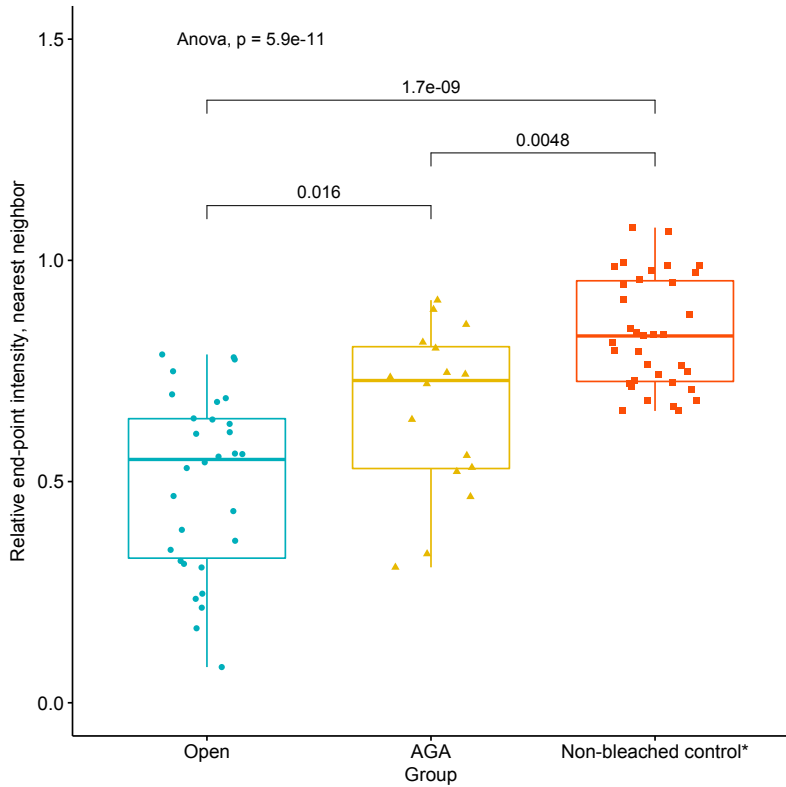


Figure 3.14: Effect of specific-target-cell photobleaching and chemical gap-junction blocking with the FLIP experimental protocol in the bovine outer annulus at 1% strain. The relative end-point ($t = 6$ min) fluorescent intensity of the photobleached target cell's nearest neighbor (as defined in Figure 3.5) is shown. Lower values indicate enhanced gap-junctional intercellular communication. Mean-comparison p-values between the different groups are shown on the plot.
*As there was no specific target-cell photobleaching in this case, single cells were used as the nearest neighbor (35 cells from eight FLIP image sets).

3.3.3 Higher strain levels.

Experiments involving specific photobleaching of a target cell without the use of gap junction blockers were carried out at strain levels of 1, 5, 10, 15, 20 and 25%. End-point fluorescent intensities for the photobleached target cell as well as the corresponding nearest neighbors are shown in Table 3.3.

Table 3.3: End-point fluorescent intensity values at different strain levels

Strain (%)	Target-cell end-point intensity (mean \pm SEM)	Nearest-neighbor end-point intensity (mean \pm SEM)
1	0.149 \pm 0.022	0.508 \pm 0.037
5	0.066 \pm 0.019	0.346 \pm 0.038
10	0.063 \pm 0.024	0.397 \pm 0.045
15	0.056 \pm 0.015	0.294 \pm 0.043
20	0.190 \pm 0.038	0.491 \pm 0.043
25	0.214 \pm 0.031	0.346 \pm 0.043
Overall	0.124 \pm 0.012	0.421 \pm 0.019

Figure 3.15 shows the end-point fluorescent intensities of the nearest-neighbor cell at each different strain level. Tukey's multiple comparison test found the only statistically significant difference to be between the 1% and 15% strain groups ($p = 0.019$).

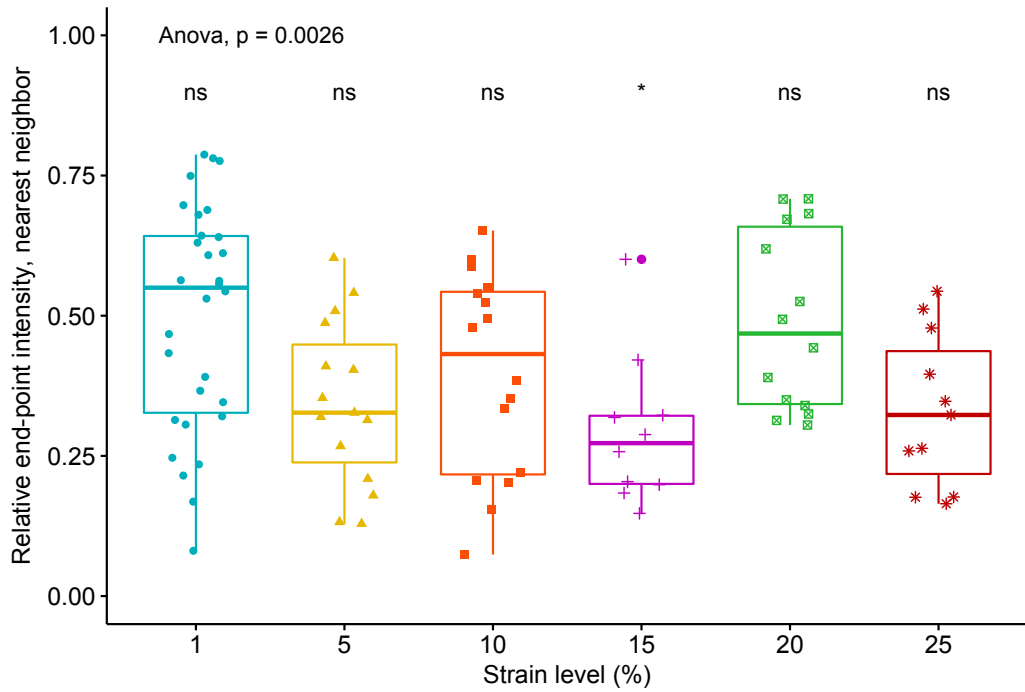


Figure 3.15: Effect of strain on gap junctional intercellular signaling using the FLIP experimental protocol in the bovine outer annulus. The relative end-point ($t = 6$ min) fluorescent intensity of the photobleached target cell's nearest neighbor (as defined in Figure 3.5) is shown. Lower values indicate enhanced gap-junctional intercellular communication. $*p < 0.05$ against the overall mean.

3.3.4 Intercellular signal propagation.

Signal propagation in the outer bovine annulus fibrosus was examined with respect to cell morphology and the number of eligible nearest-neighbor cells that appeared to communicate with the photobleached target cell. Signal-propagation patterns were separated into two broad categories: images where not all (i.e. none or a fraction of) nearby neighbors appeared to communicate with the photobleached target cell, and images where all nearby neighbors appeared to communicate with the photobleached target cell. Example images of both categories within each group of cell morphology (spindle-shaped lamellar, round lamellar, and interlamellar) are shown in the following three sections.

3.3.4.1 Interlamellar cells.

Interlamellar cells were typically clumped together in groups such that the target cell had up to five nearby neighbors according to the definition in Figure 3.5. Figure 3.16 shows an example of interlamellar cells where not all (0 of 2) nearest-neighbor cells appeared to communicate with the photobleached target cell, and Figure 3.17 shows an example of interlamellar cells where all (2 of 2) nearest-neighbor cells appeared to communicate with the photobleached target cell.

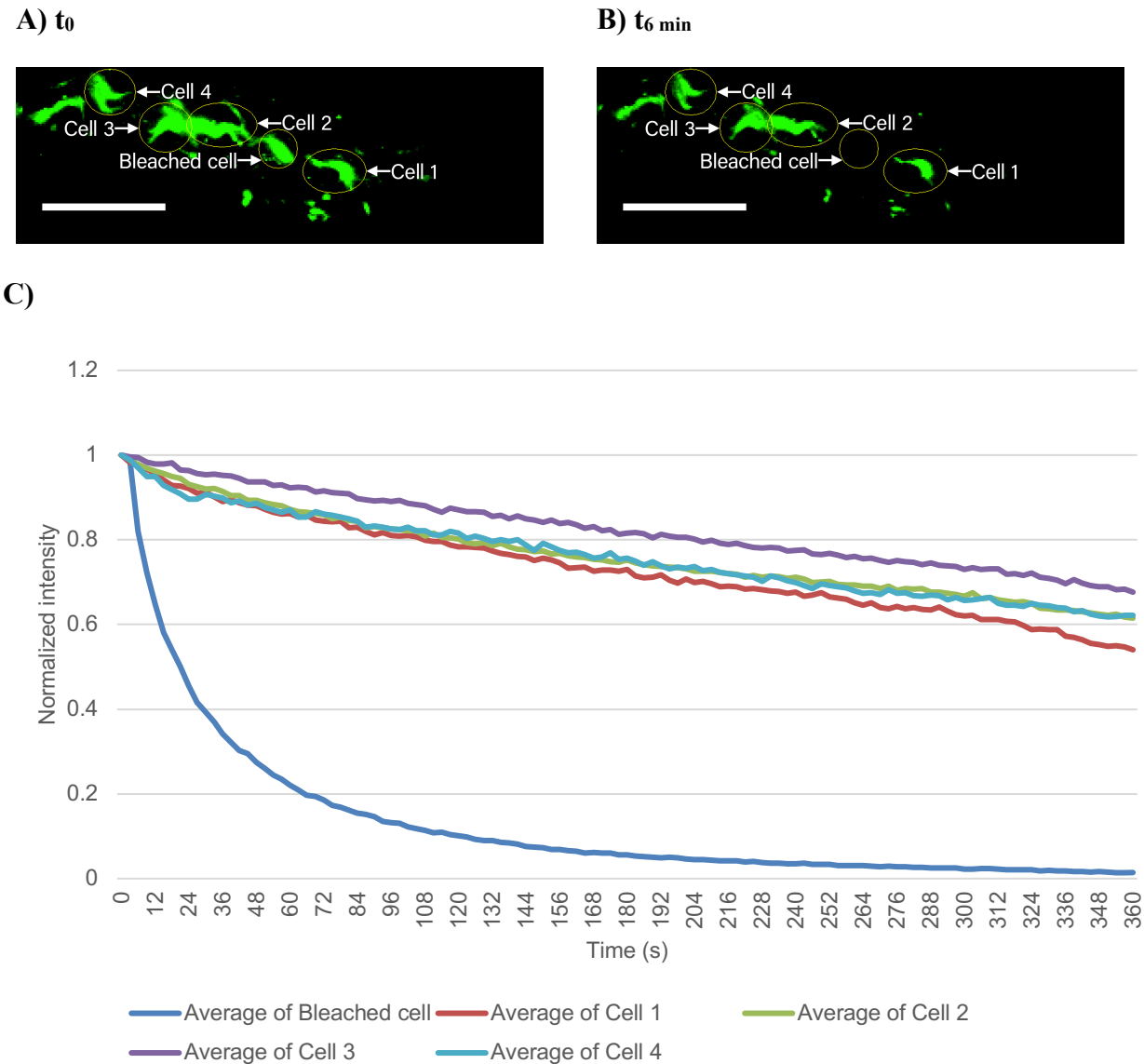


Figure 3.16: Interlamellar cells with no nearby neighbors communicating. Confocal images of interlamellar cells in the outer bovine annulus fibrosus before and after 120 FLIP imaging steps where not all nearby neighbor cells to the photobleached target cell appeared to communicate with the target cell: **A)** $t = 0$; **B)** $t = 6 \text{ minutes}$. **C)** Fluorescent intensity profiles for labelled cells. Note the fluorescent intensity drop in the bleached cell only. Cells 1 through 4 maintained similar fluorescent intensity profiles. As cells 1 and 2 are the only nearby neighbors to the target cell, this image is conservatively classified as having 0 of 2 eligible nearby neighbors involved in intercellular communication. Scale bars represent 100 μm .

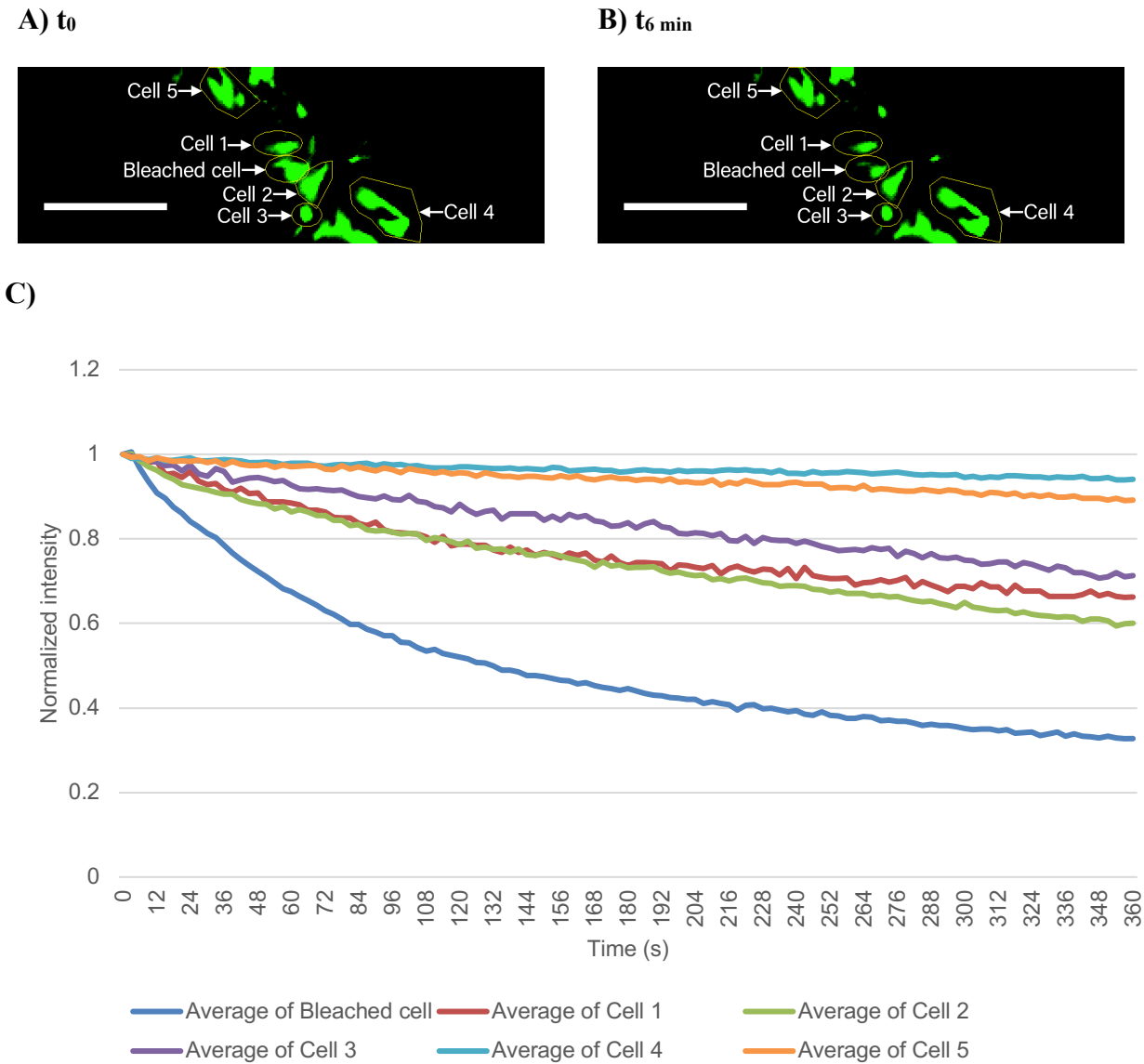


Figure 3.17: Interlamellar cells with all nearby neighbors communicating. Confocal images of interlamellar cells in the outer bovine annulus fibrosus before and after 120 FLIP imaging steps where all nearby neighbor cells to the photobleached target cell appeared to communicate with the target cell: **A) $t = 0$** ; **B) $t = 6 \text{ minutes}$** . **C)** Fluorescent intensity profiles for labelled cells. Note how both nearby-neighbor cells (cells 1 and 2) exhibit drops in fluorescent intensity below all other cells. This image is therefore classified as having 2 of 2 nearby neighbors involved in intercellular communication. Scale bars represent 100 μm .

3.3.4.2 Round lamellar cells.

Round lamellar cells were typically clumped together in groups such that the target cell had up to four nearby neighbors according to the definition in Figure 3.5. Figure 3.18 shows an example of round lamellar cells where not all (0 of 1) nearest-neighbor cells appeared to communicate with the photobleached target cell, and Figure 3.19 shows an example of round lamellar cells where all (3 of 3) nearest-neighbor cells appeared to communicate with the photobleached target cell.

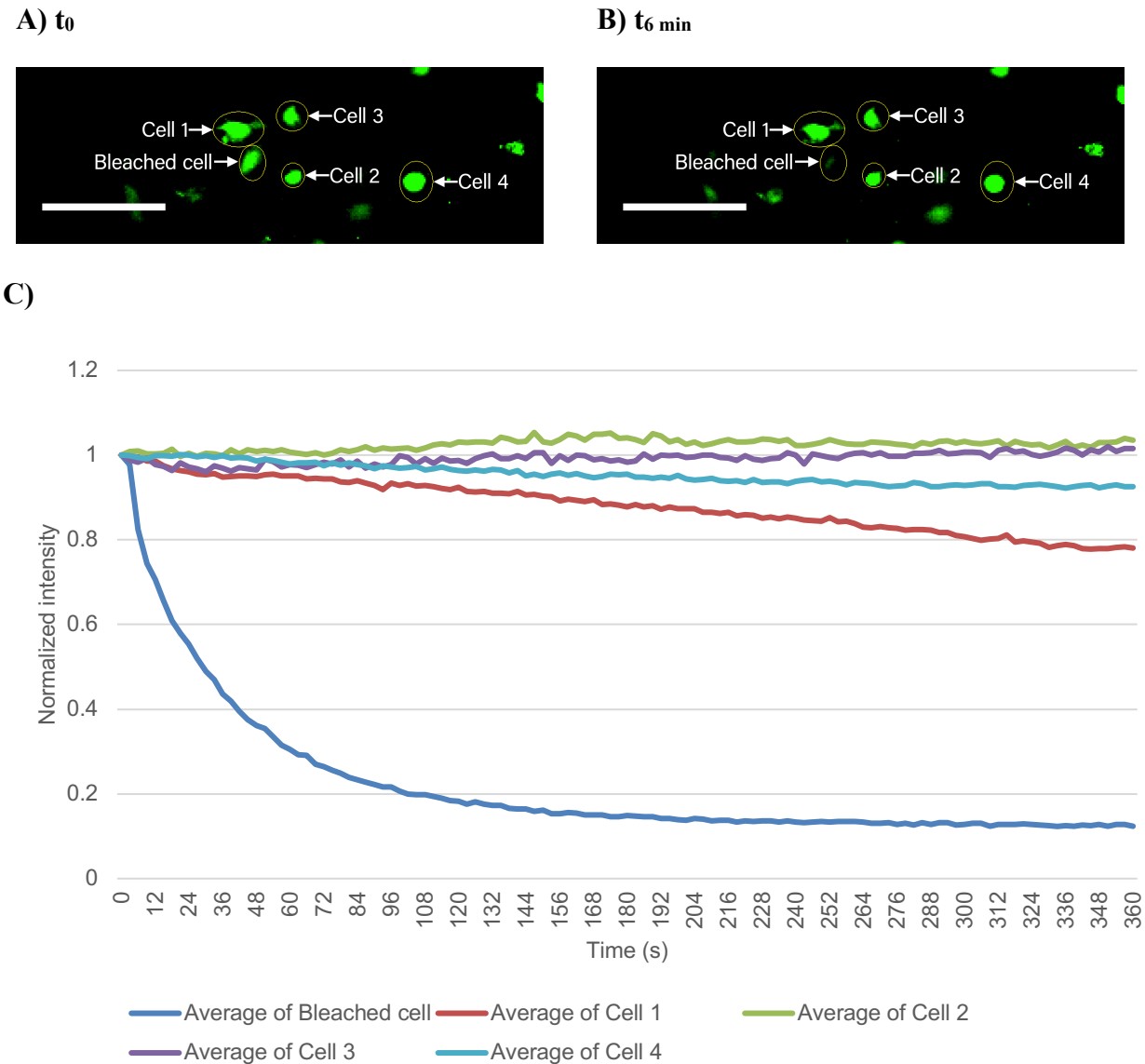


Figure 3.18: Round lamellar cells with no nearby neighbors communicating. Confocal images of round lamellar cells in the outer bovine annulus fibrosus before and after 120 FLIP imaging steps where not all nearby neighbor cells to the photobleached target cell appeared to communicate with the target cell: **A)** $t = 0$; **B)** $t = 6$ minutes. **C)** Fluorescent intensity profiles for labelled cells. Note the fluorescent intensity drop in the bleached cell only. Cells 1 through 4 maintained high fluorescent intensities. As cell 1 is the only nearby neighbor to the target cell, this image is conservatively classified as having 0 of 1 nearby neighbor involved in intercellular communication. Scale bars represent 100 μm .

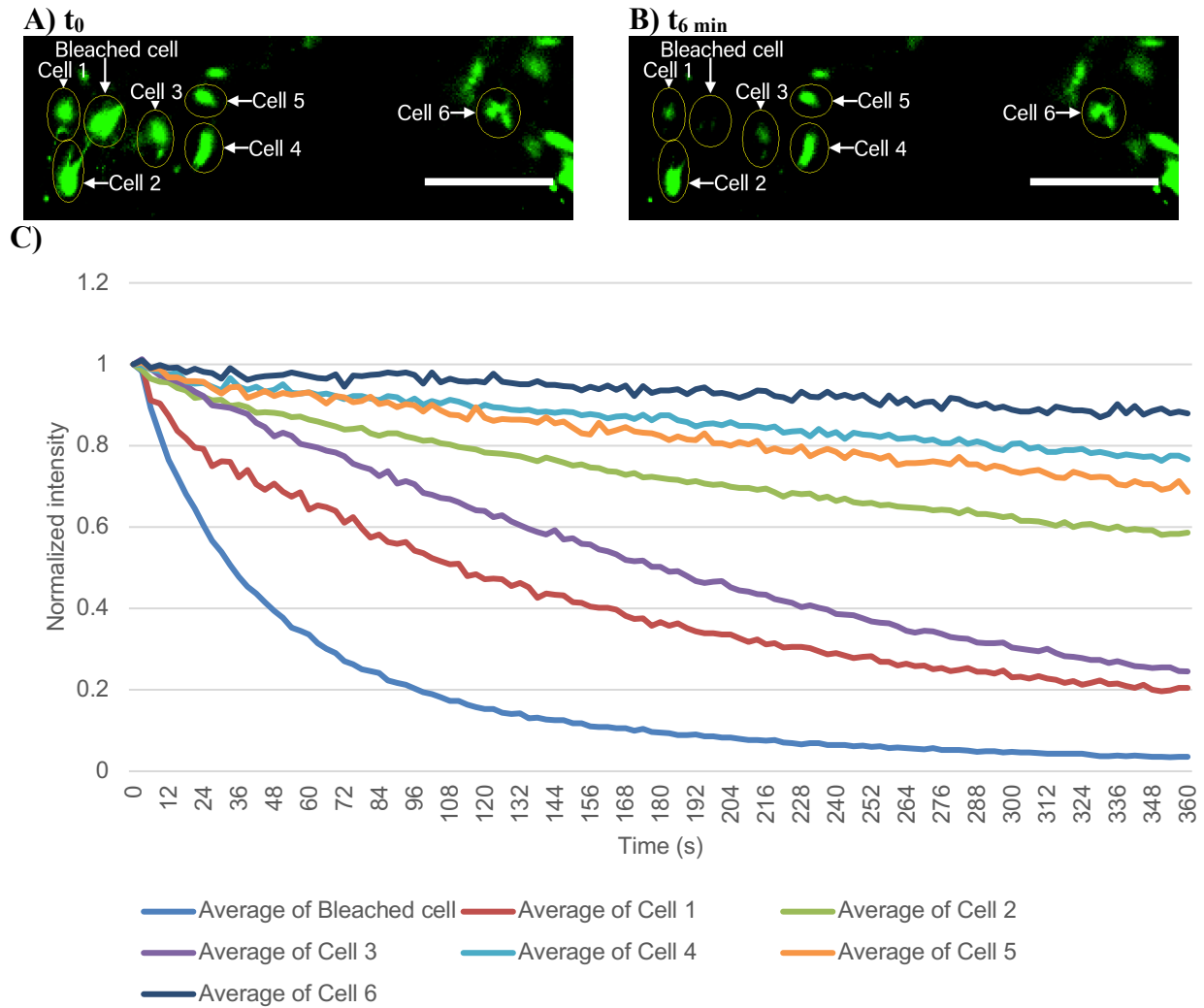


Figure 3.19: Round lamellar cells will all nearby neighbors communicating. Confocal images of round lamellar cells in the outer bovine annulus fibrosus before and after 120 FLIP imaging steps where all nearby neighbor cells to the photobleached target cell appeared to communicate with the target cell: **A)** $t = 0$; **B)** $t = 6 \text{ minutes}$. **C)** Fluorescent intensity profiles for labelled cells. Note how all three nearby-neighbor cells (cells 1, 2 and 3) exhibit drops in fluorescent intensity below all other cells. This image is therefore classified as having 3 of 3 nearby neighbors involved in intercellular communication. Scale bars represent 100 μm .

3.3.4.3 Spindle-shaped lamellar cells.

Spindle-shaped lamellar cells were typically clumped together in groups such that the target cell had up to five nearby neighbors according to the definition in Figure 3.5. Figure 3.20 shows an example of spindle-shaped lamellar cells where not all (1 of 3) nearest-neighbor cells appeared to communicate with the photobleached target cell, and Figure 3.21 shows an example

of interlamellar cells where all (3 of 3) nearest-neighbor cells appeared to communicate with the photobleached target cell.

In spindle-shaped lamellar cells, communication appeared to happen in all directions, including both along a linear cell array (see both cell 2s in Figures 3.20–3.21) and laterally between parallel cell arrays (see cell 1 in Figure 3.21). Table 3.4 shows signal-propagation results for all image sets of spindle-shaped lamellar cells that met the inclusion criteria of Figure 3.7 and where the imaging plane was aligned with the parallel annulus lamellae per Figure 3.3A (in the case of the imaging plane being perpendicular to the parallel annulus lamellae as in Figure 3.3B, the parallel sheets of spindle-shaped lamellar cells would theoretically appear only as lines, so these image sets were excluded from this analysis). A majority (12 versus 2) of eligible image sets demonstrated fluorescent intensity changes corresponding to intra-lamellar communication in both the longitudinal and lateral directions (such as in Figure 3.21) versus image sets where intra-lamellar communication appeared restricted to linear longitudinal cell arrays (such as in Figure 3.20) or did not clearly propagate beyond the photobleached target cell.

Table 3.4: Intra-lamellar signal-propagation patterns among spindle-shaped lamellar cells

Signal-propagation pattern	Count of FLIP image sets
Only photobleached target cell	1 (7%)
Longitudinal-direction only	1 (7%)
Lateral-direction only	0 (0%)
Both longitudinal and lateral	12 (86%)
Total	14 (100%)

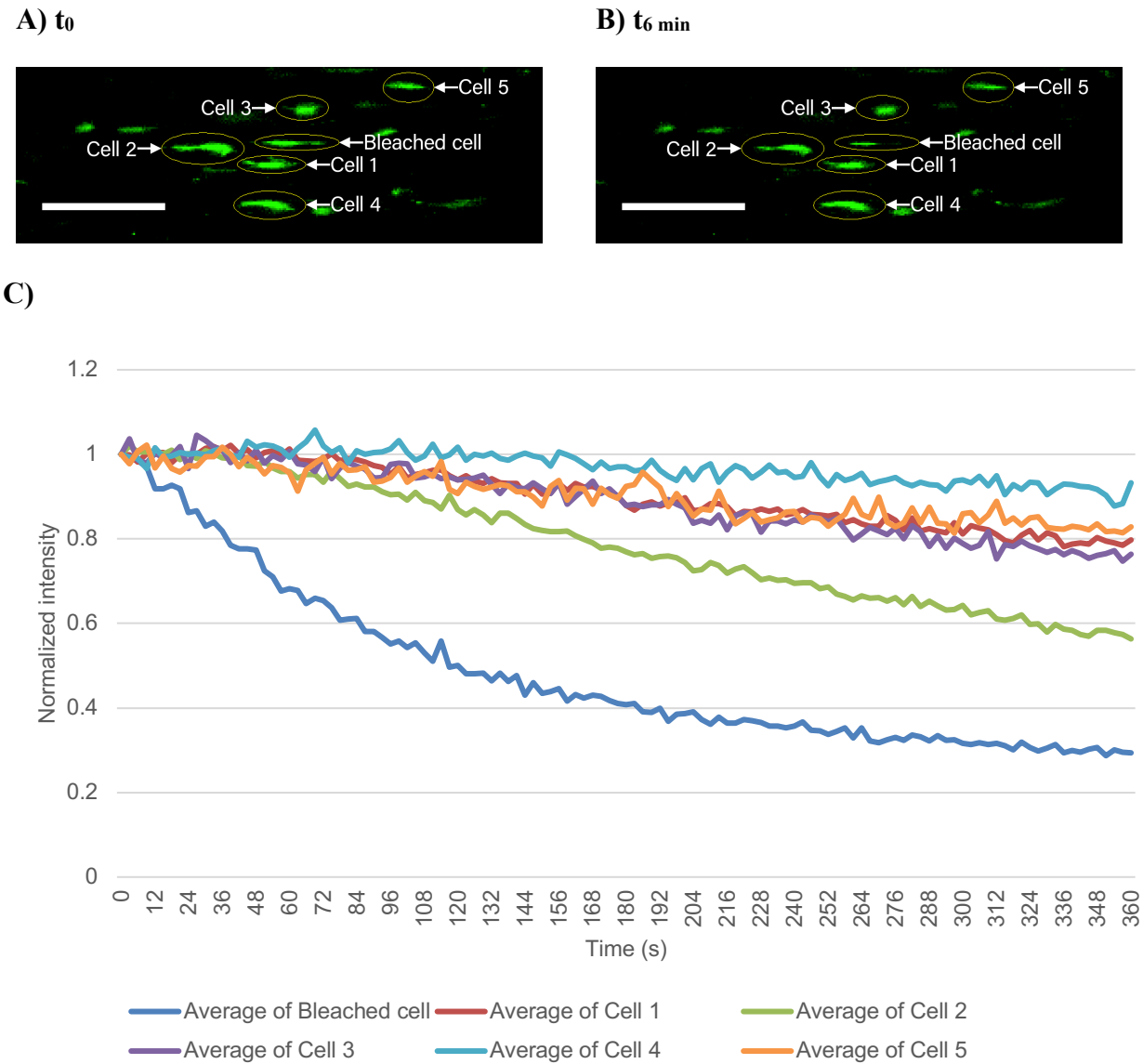


Figure 3.20: Spindle-shaped lamellar cells with only a fraction of nearby neighbors communicating. Confocal images of spindle-shaped lamellar cells in the outer bovine annulus fibrosus before and after 120 FLIP imaging steps where not all nearby neighbor cells to the photobleached target cell appeared to communicate with the target cell: **A)** $t = 0$; **B)** $t = 6$ minutes. **C)** Fluorescent intensity profiles for labelled cells. Note how cell 2 has a large drop in fluorescent intensity compared to all other cells. As cells 1, 2, and 3 are nearby neighbors to the target cell, this image is classified as having 1 of 3 nearby neighbors involved in intercellular communication, in the longitudinal direction only. Scale bars represent 100 μm .

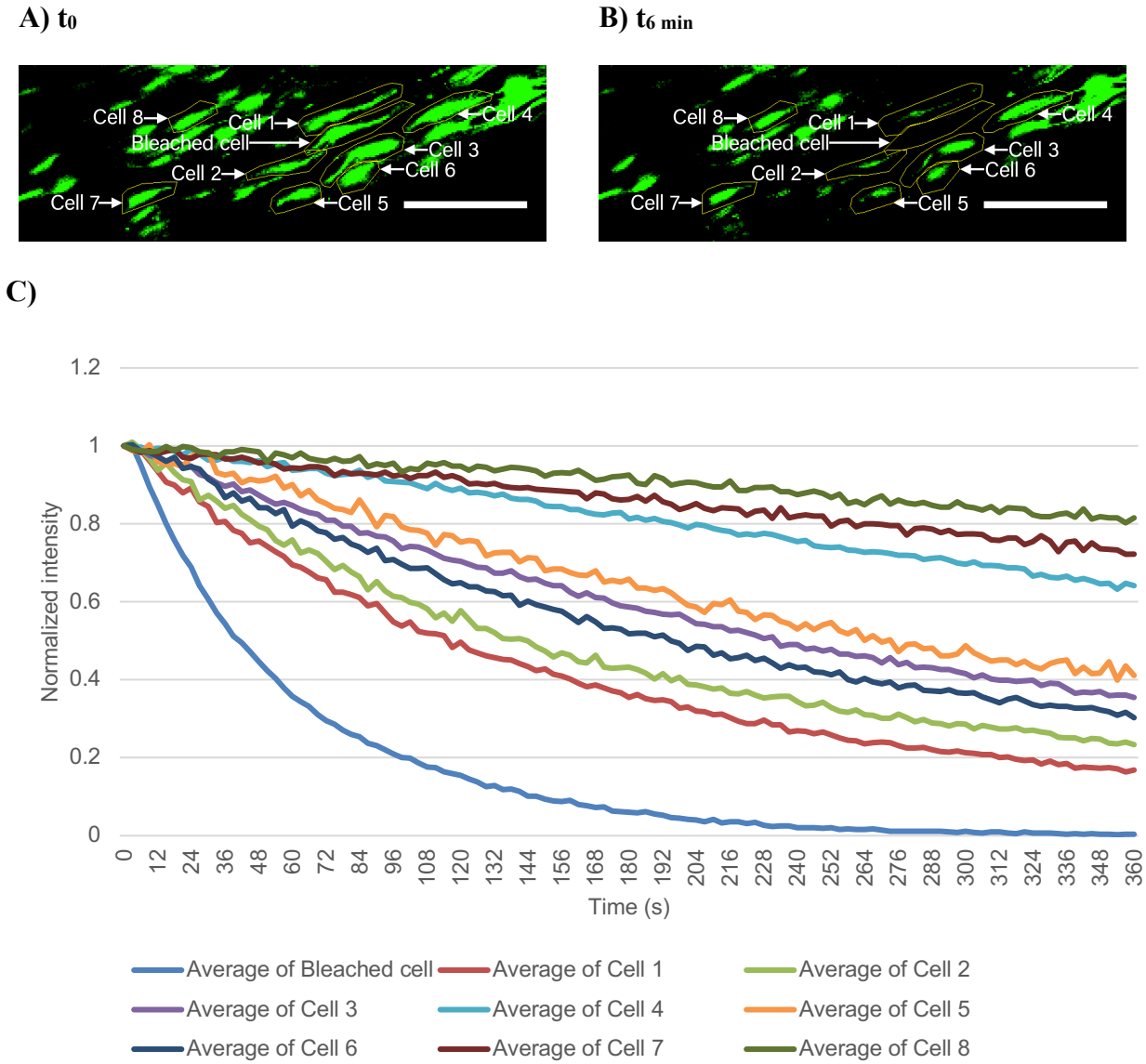


Figure 3.21: Spindle-shaped lamellar cells with all nearby neighbors communicating. Confocal images of spindle-shaped lamellar cells in the outer bovine annulus fibrosus before and after 120 FLIP imaging steps where all nearby neighbor cells to the photobleached target cell appeared to communicate with the target cell: **A)** $t = 0$; **B)** $t = 6$ minutes. **C)** Fluorescent intensity profiles for labelled cells. Note how all three nearby-neighbor cells (cells 1, 2, and 3) exhibit clear drops in fluorescent intensity below most other cells. This image is therefore classified as having 3 of 3 nearby neighbors involved in intercellular communication, in both longitudinal and lateral directions. Scale bars represent 100 μm .

3.3.4.4 Images perpendicular to the imaging plane.

To investigate intercellular signaling in the radial direction (from the nucleus pulposus toward the outer annulus fibrosus), a group of samples were imaged such that their parallel lamellae were perpendicular to the imaging plane (rotated 90° around their longitudinal axis) per Figure 3.3B. Intercellular signaling in the y-axis of these images (the vertical direction as printed on these pages) would therefore correspond to the radial direction. Figure 3.22 shows some spindle-shaped lamellar cells in such an orientation, where cells appear to be communicating in the radial direction (“2 of 2” responding vertical neighbors, per Figure 3.6). All three types of cell morphologies were found in the perpendicular image group; however, images of only one cell type, spindle-shaped lamellar cells, are shown in these results in order to minimize repetition.

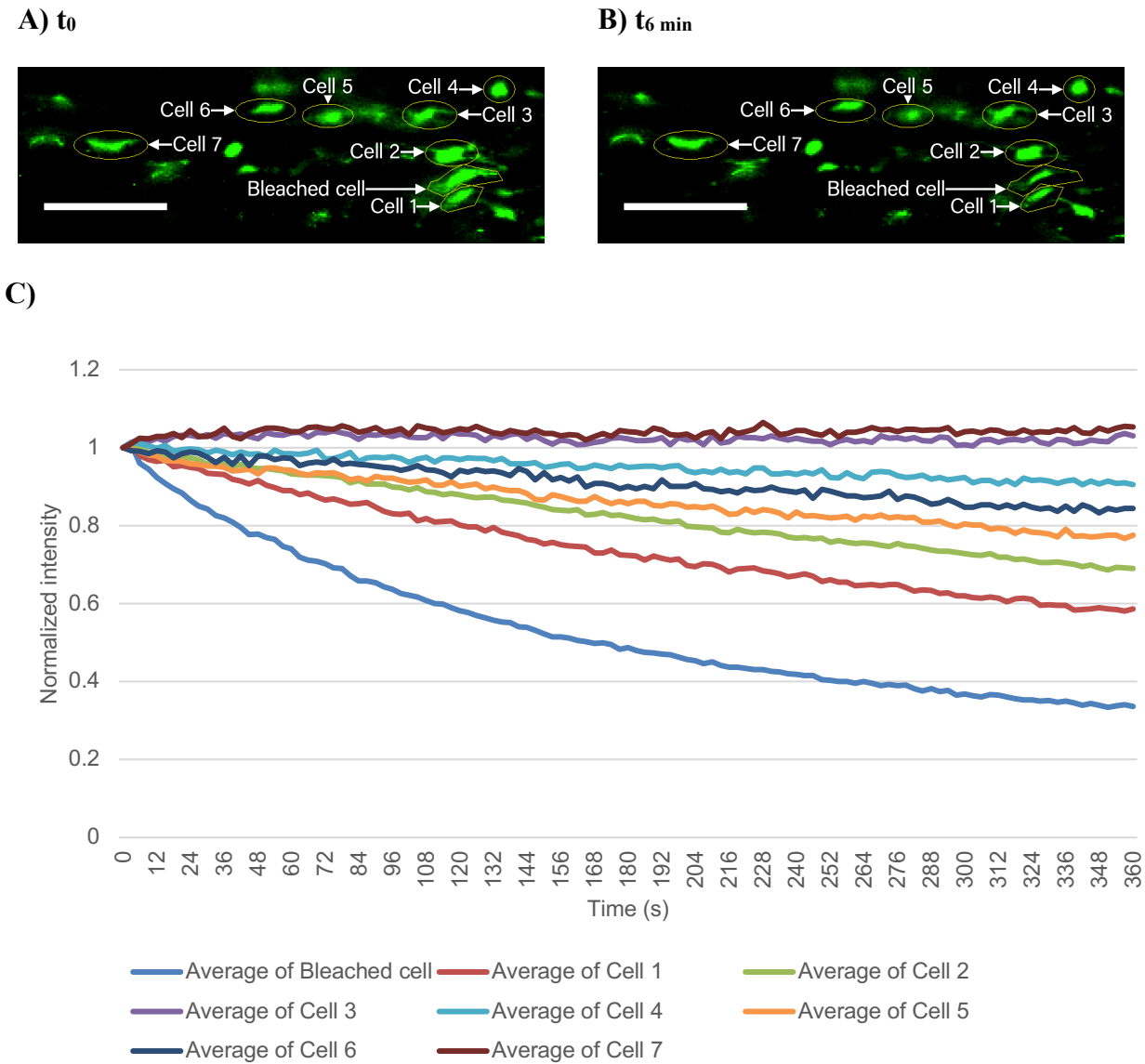


Figure 3.22: Radial-direction communication. Confocal images of spindle-shaped lamellar cells in the outer bovine annulus fibrosus before and after 120 FLIP imaging steps when the imaging plane is perpendicular to the disc lamellae (per Figure 3.3B): **A)** $t = 0$; **B)** $t = 6 \text{ minutes}$. **C)** Fluorescent intensity profiles for labelled cells. Note how cells 1 and 2 show the largest drops in fluorescent intensity, suggesting intercellular communication in the radial disc direction (normal to parallel lamellae; see Figure 3.6). Scale bars represent 100 μm .

3.3.4.5 Overall results, signal propagation.

Table 3.5 shows the overall signal-propagation patterns observed among the three different types of cell morphologies in the outer annulus from 111 FLIP images sets (94 image sets where the imaging plane was parallel to the annulus fibrosus lamellae, and 17 image sets where the imaging plane was perpendicular to the annulus fibrosus lamellae). In the majority of image series, irrespective of cell morphology, all eligible nearby cells to the photobleached target cell tended to exhibit fluorescent intensity drops indicative of intercellular communication with the target cell: image sets where none or only a fraction of eligible nearby neighbor cells appeared to communicate with the target cell numbered 27 (24%), while image sets where all eligible nearby neighbor cells appeared to communicate with the target cell numbered 84 (76%).

Table 3.5: Gap-junctional intercellular communication signal-propagation patterns among FLIP image sets from the outer bovine annulus fibrosus

Communicating Nearby Neighbors	Cell Morphology			Total
	Interlamellar	Round lamellar	Spindle-shaped lamellar	
0 or some but not all	9 (21%)	5 (26%)	13 (26%)	27 (24%)
All	33 (79%)	14 (74%)	37 (74%)	84 (76%)

Figure 3.23 details these signal-propagation results, organized by cell morphology and imaging-plane orientation. Note how most often all eligible nearby-neighboring cells (“1 of 1,” “2 of 2,” “3 of 3,” or “4 of 4,”) appear to be involved in intercellular communication with the target cell compared to fractional cases (e.g. “0 of 1”). The count for all cases not indicated (e.g. “2 of 3 interlamellar cells”) is zero.

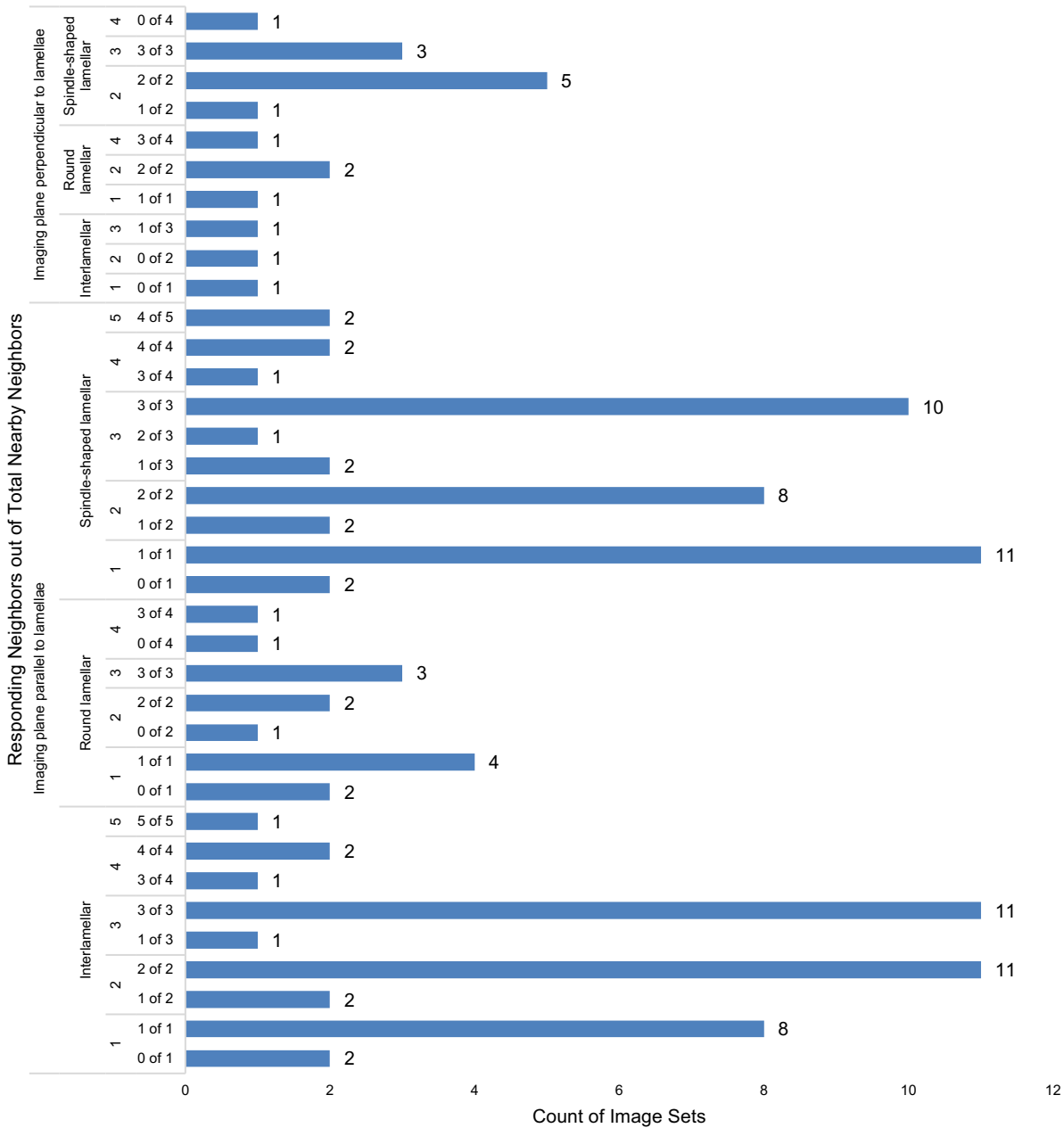


Figure 3.23: Gap-junctional intercellular communication signal propagation in the outer bovine annulus fibrosus. For each of the 111 FLIP image sets taken at different strain levels, the fraction of nearby neighbor cells (per Figure 3.5) appearing to communicate with the photobleached target cell was compared to the total number of communication-eligible nearby neighbor cells.

For radial-direction intercellular signal propagation, the perpendicular images were analyzed in terms of cells qualifying as “vertical neighbors” to the target cell per Figure 3.6. Of the 17 perpendicular FLIP image sets, most (12; 71%) appeared to involve all eligible vertical

neighbors (“1 of 1,” “2 of 2,” or “3 of 3”) in intercellular communication versus images sets where only a fraction of eligible vertical neighbors appeared to be involved in intercellular communication (5; 29%), as shown in Figure 3.24. Cases where “0 of 0” eligible vertical neighbors appeared to be involved in intercellular communication were excluded from analysis as no intercellular communication was expected or observed in these image sets in the vertical direction.

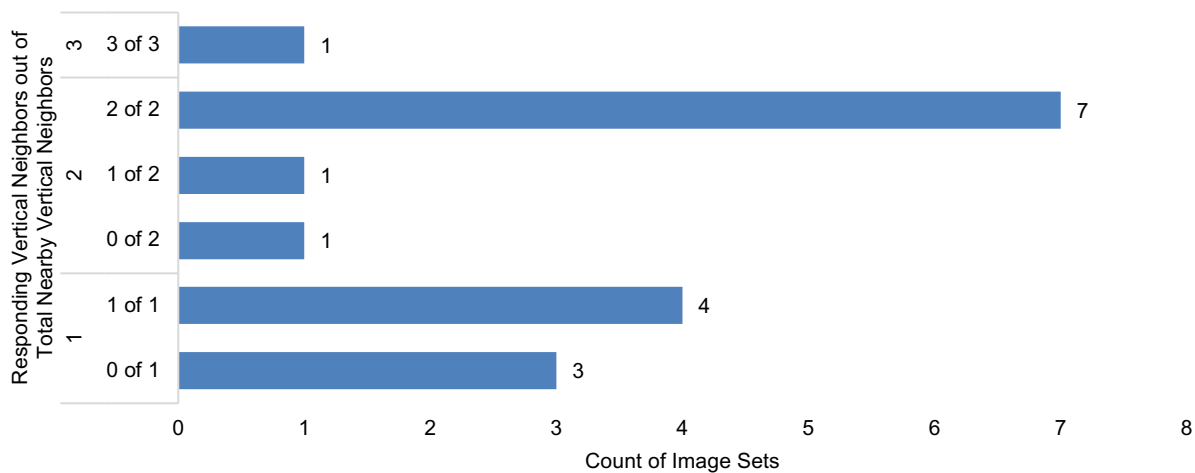
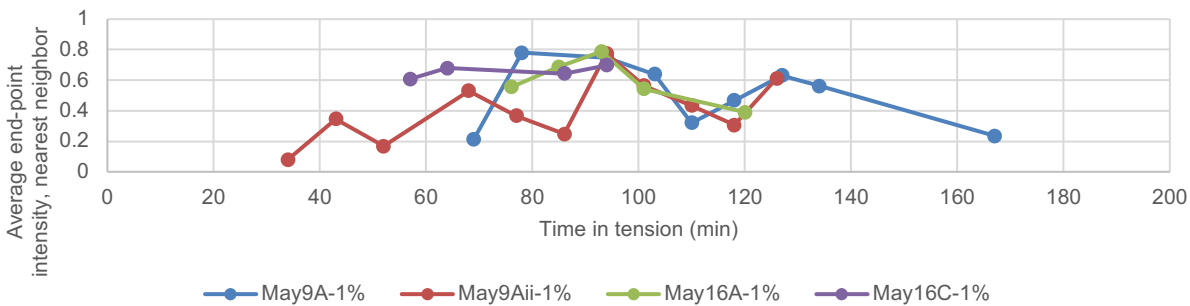
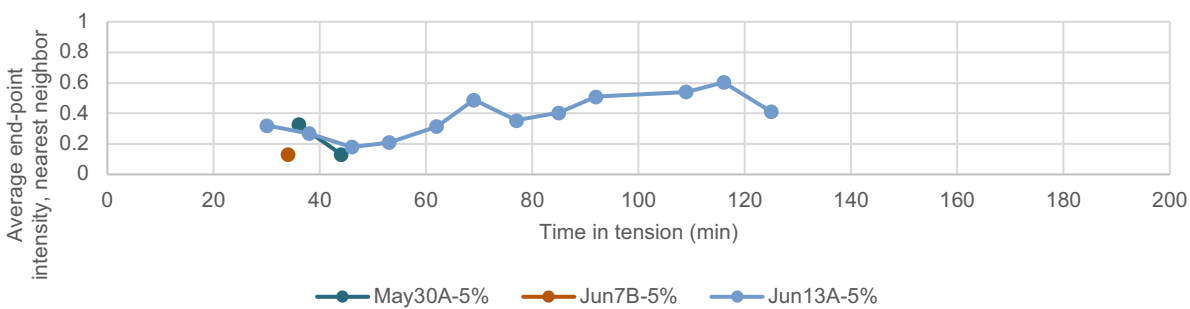
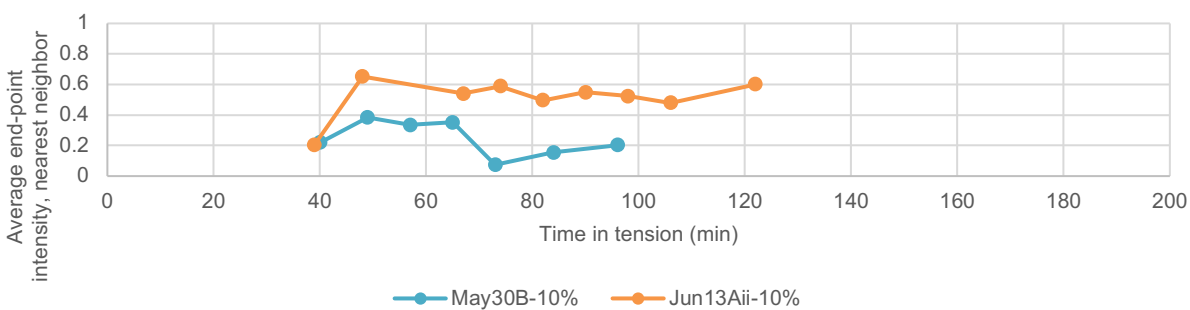


Figure 3.24: Radial-direction signaling results. For each of 17 FLIP image sets at 1% strain, the fraction of communication-eligible nearby vertical neighbor cells (per Figure 3.6) appearing to communicate with the target cell is compared to the total number of nearby vertical neighbor cells.

3.3.5 Time effects.

Multiple cell clusters were imaged from all of the 13 IVD strips across six different oxtails, with one exception: one IVD strip was imaged only once. Perpendicular FLIP image sets (Figure 3.3B) were excluded from this time-effect analysis in order to control the imaging-plane-alignment variable. Each strip sample was prepared, loaded at its respective tensile strain level, then imaged after allowing time for stress relaxation, with one to 14 image sets taken of different cell clusters. The time spent loaded in tension for each IVD specimen ranged from 30 min to 193

min. Figure 3.25 shows the average end-point intensity of the nearest-neighbor cell to the photobleached target cell across all different strain levels with open gap junctions (not chemically blocked). At 5% strain there appears to be a slight decrease in gap junction permeability (corresponding to the higher end-point fluorescent intensities with increasing time in Figure 3.25B) at around 100 minutes under tension. No clear trends were visible at other strain levels.

A) 1% strain**B) 5% strain****C) 10% strain**

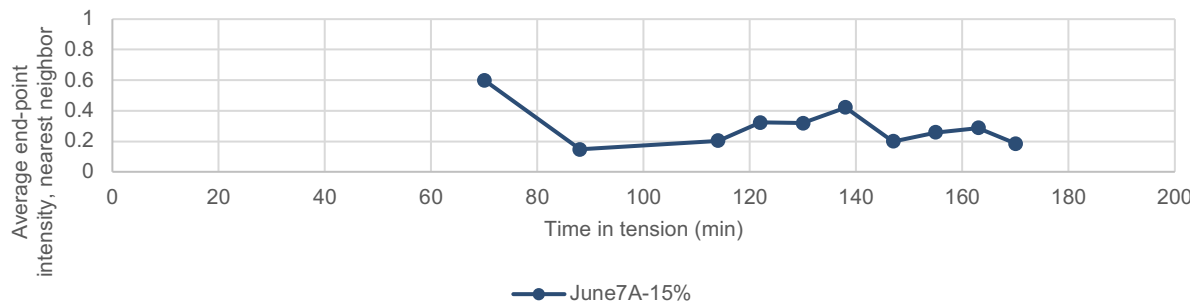
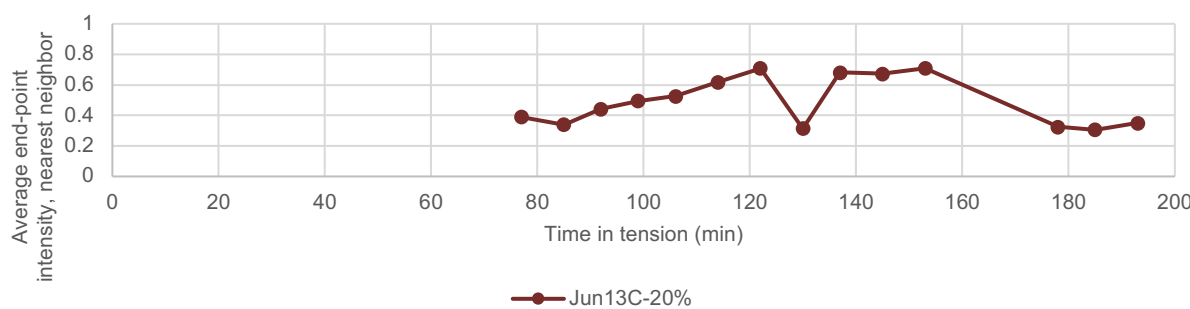
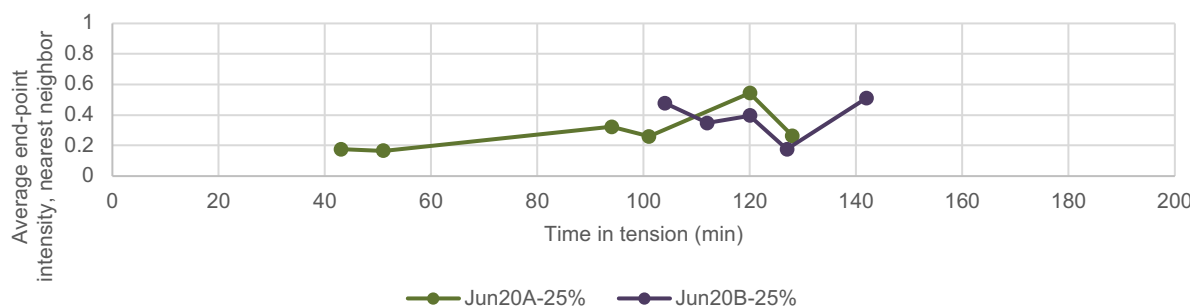
D) 15% strain**E) 20% strain****F) 25% strain**

Figure 3.25: Time effects on gap-junctional intercellular communication in IVD samples loaded in static tension. Each point represents one FLIP image set, and FLIP image sets from similar disc strips are connected by lines (e.g. 9 FLIP image sets of different cell clusters were taken in IVD specimen “May9A” at 1% strain, with increasing time spent in tension). End-point fluorescent intensities for nearest neighbor cells to the photobleached target cell are shown. Lower values indicate enhanced gap-junctional intercellular communication. **A) 1% strain B) 5% strain C) 10% strain D) 15% strain E) 20% strain F) 25% strain**

3.4 Discussion

3.4.1 Live-cell assay and cell morphology.

As calcein AM is designed to become fluorescent only upon esterase cleavage once inside a live cell, it is expected in confocal microscopy to see only viable cells (if anything) in a live tissue sample stained with calcein. In bovine annulus fibrosus samples prepared shortly after host separation, live cells were visible (Figure 3.8A), exhibiting spindle-shaped, round, and fusiform morphologies with long, branching processes. These morphologies were similar to other studies (Desrochers & Duncan, 2012; McMillan, 2009).

Live cells were not visible in a sample that had been frozen, thawed, and stained, as in Figure 3.8B. The small green dots in Figure 3.8B have a maximum diameter of about 5 µm and are too small to be live cells, nor does their process-free, round morphology correspond to the shape of live cells. The dots are likely imaging artifacts or small pockets of unbound dye that were not removed in the rinsing process.

Calcein AM therefore appears to be functioning as expected, fluorescently labelling the cytosol of live annulus fibrosus cells only.

Cells of the three known morphology types (spindle-shaped lamellar, round lamellar, and interlamellar) were found in the bovine annulus fibrosus. The distribution of cell morphology among these cells shows good agreement with the work of McMillan (2009), where spindle-shaped lamellar cells outnumbered round lamellar cells by roughly two to one. The split between interlamellar (39.3%) and lamellar cells (60.7%; both round and spindle-shaped) provided an approximately balanced representation of all cell categories in this study.

As shown in Figure 3.10, cells of different morphology can be found within close proximity of each other, particularly in the radial direction (normal to parallel annulus fibrosus lamellae), where annulus lamellae and interlamellar space alternate. Theoretically, spindle-

shaped lamellar cells are aligned in parallel linear arrays up to twelve cells long within an individual layer, with interlamellar cells occupying the interlamellar space between this and the next layer, which has a different fiber orientation per Figure 2.1 (Duncan, 2006). In practice, however, it was rare to find such well-defined cell clusters of lamellar-interlamellar interfaces, which is perhaps to be expected as cells make up only 1% of the disc by volume (Susan R.S. Bibby et al., 2001). It was much more common to find clumps of cells of mostly similar morphology.

3.4.2 1% strain.

As gap junctions are a physical coupling between adjacent cell membranes, intercellular communication through gap junctions will occur only among closely connected cells. In this study, the FLIP confocal microscopy technique was used to examine gap-junctional intercellular communication among interconnected cells in the outer bovine annulus fibrosus. When a specific target cell was repetitively photobleached using 100% laser power, its relative fluorescent intensity dropped from 1.0 down to an average of 0.124 (across 94 samples) over the course of six minutes. Variations in this end-point intensity could be explained by differences in imaging depth, which was estimated to be between 50–150 µm below the surface (see §3.2.4), where deeper cells could have been less affected by photobleaching. Adjacent cells located within a roughly one-cell-diameter distance (see Figure 3.5) of the photobleached target cell similarly experienced drops in fluorescent intensity, though less pronounced than in the target cell. To confirm that these intensity changes were the result of gap-junctional intercellular communication and not overall frame photobleaching or another phenomenon, control experimental groups involving no specific target-cell photobleaching as well as chemically blocked gap junctions were examined.

The non-photobleached control experimental group involved a collection of cells imaged using the FLIP protocol minus specific target-cell photobleaching (Figure 3.11). No major change was expected or observed between Figure 3.11A and B as no single cell was intentionally photobleached. This can be seen in Figure 3.11C, where all cells maintained fluorescent intensity profiles of around 1.0 over the experiment's six-minute run time. End-point intensities above 1.0 (such as Cell 1 in Figure 3.11, which had an end-point intensity of 1.074) could be due to measurement error or small amounts of z-drift. Observation of fluorescent dyes via confocal microscopy causes fluorescent-signal fading (Diaspro et al., 2006), and the imaging-laser power of 2% used in this protocol resulted in an average relative end-point intensity of 0.835 ± 0.021 (SEM) for all cells in this control group (1.0 would correspond to zero fading), suggesting slight fluorescent-intensity decay due to laser illumination during imaging. Laser illumination from imaging thus likely had a small contribution to observed fluorescent intensity drops in all cells; however, specific-target-cell photobleaching had a much more pronounced effect on both the target cell and its surrounding nearby-neighbor cells' fluorescent intensities that the effect of imaging-laser-fading was practically considered negligible. Overall fading effects would theoretically be uniform across the imaging field as well.

In the case of chemically blocked gap junctions using AGA, it would be expected to see a drop in fluorescent intensity in only the photobleached target cell, with all nearby neighboring cells maintaining high relative fluorescent intensities of around 1.0 as their fluorescently labelled cytosol would be unable to diffuse through the blocked gap junctions. A typical fluorescent intensity profile for this experimental group is shown in Figure 3.13, where only the photobleached target cell appeared to undergo a drop in fluorescent intensity. Cell 1 in this image is defined as the nearest neighbor to the target cell (per Figure 3.5) and maintained a high relative end-point intensity of 0.815. The average nearest-neighbor end-point intensity of 0.661 ± 0.047

in this group was significantly below ($p = 0.0048$) the average end-point intensity of cells in the non-photobleached control group (0.835 ± 0.021), suggesting that AGA as used in this experimental setup was capable of attenuating gap-junctional intercellular signaling but not completely eliminating it.

This is in line with some other results as AGA has been found to be only 60% effective at blocking gap-junctional conductance in mouse cardiac myocytes even at high concentrations of up to 100 μM , as used in this study (Rozental et al., 2001). Maeda et al. (2012), however, found no significant differences in fluorescent intensities between tendon cells in a non-photobleached control group and corresponding cells in an AGA-treated group using similar inhibitor-treatment methods as the current study (1 h incubation in 100 μM AGA). Perhaps this discrepancy is due to differences between rat tendon, mouse cardiac myocytes, and bovine annulus fibrosus. As tendon cells and bovine annulus fibrosus cells both exhibit high expression of connexin 43 (Gruber et al., 2001; Maeda et al., 2012), the imperfect blocking effect of AGA in the intervertebral disc versus the highly effective blocking effect in tendon is unlikely to be due to differences in the chemical structure of the gap junctions between both tissues. It could instead be attributed to differences in the extracellular matrix structure and composition or gap-junction concentration and localization. Desrochers and Duncan (2012) found imperfect chemical blocking of gap junctions in a complementary FRAP experiment in the bovine annulus fibrosus using 1-octanol, attributing the result to unbound stain, internal redistribution of unbleached calcein molecules within the target cell from outside the imaging plane, or ion leakage through the disrupted cell membrane after 1-octanol treatment. Possibly, it is harder for the aqueous AGA molecules (and other pharmacological gap-junction inhibitors such as 1-octanol) to effectively penetrate deeper into the annulus fibrosus extracellular matrix relative to tendon.

In the photobleached target cell, the average relative end-point fluorescent intensity was 0.097 in the AGA group, which was lower than the value of 0.144 in the absence of AGA. Maeda et al. (2012) found a larger difference in this target-cell relative-end-point intensity in a similar FLIP experiment in rat tendon: 0.05 with the presence of AGA, and 0.2 in its absence. While the difference in relative end-point fluorescent intensity between open and blocked gap junctions in the current study is small (~0.047), it does nonetheless suggest that the presence of AGA reduced entry of fluorescently labelled molecules into the photobleached target cell, thus resulting in its relatively lower end-point fluorescent intensity relative to the absence of AGA. Overbleaching is known to negatively affect cell viability (Hunter et al., 2004); however, the FLIP methodology used in this study perhaps does not necessarily require clear target-cell viability as in other fluorescence microscopy techniques like FRAP, where only the target cell's fluorescent intensity is measured. Given the similar end-point fluorescent intensities in the photobleached target cell in both tendon (Maeda et al., 2012) and the current study, it is assumed that target-cell viability is not essential to these results. Perhaps future experiments could examine fluorescent return into the target cell after performing the FLIP protocol.

Gap junctions are generally considered able to allow the passage of molecules up to 1 kDa in size (Simon & Goodenough, 1998). Calcein AM is 994.86 Da (1 Da = 1 g/mol) and is thus theoretically able to pass through gap-junction channels when they are open. Calcein has been used extensively in the study of gap junctions and the movement of molecules through them (Chi et al., 2004, 2005; Desrochers & Duncan, 2012; Maeda et al., 2012, 2017; Maeda & Ohashi, 2015; McMillan, 2009; Suadicani et al., 2004; Sugawara et al., 2011). While connexins 43 and 45 have both been found in the disc (Gruber et al., 2001), the movement of calcein molecules is likely through connexin-43 gap junctions as connexin 45 is known to form gap junctions with a pore size smaller than 0.3 kDa (Stains & Civitelli, 2005). Gap junctions formed

by other connexin isoforms (connexins 26, 37, and 40) demonstrated minimal or no passage of Alexa dye molecules up 0.760 kDa (P. A. Weber, Chang, Spaeth, Nitsche, & Nicholson, 2004), further supporting connexin-43 gap junctions as the dominant channel for calcein movement.

The AGA-blocked experimental group in conjunction with the open-gap-junction experimental group indirectly suggest that at 1% strain, calcein molecules can freely diffuse between gap-junction-connected cells. As gap junctions often aggregate together in populations known as plaques containing a few to thousands of units (Goodenough & Paul, 2009), the diffusion of individual calcein molecules between adjacent cells likely occurs across thousands of individual gap junctions. Intracellular diffusion (internal movement within a cell) of calcein is much higher than intercellular diffusion through gap junctions, with diffusion coefficients of $26.08 \mu\text{m}^2/\text{s}$ and $1.23 \mu\text{m}^2/\text{s}$, respectively, in rabbit tendon (Maeda & Ohashi, 2015). Comparably, in normal rat kidney cells, the diffusion coefficient for calcein moving through connexin-43 gap junction channels was $0.8 \mu\text{m}^2/\text{s}$ (Bathany, Beahm, Felske, Sachs, & Hua, 2011). Similar rates would likely be expected in annulus fibrosus cells; however, the variability in cell morphology (and thus volume) and orientation make it challenging to mathematically model calcein's diffusion coefficients with the data from this study.

Qualitatively, it is suggested that lower end-point fluorescent intensities in nearby-neighboring cells (ranging from 0.081 up to 0.787, per §3.3.2.2) correspond to higher diffusion rates. Thus, nearest-neighbor cells (which had the lowest end-point intensity of all nearby-neighboring cells) likely demonstrated the highest rates of diffusion into the target cell. As connexin-43 hemichannels have been found to be distributed extensively and non-preferentially across annulus cell bodies and processes (Bruehlmann et al., 2002; Duncan, 2006), this higher rate of diffusion is perhaps a result of larger cell–cell contact area with the target cell across membranes or processes, assuming an approximately uniform connexin-43 gap-junction density.

The exact location of functional gap junctions (two opposing, docked connexin-43 hemichannels from adjacent cells) between interconnected bovine annulus cells has not yet been fully discerned (Desrochers & Duncan, 2012). Interestingly, in Figure 3.19 a clearly visible process exists between cell 2 and the target cell, which disappears over time. If diffusion occurred through this process from cell 2 into the target cell, it would be expected to see increasing fluorescence in this process over time, confounding the notion of diffusion occurring through gap-junction-connected processes. Future investigation is required to determine exactly where the functional connexin-43 gap junctions are located on annulus cell membranes.

In addition to pharmacological blockers, gap-junction permeability is known to be affected by mechanical load (Desrochers & Duncan, 2012; Maeda et al., 2012). The effect of mechanical load on gap-junction permeability will be discussed in more detail in the next section (§3.4.3).

FLIP image sets in this experiment were taken at room temperature, approximately 22°C, which is below the physiological temperature of 37°C, a limitation of the current study. Gap-junction intercellular communication has been previously reported at around 21–22°C, however (Chi et al., 2004, 2005; Desrochers & Duncan, 2012; Guilak et al., 1994). As diffusion scales linearly with temperature (Houtsmuller, 2005), performing FLIP experiments in the annulus fibrosus at physiological temperatures could be a useful future direction for this study.

Only cells within a similar z-plane were analyzed in these FLIP image sets. As described in the methods section (§3.2.6), only cells that were oversampled in triplicate in the z-direction were analyzed for fluorescent intensity changes. Such cells thus shared similar z-plane alignment with the target cell. Given the ability of FLIP to study intercellular signal propagation among interconnected cells, the question of out-of-plane signaling arises: could cells connected to the target cell but in different z-planes also be involved in communicating with the target cell? Out-

of-plane signaling, however, such as from cells directly above or below the target cell, is unlikely to be accurately detected in this case, as the hourglass-shaped confocal beam (per Figure 2.4A) would photobleach any such cells with similar laser power as the target cell (this intensity is highest closest to the target-cell plane and diminishes with increasing distance in the positive and negative z-directions). Furthermore, it has been demonstrated in a fluorescence-recovery experiment (FRAP) that only lateral (and not axial) diffusion contributed to fluorescence recovery inside a bleached region (Blonk, Don, Van Aaslt, & Birmingham, 1993). For this reason, these image sets must be considered two-dimensional, and this particular data set cannot make any inferences as to intercellular signaling in the direction normal to the parallel annulus fibrosus lamellae. Intercellular signaling in such a direction will be discussed in §3.4.4.

A drop in fluorescent intensity in cells nearby to the photobleached target cell is therefore likely indicative of intercellular communication between these adjacent, interconnected cells via functional connexin-43 gap junctions. In the experimental groups with open gap junctions, a fluorescent intensity drop was frequently observed in one or more of the cells nearby the photobleached target cell. Signaling patterns among these neighboring cells, a major goal of the current study, will be discussed in §3.4.4.

3.4.3 Higher strain levels.

This study examined the effect of different strain levels on gap-junctional intercellular communication in the bovine annulus fibrosus, ranging from low to extreme. Circumferential strips of annulus tissue were loaded in uniaxial tension at 1, 5, 10, 15, 20, and 25% strain, with the only finding being a slight increase in gap-junction permeability in the 15% strain group per Figure 3.15.

A nearest-neighbor end-point fluorescent intensity of 1.0 in Figure 3.15 would suggest that zero gap-junctional intercellular signaling had occurred: the nearest-neighbor cell to a

photobleached target cell would have maintained all of its fluorescent intensity, with none of its fluorescently labelled calcein molecules diffusing into the nearby target cell. A relative end-point fluorescent intensity of 0 in the same figure would suggest a high amount of gap-junctional intercellular signaling as the nearest-neighbor cell would have thus lost all of its fluorescent calcein molecules through gap-junction-facilitated diffusion into the target cell.

The results for nearest-neighbor end-point fluorescent intensities for these five different strain levels, from 1%, where samples were loosely held in place with minimal apparent tension, up to 25%, where samples were quite taut and visibly stretched, all fell around 0.42 (the overall mean was 0.421 ± 0.019), suggesting fairly minimal differences in gap-junction permeability, at least as detected using this experimental methodology. At 1% strain, gap-junctional intercellular signaling remained relatively low, which appeared as a high nearest-neighbor mean end-point fluorescent intensity (0.508) compared to other strain levels. Moderate strain levels (5, 10 and 15%) all had lower nearest-neighbor end-point fluorescent intensities than 1% strain (0.346, 0.397, and 0.294, respectively), suggesting a minor increase in gap-junction permeability at these strain levels, but with statistical significance only in the case of 15% strain ($p = 0.019$ relative to 1% strain). As residual strains exist in the intact disc of up to 8.3% (Duclos & Michalek, 2017), accurate comparisons between the linear tensile strains used in this study and *in situ* circumferential strains are difficult to perform. Perhaps at 15% strain strips were loaded at a level corresponding to a physiological value that optimizes gap-junction permeability. Maeda and Ohashi (2015) found a statistically significant increase in gap-junction permeability in rabbit tendon at a physiological strain level of 4% relative to 0% (and a subsequent decrease at the higher-than-physiological strain level of 8%), attributing the enhancement in permeability to an opening of gap-junction pores in response to mechanotransduction events. Desrochers and Duncan (2012) found a reversible reduction in gap-junction communication in the intact

intervertebral disc under high flexion loads: communication was reduced during high flexion of spinal motion segments but returned to normal levels after load removal.

At strain levels of 20 and 25%, it would be expected to see high nearest-neighbor end-point fluorescent intensities, indicating a reduction in gap-junction permeability; however, no such change could be observed with any statistical power. The 20% strain group demonstrated a slight decrease in gap-junction permeability relative to 15% strain (corresponding to a higher mean end-point intensity of 0.491 versus 0.294); however, perhaps unexpectedly, 25% strain had a lower mean end-point intensity than 20% strain (0.421). Low sample size could be a contributing factor to these unclear results.

Some variability was observed in the photobleached target cell's mean end-point fluorescent intensities among the different strain-level groups: at 1% strain, the mean target-cell end-point intensity was 0.149, while at 5, 10, and 15% strain, the mean target-cell end-point intensity drops to 0.056–0.066, before increasing to 0.190–0.214 at 20 and 25% strain (Table 3.3). As discussed in the previous section (§3.4.2), the target cell's mean end-point intensity was lower when gap-junction-blocker AGA was used (0.097) compared to in its absence (0.144), so some effect of mechano-regulation could perhaps manifest as changes in mean target-cell end-point fluorescent intensities. A higher target-cell end-point intensity would theoretically correspond to enhanced gap-junction permeability. Taking the nearest-neighbor end-point intensity and subtracting the target-cell end-point intensity in each FLIP image set (a means of comparing the largest fluorescent-intensity difference between a target cell and its corresponding nearest-neighbor within a given image set), however, resulted in no statistically significant differences between any of the strain-level groups. Interestingly, at 15% strain, the target-cell mean end-point intensity was the lowest (0.056) among all strain levels, which theoretically corresponds to inhibited gap-junction permeability, thus contradicting the earlier notion of 15%

strain having enhanced gap-junction permeability (per comparing only nearest-neighbor end-point fluorescent intensities). The nearest-neighbor end-point intensity, however, is likelier a stronger indication of gap-junction permeability than the target cell's end-point intensity as the FLIP protocol specifically examines adjacent cells for fluorescent intensity changes. Only considering the target cell's intensity would be similar to a FRAP experiment (see §2.5).

While the uniaxial-strain methodology used in the current study was helpful for accurately and consistently measuring linear tensile strain among different intervertebral disc strips, it did not provide an accurate representation of true physiological loading conditions, which is a likely factor in these ambiguous results. As applied to the excised disc-strip samples, uniaxial tension corresponds to hoop stress in the circumferential direction of *in situ* discs, which is only one aspect of normal physiological loading. Collagen fibers in the annulus fibrosus bear load primarily through tension (as opposed to compression), and collagen-fibril-sliding is the main form of macro-scale deformation, with high shear loads appearing in the interlamellar space (Hsieh & Twomey, 2010). At the edge of each disc strip prepared in this experiment, collagen fibers were cut where they would have otherwise been securely anchored into the vertebral bodies (Inoue, 1981; Newell et al., 2017). Loading disc strips in uniaxial tension is thus along a direction oblique (up to 30°) to both alternating collagen-fiber directions of the concentric lamellae (consider the circumferential direction in Figure 2.1). Fibril sliding likely occurred to some degree as samples elongated under tension while becoming thinner, though this deformation would have been affected by the cut ends of the collagen fibers. It is possible that even at high tissue strains of 25%, annulus cells were still relatively unloaded versus the *in situ* environment. Perhaps this is an explanation for not seeing a clearly detectable reduction in gap-junction permeability at high strain levels. In the intact disc, macroscale strain redistributes as it

translates down to the cellular scale (Desrochers & Duncan, 2010), another effect that was not controlled for with the disrupted extracellular matrix in this study.

Horizontal drift would likely be present as x-translation in FLIP images sets if major sample slippage had occurred while the image set was being collected. A set of clamps were machined for this experiment that were designed to securely clamp the tissue samples. Slippage can be an issue at high tissue strain levels, like the 20 and 25% used here. This would correspond to x-translation (see Figure 3.3A) in the time-series images of a given cell cluster, either in the positive or negative x-direction, depending on the cell cluster's relative orientation to the overall sample x-centroid (it was highly likely that there was at least some x-direction discrepancy between a given cell cluster its corresponding sample x-centroid given the small 425.10 μm image width within the much larger 30–60 mm-long sample): for example, a cell cluster located in the positive x-direction from the sample x-centroid would move in the negative x-direction closer toward the sample's x-centroid if tissue slippage had occurred at either clamp, thereby relaxing the sample's tension. X-translation appeared negligible in all image sets, indicating minimal slippage, which was also confirmed by visual inspection.

AGA-gap-junction-blocked FLIP experiments were performed only at 1% strain in the current study, where AGA was found to be effective at attenuating but not completely inhibiting gap-junctional intercellular communication (see §3.4.2). At higher strain levels, it was therefore assumed that observed fluorescent-intensity changes in FLIP image sets were in response to gap-junction intercellular communication. It is likely that AGA would reduce gap-junction intercellular communication at higher strain levels too; however, such experiments were not performed. Other studies have performed gap-junction-inhibited experiments at higher load levels but with fewer loaded groups (one or two but not six) (Desrochers & Duncan, 2012; Maeda & Ohashi, 2015). Given the unclear effect of high strain in the current study (with

perhaps the one statistically significant difference between the 1 and 15% strain groups and no clear disruption of gap-junction permeability at high strain levels), it is unlikely that the use of AGA-blocked experimental groups at higher strain levels would have further elucidated these results.

In summary, gap junction permeability can be affected by mechanical load. In this study on the annulus fibrosus, 15% strain was shown to enhance gap-junction permeability, though, perplexingly, high strain levels (20 and 25%) did not appear to reduce gap-junction permeability, as would have been expected. In the disc (Desrochers & Duncan, 2012) and tendon (Maeda & Ohashi, 2015), high mechanical loads have previously been shown to inhibit gap-junction communication. Lower-than-physiological loads may similarly reduce gap-junction permeability (Maeda & Ohashi, 2015), suggesting an optimum loading magnitude for maximum gap-junction permeability. Such an effect was perhaps observed in this study, with maximal gap-junction permeability at 15% strain, though this conclusion comes with the caveat of the altered mechanical-loading environment (disc strips instead of intact disc tissue), which may also explain the lack of disruption in gap-junctional intercellular communication at high strain levels.

3.4.4 Signal propagation.

Signal propagation of intercellular-messaging molecules in other connective tissues has been found to exhibit non-homogeneous behavior. In tendon, collagen fibers run parallel to the main tensile longitudinal axis, with tenocytes aligned along these collagen fibers. While tenocytes are connected both longitudinally and laterally via gap junctions (McNeilly, Banes, Benjamin, & Ralphs, 1996), it was found that the predominant intercellular communication was between cells within a given row (aligned along the same longitudinal collagen fiber), rather than between rows (Maeda et al., 2012). Ligament also demonstrated gap-junction localization to only areas of close cell-cell contact (Chi et al., 2005). In bone, where many different cell types exist,

it was found that intercellular calcium signaling propagated more strongly toward bone surface cells than between or toward bone-matrix-embedded osteocytes, suggesting coordination between osteocytic mechanosensing and bone-surface-modeling activity (Adachi, Aonuma, Taira, et al., 2009).

With the unique tissue organization of the annulus fibrosus, concentric layers of collagen fibers at alternating orientations and cells distributed both within and between these lamellae (see §2.1.1), the hypothesis of this study was that similarly asymmetrical patterns of intercellular communication could exist in the disc. The FLIP confocal-microscopy protocol was used to photobleach a target cell and to examine the movement of fluorescently labelled calcein molecules from nearby neighboring cells into this target cell.

Cells were separated by morphology (spindle-shaped lamellar, round lamellar, and interlamellar) as signaling patterns could possibly be different within these three classes. All strain-level groups were combined in this investigation on signal propagation as there were minimal differences between the different strain-level groups with regard to gap-junction permeability, as previously discussed (§3.4.3). With all three cell morphology types, it was found that gap-junction intercellular signals into a photobleached target cell tended to come from nearby-neighboring cells in all directions, with no clear directional biases. As shown in Figure 3.23, the majority of intercellular-communication signaling patterns with the target cell appeared to involve most if not all eligible nearby neighbors, irrespective of cell morphology. Images where only a fraction of eligible nearby neighbor cells to the target cell, such as “1 of 2” or “2 of 4” cells appeared to be involved in intercellular communication, were outnumbered 84:27 (76% to 24%) by images where every eligible nearby neighbor appeared to be involved in intercellular communication. Accordingly, the sub groups of fractional responses were all lumped together rather than being further subdivided.

Interlamellar and round lamellar cells tended to be clustered together in groups of two to six cells in close proximity (see Figures 3.16–3.19) such that their membranes or processes could be connected to a target cell by gap junctions. Usually, all of these nearby-neighbor cells appeared to be involved in communication with the target cell.

The lack of clear directional biases in signal-propagation is remarkable in the case of spindle-shaped lamellar cells. Spindle-shaped lamellar cells typically appeared as parallel rows of linear arrays (see Figures 3.20–3.21). With this highly organized layout versus the more random cell distribution of interlamellar and round lamellar cells, signal-propagation patterns specific to spindle-shaped lamellar cells were examined. Photobleaching a given spindle-shaped-lamellar target cell would usually correspond to a fluorescent intensity drop in all surrounding cells, both in cells along the same linear array (such as cell 2 in Figure 3.21) and in cells located in adjacent parallel arrays (such as cell 1 in Figure 3.21). Of the 14 FLIP image sets containing spindle-shaped lamellar cells that met the inclusion criteria for intra-lamellar signal-propagation analysis (per Figure 3.7), 12 showed fluorescent-intensity changes indicative of both longitudinal and lateral intra-lamellar communication (see Table 3.4), suggesting no clear signal-propagation non-homogeneities. As hypothesized, signaling could have been restricted to a given longitudinal linear array without crossing to lateral arrays; however, these findings do not support such a signaling pattern.

This finding is in contrast to both tendon and ligament. In tendon, cells aligned in parallel linear arrays almost exclusively communicated along the longitudinal axis of each array but not laterally between adjacent arrays (Maeda et al., 2012). Connexin 43 was found to be localized to such longitudinal cell–cell interfaces within a given fiber according to confocal immunofluorescence, while connexins 26 and 32, also protein subunits capable of forming gap junctions, were more diffused in their localization pattern (Maeda et al., 2012).

Ligament has a similar organization to tendon: cells are generally aligned in rows parallel to the main longitudinal tissue axis (Bray et al., 2005; Chi et al., 2005). Chi et al. (2005) found these cells to be relatively sparse and to express functional connexin-43 gap junctions primarily in areas of cell-cell contact along the longitudinal axis of a cell row, reflecting a similar bipolar nature to tendons cells.

Given the extensive, non-localized distribution of connexin 43 across annulus fibrosus cell bodies and processes (Bruehlmann et al., 2002; Duncan, 2006), it would perhaps be surprising to find a bipolar or similar signal-propagation pattern in the disc, which is consistent with this study's result of intercellular signaling being possible in all directions among interconnected cells if they are in close enough proximity to each other.

To investigate radial-direction (the z-direction per Figure 3.3A) intercellular communication, such as communication between cells in a single lamella and adjacent interlamellar cells, two-photon excitation laser-scanning microscopy was initially attempted. Per Figure 2.4A, specific target-cell photobleaching using one-photon excitation bleaches the target cell and all other cells above and below this target cell within the three-dimensional hourglass-shaped laser beam (with fading intensity as the z-distance from the target cell increases). Thus, in one-photon excitation, repeatedly bleaching a specific target cell and capturing z-stacks of surrounding cells would not permit effective investigation of radial-direction intercellular signaling as fluorescent intensities in the z-direction would be affected by out-of-plane photobleaching.

Two-photon-excitation laser-scanning microscopy (see Figure 2.4B) could theoretically permit a target cell to be repeatedly photobleached while capturing z-stacks to track fluorescent-intensity changes in three dimensions. Due to the highly localized fluorescence excitation volume in two-photon excitation (sub-femtoliter), planes above and below the target cell's plane

would not be subject to out-of-plane photobleaching as in one-photon excitation (with its much larger hourglass-shaped laser beam). In practice, however, target-cell photobleaching using two-photon excitation was ineffective as it proved challenging to significantly reduce the fluorescent intensity of the target cell within a suitable time frame (such as the six minutes used here in one-photon excitation). Even with the target cell bleached at 100% laser power and the maximum laser-dwell time (173 μ s) over the bleached ROI, intensity changes in the target cell were negligible. Extending experiment run time could perhaps mitigate this issue; however, it is speculated that run time would need to be increased at least fivefold or more, making such experiments impractical. Additionally, two-photon excitation required a relatively thin optical slice thickness of 1.4 μ m, wherein z-plane image drift became an issue again (it had previously been mitigated by using a thicker optical slice via increased pinhole diameter in one-photon excitation).

The sub-femtoliter fluorescence excitation volume in two-photon excitation gives it effective subcellular resolution (Rubart, 2004). Unfortunately, the much larger volumes of entire bovine annulus fibrosus cells (roughly $20 \times 10 \times 10 \mu\text{m}^3$) were likely too large to be significantly affected by even high-laser-power photobleaching over extended time periods with the two-photon-excitation laser. With these issues, the two-photon-excitation approach for investigating radial-direction signaling was not pursued any further.

Instead, bovine annulus fibrosus disc strips were rotated 90° around their longitudinal axis such that their parallel lamellae were perpendicular to the microscope imaging plane (Figure 3.3B). One-photon excitation was again used to run FLIP experiments and examine intercellular signal propagation. In this perpendicular group, intercellular signaling in the y-axis of these images (the vertical direction as printed on these pages) corresponds to the radial direction (normal to parallel annulus lamellae). Per Figure 3.24, it was found that in these perpendicular

FLIP image sets, a majority of image sets appeared to involve all eligible vertical neighbors (12 versus 5) in intercellular communication versus image sets where only a fraction of eligible vertical neighbors appeared to be involved. This suggests that intercellular signaling can propagate in the radial disc direction. If less perpendicular FLIP image sets appeared to be involved in such radial-direction intercellular communication, it would suggest that intercellular communication was in some way restricted, perhaps to within a given annulus lamellae; however, the lamellar–interlamellar interface was often poorly defined. A well-defined lamellar–interlamellar transition as in Figure 3.10 was rare to find even when the imaging plane was parallel to the annulus lamellae (as in Figure 3.3A), appearing in only a few of these FLIP image sets, and no such transition was clearly evident in any of the perpendicular FLIP image sets (as in Figure 3.3B). Signaling patterns at lamellar/interlamellar interfaces thus remain unclear, though radial-direction signaling does nonetheless appear possible according to these results.

It was challenging to accurately determine cell morphology in the perpendicular FLIP image sets as spindle-shaped lamellar cells could theoretically appear incorrectly as round in the two-dimensional viewing plane, while they could actually be circular slices of elongated, spindle-shaped cells. Furthermore, the perpendicular FLIP image sets were collected by imaging through the cut annulus fibrosus lamellae, with extracellular matrix disruption likely at even the maximum imaging penetration depth of about 150 µm due to the rougher surface compared to the non-perpendicular FLIP image sets, where the surface was only scraped clean. Even a clear result here would thus still not represent true physiological conditions.

In rare cases, drops in fluorescent intensity along chains of three interconnected cells were observed, with intensity drops in the target cell, a nearby neighbor, and a third cell connected to the nearby-neighbor cell only (and not directly to the target cell), suggesting signal propagation along the chain of cells. In a similar FLIP experiment in tendon, where cells form

even, linear arrays, intercellular signal propagation could be detected in up to three adjacent cells on either side of a target cell (Maeda et al., 2012). However, given the highly variable cell distribution and orientation in the intervertebral disc, the highly variable end-point fluorescent intensities of all cells, and the relative rarity of such three-cell-propagation cases (12 of 111 image sets), these image sets were not examined further for intercellular signal-propagation trends as they would require a much more complicated analysis with poor statistical power.

Essentially, these data suggest that in the outer bovine annulus fibrosus, gap-junctional intercellular communication does not tend to exhibit any clearly non-homogeneous behavior. If outer annulus cells are in close enough proximity with each other to form gap junctions, they likely do form gap junctions and have the ability to communicate through them to each other. A given target cell appeared to communicate with all of its one-to-five nearest interconnected neighbors in 76% of cases, versus 24% of cases where it only appeared to communicate with a fraction of its nearest interconnected neighbors, irrespective of orientation or morphology. This suggests that groups of clustered cells are likely to communicate with each other in all three Cartesian directions (or circumferential, axial, and radial directions *in situ*), with no clearly identifiable directional preferences or biases. Signal propagation rarely appeared to go beyond two interconnected cells. Although it was initially hypothesized that intercellular signal propagation would perhaps be constricted to cells within a given linear array (in the case of spindle-shaped lamellar cells) or layer, these results suggest that intercellular signaling does not demonstrate any such restrictive patterns.

For tissue-engineered disk repair or replacement strategies, these findings suggest that intercellular communication can likely be considered isotropic, which could perhaps be a simplified design criterion for structural scaffolds impregnated with intervertebral disc cells

compared to specifically designing scaffolds to accommodate intercellular signaling irregularities.

3.4.5 Time effects.

In the current study, samples were loaded in static tension for 30 to 193 min. Average end-point fluorescent intensities of nearest-neighbor cells to photobleached target cells are shown in Figure 3.25, where a decrease in gap junction permeability would appear as a higher average end-point fluorescent intensity. Samples were separated by tension level since tension is known to affect gap-junction permeability (as discussed in §3.4.3), though no clear effect on gap-junction permeability was observed at high levels of tension with the methodology used in this study.

Gap junction turnover is fairly rapid, with connexins demonstrating half-lives of no longer than a few hours (M. U. Hussain, 2014a). On the time scale of minutes to hours, gene expression can thus affect gap junction communication: in rat tendon, a 1 N static tensile load had no effect on gap-junction permeability after 10 min, yet permeability dropped significantly after 1 hour of loading, corresponding to a suppression of connexin-43 protein expression due to the increased turnover of gap junctions (Maeda et al., 2012). Connexin-43 mRNA levels, however, were upregulated, suggesting that tenocytes were attempting to restore their functional gap junctions in response to them being mechanically disrupted and degraded at a faster rate.

In the intervertebral disc, it would therefore be expected that increasing time spent in static tension would correspond to a reduction in gap-junction permeability. Unfortunately, the effect of time on gap-junction permeability was unclear with the current data set. Separated by strain level, only one to four strips were held under static strain, providing few data points at different time intervals that could be used in statistical comparison. Furthermore, the removal of circumferential strips of disc tissue from their intact *in situ* environment may have drastically

altered the loading environment such that even at high strain levels (20 or 25%), cells were still relatively unloaded, as discussed previously (§3.4.3). If this is the case, any time effects on gap junction permeability would therefore be less pronounced than in the native loading environment and therefore even harder to detect.

The experiments performed in the current study were not originally intended to study time effects; however, the time-in-tension data was available and examined in case it pointed toward any interesting findings. While these results were inconclusive, the experimental protocol could be adapted and used with a larger sample size to better study the effects of temporally varied mechanical load and its effect on gap-junctional intercellular communication in the intervertebral disc.

Chapter Four: Conclusions

4.1 Introduction

This study investigated intercellular signal propagation in live bovine annulus fibrosus tissue. Given the unique, anisotropic structure of the intervertebral disc, it was hypothesized that intercellular signaling would exhibit similarly non-homogeneous behavior; however, the experiments performed in this study suggest that intercellular communication is predominantly proximity based. A given target cell appeared to communicate with all of its one-to-five nearest interconnected neighbors in 76% of cases, versus 24% of cases where it only appeared to communicate with a fraction of its nearest interconnected neighbors. This suggests that groups of clustered cells are likely to communicate with each other in all three Cartesian directions (or circumferential, axial, and radial directions *in situ*), with no clearly identifiable directional preferences or biases, though signal propagation rarely appeared to go beyond two interconnected cells.

This study also examined gap junction permeability at different strain levels. Previously, high flexion loads in the intact intervertebral disc had been found to disrupt gap junction intercellular signaling. This study found a slight increase in gap junction permeability at moderate loads (15% strain in linear tension) but no clear disruption even at extremely high loads, perhaps due to the methodology in this study that bluntly dissected discs from their adjoining vertebrae.

Lastly, this study attempted to perform specific target-cell photobleaching within a three-dimensional imaging volume using two-photon-excitation fluorescence microscopy, yet it was determined that two-photon excitation, while effective at minimizing overall image photobleaching, meant that specific-target-cell photobleaching was not feasible. The target cell

could be not sufficiently photobleached within a reasonable timeframe to observe any fluorescent molecule movement.

This knowledge may be beneficial in understanding the normal function of healthy disc tissue, thus providing a benchmark to compare diseased tissue with and may have implications for tissue-engineered regenerative or repair strategies of the intervertebral disc, where gap-junction intercellular communication may need to be addressed as a design requirement.

4.2 Limitations

The major limitation of this study was the use of excised annulus fibrosus strips instead of intact discs. Circumferential disc strips were removed from their native *in situ* microenvironment and unfolded into strips that were loaded in tension. This modified the loading environment of the annulus (where collagen fibers would normally have been firmly anchored into vertebral endplates) but nevertheless allowed for accurate strain measurements as well as the investigation of radial-direction intercellular signaling by rotating samples 90° along their longitudinal axis (per Figure 3.3B). Tissue swelling may also have affected the cellular microenvironment as samples were immersed in PBS for up to five hours, which could have induced tissue swelling and further modification of the cellular microenvironment.

Studies were performed at room temperature, which is below the physiological value of 37°C. Gap junction activity had previously been reported at room temperature (Chi et al., 2004, 2005; Desrochers & Duncan, 2012; Guilak et al., 1994), and as diffusion scales linearly with temperature (Houtsmauller, 2005), it would be expected that calcein mobility would be enhanced at higher temperatures. Increased calcein mobility would likely appear as larger fluorescent intensity drops in neighboring cells to the target cell due to higher diffusion rates and would also perhaps increase intensity drops along chains of three or more interconnected cells. This would

likely help better understand the length of downstream signal propagation between interconnected chains of cells.

Particularly in the case of perpendicular FLIP image sets, small N (17) may limit the authority of any conclusions with respect to radial-direction intercellular signaling. Lamellar–interlamellar interfaces were often poorly defined. Well-defined lamellar–interlamellar transitions as in Figure 3.10 were rare to find when the imaging plane was parallel to the annulus lamellae (per Figure 3.3A), and even harder to find when imaging perpendicular to the annulus lamellae (per Figure 3.3B). More conclusive findings regarding intercellular communication at lamellar–interlamellar interfaces would require deliberate identification of such regions within outer annulus tissue and gathering enough data for statistical comparison. As disc cells are relatively sparse, occupying only 1% of the disc by volume (Susan R.S. Bibby et al., 2001), lamellar–interlamellar regions are a subset of this population, which adds the practical constraint of spending time searching for such regions during experimentation.

The FLIP imaging protocol used in this study resulted in a heavily photobleached target cell that rarely regained any fluorescent intensity after the six-minute imaging period and was therefore unable to be imaged more than once. Thus, it cannot be definitively claimed that AGA disrupts gap-junction functioning within a single cell, though overall trends indirectly point toward AGA attenuating gap-junction functioning (see §3.4.2). Furthermore, the reversibility of pharmacological gap-junction inhibitor AGA was not investigated in this study. While AGA may be partially reversible (Rozental et al., 2001), experiments examining the restoration of gap-junction functioning after AGA removal were not performed.

The six-minute experiment run-time used in this study was selected to investigate diffusion-based intercellular communication on this time-scale (see §3.2.4). Additionally, samples were held in static tension for up to 193 min to investigate the longer-term effects of

tension on gap-junction permeability (see §3.4.5). Mechanotransducive and intercellular communication events may occur on both shorter and longer time scales. Immediate application of mechanical stimulus to a cell can cause a cellular response within milliseconds, while other signaling pathways act over hours or days by altering gene expression (Lotz & Hsieh, 2014). The methods used in this study only permitted investigation of intercellular communication on the minutes-to-hours time-scale.

The use of calcein AM as a fluorescent label enabled the investigation of diffusion through gap junctions formed by connexin 43 (see §3.4.2); however, other connexin isoforms such as connexin 45 have been found in the disc (Gruber et al., 2001). This study was limited to the movement of calcein through connexin-43 gap junctions and cannot make any inferences as to intercellular communication through connexin-45 gap junctions, which have too small of a pore size to allow the passage of calcein molecules. Furthermore, specific ions and other metabolites diffuse through gap junctions, which cannot be directly visualized via calcein staining. The selection of different fluorescent labels could help elucidate the exact chemical composition of intercellular-messaging molecules.

4.3 Future Work

Further studies are required to more deeply understand gap-junctional intercellular signaling in the intervertebral disc and how these signals can be propagated between chains of connected cells. These include:

- Performing similar FLIP experiments in the intact intervertebral disc instead of a bluntly dissected circumferential strip of disc tissue to have a more physiological representation of the cellular microenvironment (and at temperatures closer to the physiological value of 37°C)

- Performing similar FLIP experiments with the imaging plane perpendicular to the annulus lamellae (per Figure 3.3B) at strain levels higher than 1%
- Comparing intercellular communication between healthy and diseased tissue states
- Using human intervertebral disc tissue to validate findings from bovine and other animal model studies
- More specifically examining the chemical composition of messages being sent from one cell to another with the use of different fluorescent labels such as ion-specific labels or a nitric-oxide-specific label
- Discerning the exact location of functional connexin-43 gap junctions between interconnected cells (connexin-43 hemichannels are known to be distributed extensively across cell membranes and processes; however, which ones of these form functional gap junctions is not yet known)

Chapter Five: References

- Adachi, T., Aonuma, Y., Ito, S., Tanaka, M., Hojo, M., Takano-Yamamoto, T., & Kamioka, H. (2009). Osteocyte calcium signaling response to bone matrix deformation. *Journal of Biomechanics*, 42(15), 2507–2512. <http://doi.org/10.1016/j.jbiomech.2009.07.006>
- Adachi, T., Aonuma, Y., Taira, K., Hojo, M., & Kamioka, H. (2009). Asymmetric intercellular communication between bone cells: Propagation of the calcium signaling. *Biochemical and Biophysical Research Communications*, 389(3), 495–500. <http://doi.org/10.1016/j.bbrc.2009.09.010>
- Adams, M. A., & Hutton, W. C. (1980). The effect of posture on the role of the apophysial joints in resisting intervertebral compressive forces. *The Journal of Bone and Joint Surgery. British Volume*, 62-B(3), 358–362. <http://doi.org/10.1302/0301-620X.62B3.6447702>
- Adams, M. A., & Roughley, P. J. (2006). What is intervertebral disc degeneration, and what causes it? *Spine*, 31(18), 2151–2161. <http://doi.org/10.1097/01.brs.0000231761.73859.2c>
- Adler, J., & Pagakis, S. N. (2003). Reducing image distortions due to temperature-related microscope stage drift. *Journal of Microscopy*, 210(2), 131–137. <http://doi.org/10.1046/j.1365-2818.2003.01160.x>
- Allegri, M., Montella, S., Salici, F., Valente, A., Marchesini, M., Compagnone, C., ... Fanelli, G. (2016). Mechanisms of low back pain: A guide for diagnosis and therapy. *F1000Research*, 5, 1530. <http://doi.org/10.12688/f1000research.8105.2>
- Ambard, D., & Cherblanc, F. (2009). Mechanical behavior of annulus fibrosus: A microstructural model of fibers reorientation. *Annals of Biomedical Engineering*, 37(11), 2256–2265. <http://doi.org/10.1007/s10439-009-9761-7>
- Banes, A. J., Weinhold, P., Yang, X., Tsuzaki, M., Bynum, D., Bottlang, M., & Brown, T. (1999). Gap junctions regulate responses of tendon cells ex vivo to mechanical loading. *Clinical Orthopaedics and Related Research*, 367(Supplement S), S356–S370. <http://doi.org/10.1097/00003086-199910001-00034>
- Bao, L., Sachs, F., & Dahl, G. (2004). Connexins are mechanosensitive. *American Journal of Physiology: Cell Physiology*, 287(5), C1389–C1395. <http://doi.org/10.1152/ajpcell.00220.2004>
- Bathany, C., Beahm, D., Felske, J. D., Sachs, F., & Hua, S. Z. (2011). High throughput assay of diffusion through Cx43 gap junction channels with a microfluidic chip. *Analytical Chemistry*, 83(3), 933–939. <http://doi.org/10.1021/ac102658h>
- Battié, M. C. (2006). Lumbar disc degeneration: Epidemiology and genetics. *The Journal of Bone and Joint Surgery. American Volume*, 88-A(Supplement 2), 3. <http://doi.org/10.2106/JBJS.E.01313>

- Bennett, M. V., & Verselis, V. K. (1992). Biophysics of gap junctions. *Seminars in Cell Biology*, 3(1), 29–47. [http://doi.org/10.1016/S1043-4682\(10\)80006-6](http://doi.org/10.1016/S1043-4682(10)80006-6)
- Bergknut, N., Rutges, J. P. H. J., Kranenburg, H. J. C., Smolders, L. A., Hagman, R., Smidt, H. J., ... Dhert, W. J. A. (2012). The dog as an animal model for intervertebral disc degeneration. *Spine*, 37(5), 351–358. <http://doi.org/10.1097/BRS.0b013e31821e5665>
- Berridge, M. J., Bootman, M. D., & Roderick, H. L. (2003). Calcium signalling: Dynamics, homeostasis and remodelling. *Nature Reviews Molecular Cell Biology*, 4(7), 517–529. <http://doi.org/10.1038/nrm1155>
- Bibby, S. R. S., Jones, D. A., Lee, R. B., Yu, J., & Urban, J. P. G. (2001). The pathophysiology of the intervertebral disc. *Joint Bone Spine*, 68(6), 537–542. [http://doi.org/10.1016/S1297-319X\(01\)00332-3](http://doi.org/10.1016/S1297-319X(01)00332-3)
- Bibby, S. R. S., & Urban, J. P. G. (2004). Effect of nutrient deprivation on the viability of intervertebral disc cells. *European Spine Journal*, 13(8), 695–701. <http://doi.org/10.1007/s00586-003-0616-x>
- Blonk, J. C. G., Don, A., Van Aaslt, H., & Birmingham, J. J. (1993). Fluorescence photobleaching recovery in the confocal scanning light microscope. *Journal of Microscopy*, 169(3), 363–374. <http://doi.org/10.1111/j.1365-2818.1993.tb03312.x>
- Bray, R. C., Salo, P. T., Lo, I. K., Ackermann, P., Rattner, J. B., & Hart, D. A. (2005). Normal ligament structure, physiology and function. *Sports Medicine And Arthroscopy Review*, 13(3), 127–135.
- Bron, J. L., Helder, M. N., Meisel, H. J., Van Royen, B. J., & Smit, T. H. (2009). Repair, regenerative and supportive therapies of the annulus fibrosus: Achievements and challenges. *European Spine Journal*, 18(3), 301–313. <http://doi.org/10.1007/s00586-008-0856-x>
- Bruehlmann, S. B., Rattner, J. B., Matyas, J. R., & Duncan, N. A. (2002). Regional variations in the cellular matrix of the annulus fibrosus of the intervertebral disc. *Journal of Anatomy*, 201(2), 159–71. <http://doi.org/10.1046/j.1469-7580.2002.00080.x>
- Bruzzone, R., White, T. W., & Paul, D. L. (1996). Connections with connexins: The molecular basis of direct intercellular signaling. *European Journal of Biochemistry*, 238(1), 1–27. <http://doi.org/10.1111/j.1432-1033.1996.0001q.x>
- Bush, P. G., Wokosin, D. L., & Hall, A. C. (2007). Two-versus one photon excitation laser scanning microscopy: Critical importance of excitation wavelength. *Frontiers in Bioscience: A Journal and Virtual Library*, 12, 2646–2657. <http://doi.org/10.2741/2261>
- Butcher, D. T., Alliston, T., & Weaver, V. M. (2009). A tense situation: Forcing tumour progression. *Nature Reviews Cancer*, 9(2), 108–122. <http://doi.org/10.1038/nrc2544>

- Chen, C., Tambe, D. T., Deng, L., & Yang, L. (2013). Biomechanical properties and mechanobiology of the articular chondrocyte. *American Journal of Physiology: Cell Physiology*, 305(12), C1202–C1208. <http://doi.org/10.1152/ajpcell.00242.2013>
- Chen, J., Yan, W., & Setton, L. A. (2004). Static compression induces zonal-specific changes in gene expression for extracellular matrix and cytoskeletal proteins in intervertebral disc cells in vitro. *Matrix Biology*, 22(7), 573–583. <http://doi.org/10.1016/j.matbio.2003.11.008>
- Cheung, K. M. C., Karppinen, J., Chan, D., Ho, D. W. H., Song, Y. Q., Sham, P., ... Luk, K. D. K. (2009). Prevalence and pattern of lumbar magnetic resonance imaging changes in a population study of one thousand forty-three individuals. *Spine*, 34(9), 934–940. <http://doi.org/10.1097/BRS.0b013e3181a01b3f>
- Chi, S. S., Rattner, J. B., & Matyas, J. R. (2004). Communication between paired chondrocytes in the superficial zone of articular cartilage. *Journal of Anatomy*, 205(5), 363–370. <http://doi.org/10.1111/j.0021-8782.2004.00350.x>
- Chi, S. S., Rattner, J. B., Sciore, P., Boorman, R., & Lo, I. K. Y. (2005). Gap junctions of the medial collateral ligament: Structure, distribution, associations and function. *Journal of Anatomy*, 207(2), 145–154. <http://doi.org/10.1111/j.1469-7580.2005.00440.x>
- Choy, A. T. H., & Chan, B. P. (2015). A structurally and functionally biomimetic biphasic scaffold for intervertebral disc tissue engineering. *PLoS ONE*, 10(6), 1–18. <http://doi.org/10.1371/journal.pone.0131827>
- Christ, B., & Wilting, J. (1992). From somites to vertebral column. *Annals of Anatomy*, 174(1), 23–32. [http://doi.org/10.1016/S0940-9602\(11\)80337-7](http://doi.org/10.1016/S0940-9602(11)80337-7)
- Chung, S. A., Khan, S. N., & Diwan, A. D. (2003). The molecular basis of intervertebral disk degeneration. *Orthopedic Clinics of North America*, 34(2), 209–219. [http://doi.org/10.1016/S0030-5898\(03\)00026-9](http://doi.org/10.1016/S0030-5898(03)00026-9)
- Colombier, P., Clouet, J., Hamel, O., Lescaudron, L., & Guicheux, J. (2014). The lumbar intervertebral disc: From embryonic development to degeneration. *Joint Bone Spine*, 81(2), 125–129. <http://doi.org/10.1016/j.jbspin.2013.07.012>
- Cortes, D. H., & Elliott, D. M. (2014). The intervertebral disc: Overview of disc mechanics. In I. M. Shapiro & M. V. Risbud (Eds.), *The Intervertebral Disc: Molecular and Structural Studies of the Disc in Health and Disease* (pp. 17–31). Vienna: Springer-Verlag. http://doi.org/10.1007/978-3-7091-1535-0_2
- Coventry, M. B. (1969). Anatomy of the intervertebral disk. *Clinical Orthopaedics and Related Research*, 67, 9–15.
- Cramer, G. D. (2014). General characteristics of the spine. In G. D. Cramer & S. A. Darby (Eds.), *Clinical Anatomy of the Spine, Spinal Cord, and ANS* (Third Edit, pp. 15–64). St. Louis, Mo.: Elsevier. <http://doi.org/10.1016/B978-0-323-07954-9.00002-5>

- Dagenais, S., Caro, J., & Haldeman, S. (2008). A systematic review of low back pain cost of illness studies in the United States and internationally. *Spine Journal*, 8(1), 8–20. <http://doi.org/10.1016/j.spinee.2007.10.005>
- Daly, C., Ghosh, P., Jenkin, G., Oehme, D., & Goldschlager, T. (2016). A review of animal models of intervertebral disc degeneration: Pathophysiology, regeneration, and translation to the clinic. *BioMed Research International*, Vol. 2016, 1–14. <http://doi.org/10.1155/2016/5952165>
- Davidson, J. S., Baumgarten, I. M., & Harley, E. H. (1986). Reversible inhibition of intercellular junctional communication by glycyrrhetic acid. *Biochemical and Biophysical Research Communications*, 134(1), 29–36.
- De Schepper, E. I. T., Damen, J., Van Meurs, J. B. J., Ginai, A. Z., Popham, M., Hofman, A., ... Bierma-Zeinstra, S. M. (2010). The association between lumbar disc degeneration and low back pain: The influence of age, gender, and individual radiographic features. *Spine*, 35(5), 531–536. <http://doi.org/10.1097/BRS.0b013e3181aa5b33>
- Demers, C. N., Antoniou, J., & Mwale, F. (2004). Value and limitations of using the bovine tail as a model for the human lumbar spine. *Spine*, 29(24), 2793–2799. <http://doi.org/10.1097/01.brs.0000147744.74215.b0>
- DePaola, N., Davies, P. F., Pritchard, W. F., Florez, L., Harbeck, N., & Polacek, D. C. (1999). Spatial and temporal regulation of gap junction connexin43 in vascular endothelial cells exposed to controlled disturbed flows in vitro. *Proceedings of the National Academy of Sciences*, 96(6), 3154–3159. <http://doi.org/10.1073/pnas.96.6.3154>
- Desrochers, J., & Duncan, N. A. (2010). Strain transfer in the annulus fibrosus under applied flexion. *Journal of Biomechanics*, 43(11), 2141–2148. <http://doi.org/10.1016/j.jbiomech.2010.03.045>
- Desrochers, J., & Duncan, N. A. (2012). Intercellular communication via gap junctions affected by mechanical load in the bovine annulus fibrosus. *Computer Methods in Biomechanics and Biomedical Engineering*, (July 2015), 1–8. <http://doi.org/10.1080/10255842.2012.717268>
- Diaspro, A., Chirico, G., Usai, C., Ramoino, P., & Dobrucki, J. (2006). Photobleaching. In J. B. Pawley (Ed.), *Handbook of Biological Confocal Microscopy* (Third Edit, pp. 690–702). Springer, New York, NY. http://doi.org/10.1007/978-0-387-45524-2_39
- Du, L., Zhu, M., Yang, Q., Zhang, J., Ma, X., Kong, D., ... Wang, L. (2014). A novel integrated biphasic silk fibroin scaffold for intervertebral disc tissue engineering. *Materials Letters*, 117, 237–240. <http://doi.org/10.1016/j.matlet.2013.12.029>
- Duclos, S. E., & Michalek, A. J. (2017). Residual strains in the intervertebral disc annulus fibrosus suggest complex tissue remodeling in response to in-vivo loading. *Journal of the Mechanical Behavior of Biomedical Materials*, 68(2017), 232–238. <http://doi.org/10.1016/j.jmbbm.2017.02.010>

- Duncan, N. A. (2006). Cell deformation and micromechanical environment in the intervertebral disc. *The Journal of Bone and Joint Surgery. American Volume*, 88–A(Supplement 2), 47–51. <http://doi.org/10.2106/JBJS.F.00035>
- Elfervig, M. K., Minchew, J. T., Francke, E., Tsuzaki, M., & Banes, A. J. (2001). IL-1beta sensitizes intervertebral disc annulus cells to fluid-induced shear stress. *Journal of Cellular Biochemistry*, 82(2), 290–298. <http://doi.org/10.1002/jcb.1153>
- Evans, W. H., & Martin, P. E. M. (2002). Gap junctions: Structure and function (review). *Molecular Membrane Biology*, 19(2), 121–136. <http://doi.org/10.1080/09687680210139839>
- Eyre, D. R., & Muir, H. (1976). Types I and II collagens in intervertebral disc. Interchanging radial distributions in annulus fibrosus. *The Biochemical Journal*, 157, 267–270. <http://doi.org/10.1042/bj1570267>
- Frymoyer, J. W. (1988). Back pain and sciatica. *New England Journal of Medicine*, 318(5), 291–300. <http://doi.org/10.1056/NEJM198802043180506>
- Furtwängler, T., Chan, S. C. W., Bahrenberg, G., Richards, P. J., & Gantenbein-Ritter, B. (2013). Assessment of the matrix degenerative effects of MMP-3, ADAMTS-4, and HTRA1, injected into a bovine intervertebral disc organ culture model. *Spine*, 38(22), 1377–1387. <http://doi.org/10.1097/BRS.0b013e31829ffde8>
- Ghannam, M., Jumah, F., Mansour, S., Samara, A., Alkhodour, S., Alzuabi, M. A., ... Shane Tubbs, R. (2017). Surgical anatomy, radiological features, and molecular biology of the lumbar intervertebral discs. *Clinical Anatomy*, 30(2), 251–266. <http://doi.org/10.1002/ca.22822>
- Goldberg, G. S., Moreno, A. P., Bechberger, J. F., Hearn, S. S., Shivers, R. R., Macphee, D. J., ... Naus, C. C. G. (1996). Evidence that disruption of connexon particle arrangements in gap junction plaques is associated with inhibition of gap junctional communication by a glycyrrhetic acid derivative. *Experimental Cell Research*, 222(1), 48–53. <http://doi.org/10.1006/excr.1996.0006>
- González Martínez, E., García-Cosamalón, J., Cosamalón-Gan, I., Esteban Blanco, M., García-Suarez, O., & Vega, J. A. (2017). Biology and mechanobiology of the intervertebral disc. *Neurocirugia*, 28(3), 135–140. <http://doi.org/10.1016/j.neucir.2016.12.002>
- Goodenough, D. A., Goliger, J. A., & Paul, D. L. (1996). Connexins, connexons, and intercellular communication. *Annual Review of Biochemistry*, 65, 475–502. <http://doi.org/10.1146/annurev.bi.65.070196.002355>
- Goodenough, D. A., & Paul, D. L. (2003). Beyond the gap: Functions of unpaired connexon channels. *Nature Reviews Molecular Cell Biology*, 4(4), 285–294. <http://doi.org/10.1038/nrm1072>
- Goodenough, D. A., & Paul, D. L. (2009). Gap junctions. *Cold Spring Harbor Perspectives in Biology*, 1, a002576. <http://doi.org/10.1101/cshperspect.a002576>

- Gruber, H. E., Ma, D., Hanley, E. N., Ingram, J., & Yamaguchi, D. T. (2001). Morphologic and molecular evidence for gap junctions and connexin 43 and 45 expression in annulus fibrosus cells from the human intervertebral disc. *Journal of Orthopaedic Research: Official Publication of the Orthopaedic Research Society*, 19(5), 985–9. [http://doi.org/10.1016/S0736-0266\(00\)00072-3](http://doi.org/10.1016/S0736-0266(00)00072-3)
- Grunhagen, T., Wilde, G., Soukane, D. M., Shirazi-Adl, S. a, & Urban, J. P. G. (2006). Nutrient supply and intervertebral disc metabolism. *The Journal of Bone and Joint Surgery. American Volume*, 88-A(Supplement 2), 30–35. <http://doi.org/10.2106/JBJS.E.01290>
- Guilak, F., Donahue, H., Zell, R., Grande, D., McLeod, K., & Rubin, C. (1994). Deformation-induced calcium signaling in articular chondrocytes. In V. C. Mow, R. Tran-Son-Tay, F. Guilak, & R. M. Hochmuth (Eds.), *Cell Mechanics and Cellular Engineering* (pp. 380–397). Springer, New York, NY.
- Han, S.-K., Wouters, W., Clark, A., & Herzog, W. (2012). Mechanically induced calcium signaling in chondrocytes in situ. *Journal of Orthopaedic Research: Official Publication of the Orthopaedic Research Society*, 30(3), 475–81. <http://doi.org/10.1002/jor.21536>
- Han, W. M., Heo, S. J., Driscoll, T. P., Boggs, M. E., Duncan, R. L., Mauck, R. L., & Elliott, D. M. (2014). Impact of cellular microenvironment and mechanical perturbation on calcium signalling in meniscus fibrochondrocytes. *European Cells and Materials*, 27, 321–331.
- Hastreiter, D., Ozuna, R. M., & Spector, M. (2001). Regional variations in certain cellular characteristics in human lumbar intervertebral discs, including the presence of α-smooth muscle actin. *Journal of Orthopaedic Research*, 19(4), 597–604. [http://doi.org/10.1016/S0736-0266\(00\)00069-3](http://doi.org/10.1016/S0736-0266(00)00069-3)
- Hayes, A. J., Benjamin, M., & Ralphs, J. R. (1999). Role of actin stress fibres in the development of the intervertebral disc: Cytoskeletal control of extracellular matrix assembly. *Developmental Dynamics*, 215(3), 179–189. [http://doi.org/10.1002/\(SICI\)1097-0177\(199907\)215:3<179::AID-AJA1>3.0.CO;2-Q](http://doi.org/10.1002/(SICI)1097-0177(199907)215:3<179::AID-AJA1>3.0.CO;2-Q)
- Helmchen, F., & Denk, W. (2005). Deep tissue two-photon microscopy. *Nature Methods*, 2(12), 932–940. <http://doi.org/10.1038/nmeth818>
- Houtsmuller, A. B. (2005). Fluorescence recovery after photobleaching: Application to nuclear proteins. *Advances in Biochemical Engineering/Biotechnology*, 95, 177–199. <http://doi.org/10.1007/b102214>
- Hsieh, A. H., & Twomey, J. D. (2010). Cellular mechanobiology of the intervertebral disc: New directions and approaches. *Journal of Biomechanics*, 43(1), 137–145. <http://doi.org/10.1016/j.jbiomech.2009.09.019>
- Hunter, C. J., Matyas, J. R., & Duncan, N. A. (2003). The notochordal cell in the nucleus pulposus: A review in the context of tissue engineering. *Tissue Engineering*, 9(4), 667–677. <http://doi.org/10.1089/107632703768247368>

- Hunter, C. J., Matyas, J. R., & Duncan, N. A. (2004). The functional significance of cell clusters in the notochordal nucleus pulposus: Survival and signaling in the canine intervertebral disc. *Spine*, 29(10), 1099–1104.
- Hussain, M. U. (2014a). General cell biology of connexins. In D. M. U. Hussain (Ed.), *Connexins: The Gap Junction Proteins* (pp. 7–9). New Delhi: Springer India. http://doi.org/10.1007/978-81-322-1919-4_4
- Hussain, M. U. (2014b). Molecular components and nomenclature of gap junctions. In D. M. U. Hussain (Ed.), *Connexins: The Gap Junction Proteins* (pp. 5–6). New Delhi: Springer India. http://doi.org/10.1007/978-81-322-1919-4_3
- Hussain, M. U. (2014c). Tissue distribution of connexins. In D. M. U. Hussain (Ed.), *Connexins: The Gap Junction Proteins* (pp. 39–56). New Delhi: Springer India. http://doi.org/10.1007/978-81-322-1919-4_10
- Inoue, H. (1981). Three-dimensional architecture of lumbar intervertebral discs. *Spine*, 6(2), 139–146. <http://doi.org/10.1097/00007632-198103000-00006>
- Ishihara, Y., Sugawara, Y., Kamioka, H., Kawanabe, N., Kurosaka, H., Naruse, K., & Yamashiro, T. (2012). In situ imaging of the autonomous intracellular Ca²⁺ oscillations of osteoblasts and osteocytes in bone. *Bone*, 50(4), 842–852. <http://doi.org/10.1016/j.bone.2012.01.021>
- Ishikawa-Ankerhold, H. C., Ankerhold, R., & Drummen, G. P. C. (2012). Advanced fluorescence microscopy techniques-FRAP, FLIP, FLAP, FRET and FLIM. *Molecules*, 17(4), 4047–4132. <http://doi.org/10.3390/molecules17044047>
- Jaalouk, D. E., & Lammerding, J. (2009). Mechanotransduction gone awry. *Nature Reviews Molecular Cell Biology*, 10(1), 63–73. <http://doi.org/10.1038/nrm2597>
- Jacobs, C. R., Temiyasathit, S., & Castillo, A. B. (2010). Osteocyte mechanobiology and pericellular mechanics. *Annual Review of Biomedical Engineering*, 12(1), 369–400. <http://doi.org/10.1146/annurev-bioeng-070909-105302>
- Jeong, J. H., Lee, J. H., Jin, E. S., Min, J. K., Jeon, S. R., & Choi, K. H. (2010). Regeneration of intervertebral discs in a rat disc degeneration model by implanted adipose-tissue-derived stromal cells. *Acta Neurochirurgica*, 152(10), 1771–1777. <http://doi.org/10.1007/s00701-010-0698-2>
- Kanaporis, G., Brink, P. R., & Valiunas, V. (2011). Gap junction permeability: Selectivity for anionic and cationic probes. *American Journal of Physiology. Cell Physiology*, 300(3), C600–9. <http://doi.org/10.1152/ajpcell.00316.2010>
- Kandel, R., Santerre, P., Massicotte, E., & Hurtig, M. (2014). Tissue engineering of the intervertebral disc. In I. M. Shapiro & M. V. Risbud (Eds.), *The Intervertebral Disc: Molecular and Structural Studies of the Disc in Health and Disease* (pp. 417–433). Vienna: Springer-Verlag. http://doi.org/10.1007/978-3-7091-1535-0_26

- Keller, H. E. (2006). Objective lenses for confocal microscopy. In J. B. Pawley (Ed.), *Handbook of Biological Confocal Microscopy* (Third Edit, pp. 145–161). Springer, New York, NY. http://doi.org/10.1007/978-0-387-45524-2_7
- Kelsey, J. L., White, A. A., & Sci, M. (1980). Epidemiology and impact of low-back pain. *Spine*, 5(2), 133–142. <http://doi.org/10.1097/00007632-198003000-00007>
- Kjær, M. (2004). Role of extracellular matrix in adaptation of tendon and skeletal muscle to mechanical loading. *Physiological Reviews*, 84(2), 649–698. <http://doi.org/10.1152/physrev.00031.2003>
- Kjær, M., Langberg, H., Heinemeier, K., Bayer, M. L., Hansen, M., Holm, L., ... Magnusson, S. P. (2009). From mechanical loading to collagen synthesis, structural changes and function in human tendon. *Scandinavian Journal of Medicine and Science in Sports*, 19(4), 500–510. <http://doi.org/10.1111/j.1600-0838.2009.00986.x>
- Kjær, M., Magnusson, P., Krosgaard, M., Møller, J. B., Olesen, J., Heinemeier, K., ... Langberg, H. (2006). Extracellular matrix adaptation of tendon and skeletal muscle to exercise. *Journal of Anatomy*, 208(4), 445–450. <http://doi.org/10.1111/j.1469-7580.2006.00549.x>
- Kumar, N. M., & Gilula, N. B. (1996). The gap junction communication channel. *Cell*, 84(3), 381–388.
- Laird, D. W. (2006). Life cycle of connexins in health and disease. *Biochemical Journal*, 394(3), 527–543. <http://doi.org/10.1042/BJ20051922>
- Lauerman, W. C., Platenberg, R. C., Cain, J. E., & Deeney, V. F. (1992). Age-related disk degeneration: Preliminary report of a naturally occurring baboon model. *Journal of Spinal Disorders*, 5(2), 170–174. <http://doi.org/10.1097/00002517-199206000-00004>
- Li, G., Wang, S., Passias, P., Xia, Q., Li, G., & Wood, K. (2009). Segmental in vivo vertebral motion during functional human lumbar spine activities. *European Spine Journal*, 18(7), 1013–1021. <http://doi.org/10.1007/s00586-009-0936-6>
- Lotz, J. C., & Hsieh, A. H. (2014). The effects of mechanical forces on nucleus pulposus and annulus fibrosus cells. In I. M. Shapiro & M. V Risbud (Eds.), *The Intervertebral Disc: Molecular and Structural Studies of the Disc in Health and Disease* (pp. 109–124). Vienna: Springer-Verlag. http://doi.org/10.1007/978-3-7091-1535-0_7
- Lu, X. L., Huo, B., Park, M., & Guo, X. E. (2012). Calcium response in osteocytic networks under steady and oscillatory fluid flow. *Bone*, 51(3), 466–473. <http://doi.org/10.1016/j.bone.2012.05.021>
- Luoma, K., Riihimäki, H., Luukkonen, R., Raininko, R., Viikari-Juntura, E., & Lamminen, A. (2000). Low back pain in relation to lumbar disc degeneration. *Spine*, 25(4), 487–492. <http://doi.org/10.1097/00007632-200002150-00016>

- Maeda, E., & Ohashi, T. (2015). Mechano-regulation of gap junction communications between tendon cells is dependent on the magnitude of tensile strain. *Biochemical and Biophysical Research Communications*, 465(2), 281–286.
<http://doi.org/10.1016/j.bbrc.2015.08.021>
- Maeda, E., Pian, H., & Ohashi, T. (2017). Temporal regulation of gap junctional communication between tenocytes subjected to static tensile strain with physiological and non-physiological amplitudes. *Biochemical and Biophysical Research Communications*, 482(4), 1170–1175.
<http://doi.org/10.1016/j.bbrc.2016.12.007>
- Maeda, E., Shelton, J. C., Bader, D. L., & Lee, D. A. (2007). Time dependence of cyclic tensile strain on collagen production in tendon fascicles. *Biochemical and Biophysical Research Communications*, 362(2), 399–404. <http://doi.org/10.1016/j.bbrc.2007.08.029>
- Maeda, E., Ye, S., Wang, W., Bader, D. L., Knight, M. M., & Lee, D. A. (2012). Gap junction permeability between tenocytes within tendon fascicles is suppressed by tensile loading. *Biomechanics and Modeling in Mechanobiology*, 11(3–4), 439–447.
<http://doi.org/10.1007/s10237-011-0323-1>
- Masuda, K., Aota, Y., Muehleman, C., Imai, Y., Okuma, M., Thonar, E. J., ... An, H. S. (2005). A novel rabbit model of mild, reproducible disc degeneration by an annulus needle puncture: Correlation between the degree of disc injury and radiological and histological appearances of disc degeneration. *Spine*, 30(1), 5–14.
<http://doi.org/10.1097/01.brs.0000148152.04401.20>
- Mayan, M. D., Gago-Fuentes, R., Carpintero-Fernandez, P., Fernandez-Puente, P., Filgueira-Fernandez, P., Goyanes, N., ... Blanco, F. J. (2015). Articular chondrocyte network mediated by gap junctions: Role in metabolic cartilage homeostasis. *Annals of the Rheumatic Diseases*, 74(1), 275–284. <http://doi.org/10.1136/annrheumdis-2013-204244>
- McMillan, J. L. (2009). *Cell morphology and gap junction communication in the annulus fibrosus*. University of Calgary, Calgary, Alberta, Canada.
- McNeilly, C. M., Banes, A. J., Benjamin, M., & Ralphs, J. R. (1996). Tendon cells in vivo form a three dimensional network of cell processes linked by gap junctions. *J. Anat.*, 189, 593–600.
- Melrose, J., & Roughley, P. (2014). Proteoglycans of the intervertebral disc. In I. M. Shapiro & M. V. Risbud (Eds.), *The Intervertebral Disc: Molecular and Structural Studies of the Disc in Health and Disease* (pp. 53–77). Vienna: Springer-Verlag. http://doi.org/10.1007/978-3-7091-1535-0_4
- Moran, A. L. (2000). Calcein as a marker in experimental studies newly-hatched gastropods. *Marine Biology*, 137(5–6), 893–898. <http://doi.org/10.1007/s002270000390>

- Mwale, F. (2014). Collagen and other proteins of the nucleus pulposus, annulus fibrosus, and cartilage end plates. In I. M. Shapiro & M. V. Risbud (Eds.), *The Intervertebral Disc: Molecular and Structural Studies of the Disc in Health and Disease* (pp. 79–92). Vienna: Springer-Verlag. http://doi.org/10.1007/978-3-7091-1535-0_5
- Nachemson, A. (1966). The load on lumbar disks in different positions of the body. *Clinical Orthopaedics and Related Research*, 45, 107–122.
- Neidlinger-Wilke, C., Galbusera, F., Pratsinis, H., Mavrogenatou, E., Mietsch, A., Kletsas, D., & Wilke, H.-J. (2014). Mechanical loading of the intervertebral disc: From the macroscopic to the cellular level. *European Spine Journal*, 23(Supplement 3), S333–343. <http://doi.org/10.1007/s00586-013-2855-9>
- Nerurkar, N. L., Elliott, D. M., & Mauck, R. L. (2010). Mechanical design criteria for intervertebral disc tissue engineering. *Journal of Biomechanics*, 43(6), 1017–1030. <http://doi.org/10.1016/j.jbiomech.2009.12.001>
- Newell, N., Little, J. P., Christou, A., Adams, M. A., Adam, C. J., & Masouros, S. D. (2017). Biomechanics of the human intervertebral disc: A review of testing techniques and results. *Journal of the Mechanical Behavior of Biomedical Materials*, 69(C), 420–434. <http://doi.org/10.1016/j.jmbbm.2017.01.037>
- Oehme, D., Ghosh, P., Shimmon, S., Wu, J., McDonald, C., Troupis, J. M., ... Jenkin, G. (2014). Mesenchymal progenitor cells combined with pentosan polysulfate mediating disc regeneration at the time of microdiscectomy: A preliminary study in an ovine model. *Journal of Neurosurgery: Spine*, 20(6), 657–669. <http://doi.org/10.3171/2014.2.SPINE13760>
- Ohnishi, T., Sudo, H., Iwasaki, K., Tsujimoto, T., Ito, Y. M., & Iwasaki, N. (2016). In vivo mouse intervertebral disc degeneration model based on a new histological classification. *PLoS ONE*, 11(8), 1–12. <http://doi.org/10.1371/journal.pone.0160486>
- Olsen, A. S., Kang, J. D., Vo, N., & Sowa, G. (2018). The intervertebral disc: Normal, aging, and pathologic. In S. R. Garfin, F. J. Eismont, G. R. Bell, C. M. Bono, & J. S. Fischgrund (Eds.), *Rothman-Simeone and Herkowitz's The Spine* (7th ed., pp. 79–89). Philadelphia: Elsevier, Inc.
- Pappas, C. A., Rioult, M. G., & Ransom, B. R. (1996). Octanol, a gap junction uncoupling agent, changes intracellular [H⁺] in rat astrocytes. *Glia*, 16(1), 7–15. [http://doi.org/10.1002/\(SICI\)1098-1136\(199601\)16:1<7::AID-GLIA2>3.0.CO;2-2](http://doi.org/10.1002/(SICI)1098-1136(199601)16:1<7::AID-GLIA2>3.0.CO;2-2)
- Pazzaglia, U. E., Salisbury, J. R., & Byers, P. D. (1989). Development and involution of the notochord in the human spine. *Journal of the Royal Society of Medicine*, 82(7), 413–415.
- Pezowicz, C. A., Robertson, P. A., & Broom, N. D. (2006). The structural basis of interlamellar cohesion in the intervertebral disc wall. *Journal of Anatomy*, 208(3), 317–330. <http://doi.org/10.1111/j.1469-7580.2006.00536.x>

- Pingguan-Murphy, B., Lee, D. A., Bader, D. L., & Knight, M. M. (2005). Activation of chondrocytes calcium signalling by dynamic compression is independent of number of cycles. *Archives of Biochemistry and Biophysics*, 444(1), 45–51. <http://doi.org/10.1016/j.abb.2005.09.015>
- Platenberg, R., Hubbard, G. B., Ehler, W. J., & Hixson, C. J. (2001). Spontaneous disc degeneration in the baboon model: Magnetic resonance imaging and histopathologic correlation. *Journal of Medical Primatology*, 30(5), 268–272.
- Potter, S. M. (1996). Vital imaging: Two photons are better than one. *Current Biology*, 6(12), 1595–1598. [http://doi.org/10.1016/S0960-9822\(02\)70782-3](http://doi.org/10.1016/S0960-9822(02)70782-3)
- Rannou, F., Richette, P., Benallaoua, M., François, M., Genries, V., Korwin-Zmijowska, C., ... Poiraudeau, S. (2003). Cyclic tensile stretch modulates proteoglycan production by intervertebral disc annulus fibrosus cells through production of nitrite oxide. *Journal of Cellular Biochemistry*, 90(1), 148–157. <http://doi.org/10.1002/jcb.10608>
- Razaq, S., Wilkins, R. J., & Urban, J. P. G. (2003). The effect of extracellular pH on matrix turnover by cells of the bovine nucleus pulposus. *European Spine Journal*, 12(4), 341–349. <http://doi.org/10.1007/s00586-003-0582-3>
- Richardson, D. S., & Lichtman, J. W. (2015). Clarifying tissue clearing. *Cell*, 162(2), 246–257. <http://doi.org/10.1016/j.cell.2015.06.067>
- Richardson, S. M., Freemont, A. J., & Hoyland, J. A. (2014). Pathogenesis of Intervertebral Disc Degeneration. In I. M. Shapiro & M. V Risbud (Eds.), *The Intervertebral Disc: Molecular and Structural Studies of the Disc in Health and Disease* (pp. 177–200). Vienna: Springer-Verlag. http://doi.org/10.1007/978-3-7091-1535-0_11
- Risbud, M. V., Schaer, T. P., & Shapiro, I. M. (2010). Toward an understanding of the role of notochordal cells in the adult intervertebral disc: From discord to accord. *Developmental Dynamics*, 239(8), 2141–2148. <http://doi.org/10.1002/dvdy.22350>
- Risbud, M. V., & Shapiro, I. M. (2012). Notochordal cells in the adult intervertebral disc: New perspective on an old question. *Critical Reviews in Eukaryotic Gene Expression*, 21(1), 29–41. <http://doi.org/10.1615/CritRevEukarGeneExpr.v21.i1.30>
- Roberts, S., Evans, H., Trivedi, J., & Menage, J. (2006). Histology and pathology of the human intervertebral disc. *The Journal of Bone and Joint Surgery. American Volume*, 88–A(Supplement 2), 10–14. <http://doi.org/10.2106/JBJS.F.00019>
- Roberts, S., Menage, J., & Eisenstein, S. M. (1993). The cartilage end-plate and intervertebral disc in scoliosis: Calcification and other sequelae. *Journal of Orthopaedic Research*, 11(5), 747–57. <http://doi.org/10.1002/jor.1100110517>
- Roberts, S., Menage, J., Sivan, S., & Urban, J. P. G. (2008). Bovine explant model of degeneration of the intervertebral disc. *BMC Musculoskeletal Disorders*, 9(24), 1–6. <http://doi.org/10.1186/1471-2474-9-24>

- Roberts, S., Urban, J. P. G., Evans, H., & Eisenstein, S. M. (1996). Transport properties of the human cartilage endplate in relation to its composition and calcification. *Spine*, 21(4), 415–420. <http://doi.org/10.1097/00007632-199602150-00003>
- Rozental, R., Srinivas, M., & Spray, D. C. (2001). How to close a gap junction channel. In R. Bruzzone & C. Giaume (Eds.), *Methods in Molecular Biology, vol. 154: Connexin Methods and Protocols* (pp. 447–476). Totowa, NJ: Humana Press. <http://doi.org/10.1385/1-59259-043-8:447>
- Rubart, M. (2004). Two-photon microscopy of cells and tissue. *Circulation Research*, 95(12), 1154–1166. <http://doi.org/10.1161/01.RES.0000150593.30324.42>
- Ruiz, M. (2006). Gap cell junction [Online image]. Retrieved January 14, 2019, from https://commons.wikimedia.org/wiki/File:Gap_cell_junction-en.svg
- Sahlman, J., Inkinen, R., Hirvonen, T., Lammi, M. J., Lammi, P. E., Nieminen, J., ... Puustjärvi, K. (2001). Premature vertebral endplate ossification and mild disc degeneration in mice after inactivation of one allele belonging to the Col2a1 gene for type II collagen. *Spine*, 26(23), 2558–2565. <http://doi.org/10.1097/00007632-200112010-00008>
- Salameh, A., & Dhein, S. (2013). Effects of mechanical forces and stretch on intercellular gap junction coupling. *Biochimica et Biophysica Acta - Biomembranes*, 1828(1), 147–156. <http://doi.org/10.1016/j.bbamem.2011.12.030>
- Salari, B., & McAfee, P. C. (2012). Cervical total disk replacement: Complications and avoidance. *Orthopedic Clinics of North America*, 43(1), 97–107. <http://doi.org/10.1016/j.ocl.2011.08.006>
- Severs, N. J., Coppen, S. R., Dupont, E., Yeh, H.-I., Ko, Y.-S., & Matsushita, T. (2004). Gap junction alterations in human cardiac disease. *Cardiovascular Research*, 62(2), 368–377.
- Shivashankar, G. V., Sheetz, M., & Matsudaira, P. (2015). Mechanobiology. *Integrative Biology*, 7(10), 1091–1092. <http://doi.org/10.1039/C5IB90040A>
- Simon, A. M., & Goodenough, D. A. (1998). Diverse functions of vertebrate gap junctions. *Trends in Cell Biology*, 8(12), 477–482. [http://doi.org/10.1016/S0962-8924\(98\)01372-5](http://doi.org/10.1016/S0962-8924(98)01372-5)
- Sivan, S. S., Hayes, A. J., Wachtel, E., Caterson, B., Merkher, Y., Maroudas, A., ... Roberts, S. (2014). Biochemical composition and turnover of the extracellular matrix of the normal and degenerate intervertebral disc. *European Spine Journal*, 23(S3), 344–353. <http://doi.org/10.1007/s00586-013-2767-8>
- Sive, J. I., Baird, P., Jeziorsk, M., Watkins, A., Hoyland, J. A., & Freemont, A. J. (2002). Expression of chondrocyte markers by cells of normal and degenerate intervertebral discs. *Journal of Clinical Pathology - Molecular Pathology*, 55(2), 91–97. <http://doi.org/10.1136/mp.55.2.91>

- Sowa, G., Coelho, P., Vo, N., Bedison, R., Chiao, A., Davies, C., ... Kang, J. (2011). Determination of annulus fibrosus cell response to tensile strain as a function of duration, magnitude, and frequency. *Journal of Orthopaedic Research*, 29(8), 1275–1283. <http://doi.org/10.1002/jor.21388>
- Stains, J. P., & Civitelli, R. (2005). Gap junctions in skeletal development and function. *Biochimica et Biophysica Acta - Biomembranes*, 1719(1–2), 69–81. <http://doi.org/10.1016/j.bbamem.2005.10.012>
- Stokes, I. A., & Iatridis, J. C. (2004). Mechanical conditions that accelerate intervertebral disc degeneration: Overload versus immobilization. *Spine*, 29(23), 2724–2732.
- Suadicani, S. O., Flores, C. E., Urban-Maldonado, M., Beelitz, M., & Scemes, E. (2004). Gap junction channels coordinate the propagation of intercellular Ca²⁺ signals generated by P2Y receptor activation. *Glia*, 48(3), 217–229. <http://doi.org/10.1002/glia.20071>
- Sugawara, Y., Ando, R., Kamioka, H., Ishihara, Y., Honjo, T., Kawanabe, N., ... Yamashiro, T. (2011). The three-dimensional morphometry and cell-cell communication of the osteocyte network in chick and mouse embryonic calvaria. *Calcified Tissue International*, 88(5), 416–424. <http://doi.org/10.1007/s00223-011-9471-7>
- Taylor, A. F., Saunders, M. M., Shingle, D. L., Cimbala, J. M., Zhou, Z., & Donahue, H. J. (2006). Mechanically stimulated osteocytes regulate osteoblastic activity via gap junctions. *American Journal of Physiology: Cell Physiology*, 292(1), C545–C552. <http://doi.org/10.1152/ajpcell.00611.2005>
- Torre, O. M., Mroz, V., Bartelstein, M. K., Huang, A. H., & Iatridis, J. C. (2018). Annulus fibrosus cell phenotypes in homeostasis and injury: Implications for regenerative strategies. *Annals of the New York Academy of Sciences*, 1–18. <http://doi.org/10.1111/nyas.13964>
- Tsai, T. T., Cheng, C. M., Chen, C. F., & Lai, P. L. (2014). Mechanotransduction in intervertebral discs. *Journal of Cellular and Molecular Medicine*, 18(12), 2351–2360. <http://doi.org/10.1111/jcmm.12377>
- Tsantrizos, A., Ito, K., Aebi, M., & Steffen, T. (2005). Internal strains in healthy and degenerated lumbar intervertebral discs. *Spine*, 30(19), 2129–2137. <http://doi.org/10.1097/01.brs.0000181052.56604.30>
- Uda, Y., Azab, E., Sun, N., Shi, C., & Pajevic, P. D. (2017). Osteocyte mechanobiology. *Current Osteoporosis Reports*, 15(4), 318–325. <http://doi.org/10.1007/s11914-017-0373-0>
- van den Akker, G. G. H., Koenders, M. I., van de Loo, F. A. J., van Lent, P. L. E. M., Blaney Davidson, E., & van der Kraan, P. M. (2017). Transcriptional profiling distinguishes inner and outer annulus fibrosus from nucleus pulposus in the bovine intervertebral disc. *European Spine Journal*, 26(8), 2053–2062. <http://doi.org/10.1007/s00586-017-5150-3>

- Van Den Eerenbeemt, K. D., Ostelo, R. W., Van Royen, B. J., Peul, W. C., & Van Tulder, M. W. (2010). Total disc replacement surgery for symptomatic degenerative lumbar disc disease: A systematic review of the literature. *European Spine Journal*, 19(8), 1262–1280. <http://doi.org/10.1007/s00586-010-1445-3>
- Vatsa, A., Smit, T. H., & Klein-Nulend, J. (2007). Extracellular NO signalling from a mechanically stimulated osteocyte. *Journal of Biomechanics*, 40(1), S89-95. <http://doi.org/10.1016/j.jbiomech.2007.02.015>
- Vergari, C., Chan, D., Clarke, A., Mansfield, J. C., Meakin, J. R., & Winlove, P. C. (2017). Bovine and degenerated human annulus fibrosus: A microstructural and micromechanical comparison. *Biomechanics and Modeling in Mechanobiology*, 16(4), 1475–1484. <http://doi.org/10.1007/s10237-017-0900-z>
- Vergroesen, P.-P. A., Kingma, I., Emanuel, K. S., Hoogendoorn, R. J., Welting, T. J., van Royen, B. J., ... Smit, T. H. (2015). Mechanics and biology in intervertebral disc degeneration: A vicious circle. *Osteoarthritis and Cartilage / OARS, Osteoarthritis Research Society*, 23(7), 1057–1070. <http://doi.org/10.1016/j.joca.2015.03.028>
- Walter, B. A., Illien-Jünger, S., Nasser, P. R., Hecht, A. C., & Iatridis, J. C. (2014). Development and validation of a bioreactor system for dynamic loading and mechanical characterization of whole human intervertebral discs in organ culture. *Journal of Biomechanics*, 47(9), 2095–2101. <http://doi.org/10.1016/j.jbiomech.2014.03.015>
- Weber, J. F., & Waldman, S. D. (2014). Calcium signaling as a novel method to optimize the biosynthetic response of chondrocytes to dynamic mechanical loading. *Biomechanics and Modeling in Mechanobiology*, 13(6), 1387–97. <http://doi.org/10.1007/s10237-014-0580-x>
- Weber, K. T., Jacobsen, T. D., Maidhof, R., Virojanapa, J., Overby, C., Bloom, O., ... Chahine, N. O. (2015). Developments in intervertebral disc disease research: Pathophysiology, mechanobiology, and therapeutics. *Current Reviews in Musculoskeletal Medicine*, 8(1), 18–31. <http://doi.org/10.1007/s12178-014-9253-8>
- Weber, P. A., Chang, H. C., Spaeth, K. E., Nitsche, J. M., & Nicholson, B. J. (2004). The permeability of gap junction channels to probes of different size is dependent on connexin composition and permeant-pore affinities. *Biophysical Journal*, 87(2), 958–973. <http://doi.org/10.1529/biophysj.103.036350>
- Wenger, K. H., Woods, J. A., Holecek, A., Eckstein, E. C., Robertson, J. T., & Hasty, K. A. (2005). Matrix remodeling expression in anulus cells subjected to increased compressive load. *Spine*, 30(10), 1122–1126. <http://doi.org/10.1097/01.brs.0000162395.56424.53>
- Wu, Y., Xu, B., Yang, Q., Li, X., Zhang, Y., Ma, X., ... Zhang, Y. (2013). A novel natural ECM-derived biphasic scaffold for intervertebral disc tissue engineering. *Materials Letters*, 105, 102–105. <http://doi.org/10.1016/j.matlet.2013.04.040>

- Wynne-Jones, G., Cowen, J., Jordan, J. L., Uthman, O., Main, C. J., Glozier, N., & Van Der Windt, D. (2014). Absence from work and return to work in people with back pain: A systematic review and meta-analysis. *Occupational and Environmental Medicine*, 71(6), 448–458. <http://doi.org/10.1136/oemed-2013-101571>
- Yang, Q., Xu, H., Hurday, S., & Xu, B. (2016). Construction strategy and progress of whole intervertebral disc tissue engineering. *Orthopaedic Surgery*, 8(1), 11–18. <http://doi.org/10.1111/os.12218>
- Yellowley, C. E., Li, Z., Zhou, Z., Jacobs, C. R., & Donahue, H. J. (2000). Functional gap junctions between osteocytic and osteoblastic cells. *Journal of Bone and Mineral Research: The Official Journal of the American Society for Bone and Mineral Research*, 15(2), 209–217. <http://doi.org/10.1359/jbmр.2000.15.2.209>
- Zhang, Y., Drapeau, S., An, H. S., Markova, D., Lenart, B. A., & Anderson, D. G. (2011). Histological features of the degenerating intervertebral disc in a goat disc-injury model. *Spine*, 36(19), 1519–1527. <http://doi.org/10.1097/BRS.0b013e3181f60b39>
- Zhao, C. Q., Wang, L. M., Jiang, L. S., & Dai, L. Y. (2007). The cell biology of intervertebral disc aging and degeneration. *Ageing Research Reviews*, 6(3), 247–261. <http://doi.org/10.1016/j.arr.2007.08.001>

Appendix A: FLIP-Image-Set data

Table A.1: FLIP-image-set data

Sample Name ¹	Strain (%)	Experimental condition and imaging-plane orientation ²	Cell morphology	Target cell end-point intensity	Nearest neighbor end-point intensity	Responding fraction of total nearest neighbors	Responding fraction of total vertical neighbors	Intra-lamellar signal propagation	Elapsed time in tension (min)
May2B3	1	AGA-blocked gap junctions	Spindle-shaped lamellar	0.103	0.6403				55
May2B4	1	AGA-blocked gap junctions	Spindle-shaped lamellar	0.0391	0.5225				65
May2B5	1	AGA-blocked gap junctions	Interlamellar	0.1655	0.8149				77
May2B6	1	AGA-blocked gap junctions	Interlamellar	0.1064	0.7425				89
May2B7	1	AGA-blocked gap junctions	Round lamellar	0.0579	0.4658				98
May2B8	1	Non-bleached control	Interlamellar		1.074				105
May2B8	1	Non-bleached control	Interlamellar		0.9854				105
May2B8	1	Non-bleached control	Interlamellar		0.9568				105
May2B8	1	Non-bleached control	Interlamellar		0.9731				105
May2B9	1	Non-bleached control	Interlamellar		0.8775				113
May2B9	1	Non-bleached control	Interlamellar		0.9509				113
May2B9	1	Non-bleached control	Interlamellar		0.9876				113
May2B9	1	Non-bleached control	Interlamellar		0.9887				113
May2B9	1	Non-bleached control	Interlamellar		1.065				113
May2B10	1	AGA-blocked gap junctions	Spindle-shaped lamellar	0.0791	0.7358				128
May2B11	1	AGA-blocked gap junctions	Spindle-shaped lamellar	0.1172	0.8889				136
May2B12	1	AGA-blocked gap junctions	Round lamellar	0.0847	0.855				146
May2B13	1	AGA-blocked gap junctions	Spindle-shaped lamellar	0.0114	0.8015				156
May9A3	1	Non-bleached control	Interlamellar		0.67				44
May9A3	1	Non-bleached control	Interlamellar		0.7412				44

¹ Sample name decoding: “May2B3” means the oxtail was harvested on May 2, 2018; B is the second caudal disc (A–C corresponds to discs CC1–CC3, respectively, which were occasionally split into two parts [denoted with “ii”]); and 3 means the third FLIP image set of that sample.

² The imaging-plane orientation is assumed to be parallel to the annulus fibrosus lamellae as in Figure 3.2A unless noted as “perpendicular” in this column, which corresponds to the perpendicular orientation as in Figure 3.2B.

May9A3	1	Non-bleached control	Interlamellar		0.8326				44
May9A3	1	Non-bleached control	Interlamellar		0.8372				44
May9A3	1	Non-bleached control	Interlamellar		0.9454				44
May9A6	1	Open	Round lamellar	0.1236	0.7808	0 of 1			78
May9A8	1	Open	Interlamellar	0.0101	0.7493	1 of 1			94
May9A9	1	Open	Interlamellar	0.0132	0.6402	1 of 1			103
May9A10	1	Open	Interlamellar	0	0.3206	1 of 1			110
May9A11	1	Open	Interlamellar	0.0472	0.4673	1 of 1			118
May9A12	1	Open	Interlamellar	0.0247	0.6303	2 of 2			127
May9A13	1	Open	Interlamellar	0.0458	0.5621	2 of 2			134
May9A14	1	Open	Spindle-shaped lamellar	0.1604	0.2349	2 of 2		Excluded	167
May9Aii1	1	Open	Spindle-shaped lamellar	0.0522	0.0807	3 of 3		Both long. and lat.	34
May9Aii2	1	Open	Spindle-shaped lamellar	0.1043	0.3457	4 of 5		Both long. and lat.	43
May9Aii3	1	Open	Spindle-shaped lamellar	0.0018	0.1684	3 of 3		Both long. and lat.	52
May9Aii5	1	Open	Spindle-shaped lamellar	0.2061	0.5305	4 of 4		Both long. and lat.	68
May9Aii6	1	Open	Spindle-shaped lamellar	0.1532	0.3662	3 of 3		Both long. and lat.	77
May9Aii7	1	Open	Spindle-shaped lamellar	0.0694	0.2466	1 of 1		Excluded	86
May9Aii8	1	Open	Spindle-shaped lamellar	0.3836	0.776	0 of 1		Only target cell	94
May9Aii9	1	Open	Spindle-shaped lamellar	0.2942	0.5633	1 of 3		Longitudinal only	101
May9Aii10	1	Open	Spindle-shaped lamellar	0.0788	0.4332	1 of 2		Excluded	110
May9Aii11	1	Open	Interlamellar	0.2973	0.3058	3 of 3			118
May9Aii12	1	Open	Interlamellar	0.134	0.6116	2 of 2			126
May16A2	1	Open	Spindle-shaped lamellar	0.0868	0.5564	1 of 2		Excluded	76
May16A3	1	Open	Spindle-shaped lamellar	0.1466	0.6885	1 of 1		Excluded	85
May16A4	1	Open	Spindle-shaped lamellar	0.1511	0.7873	0 of 1		Excluded	93
May16A5	1	Open	Spindle-shaped lamellar	0.2621	0.5435	1 of 1		Excluded	101
May16A6	1	Non-bleached control	Interlamellar		0.6829				113
May16A6	1	Non-bleached control	Interlamellar		0.7079				113
May16A6	1	Non-bleached control	Interlamellar		0.724				113
May16A6	1	Non-bleached control	Interlamellar		0.7612				113
May16A6	1	Non-bleached control	Interlamellar		0.8143				113
May16A6	1	Non-bleached control	Interlamellar		0.8334				113
May16A7	1	Open	Spindle-shaped lamellar	0.0748	0.3909	2 of 2		Excluded	120

May16Aii2	1	Non-bleached control	Interlamellar		0.6597					35
May16Aii2	1	Non-bleached control	Interlamellar		0.721					35
May16Aii2	1	Non-bleached control	Interlamellar		0.7941					35
May16Aii2	1	Non-bleached control	Interlamellar		0.8465					35
May16Aii2	1	Non-bleached control	Interlamellar		0.9125					35
May16B3	1	AGA-blocked gap junctions	Round lamellar	0.0002	0.3366					51
May16B4	1	Non-bleached control	Interlamellar		0.6841					58
May16B4	1	Non-bleached control	Interlamellar		0.7643					58
May16B4	1	Non-bleached control	Interlamellar		0.8291					58
May16B4	1	Non-bleached control	Interlamellar		0.9953					58
May16B5	1	Non-bleached control	Round lamellar		0.6604					66
May16B5	1	Non-bleached control	Round lamellar		0.7154					66
May16B5	1	Non-bleached control	Round lamellar		0.9767					66
May16B7	1	Non-bleached control	Round lamellar		0.7286					82
May16B7	1	Non-bleached control	Round lamellar		0.7487					82
May16B7	1	Non-bleached control	Round lamellar		0.7966					82
May16B9	1	AGA-blocked gap junctions	Round lamellar	0.017	0.5318					98
May16C2	1	Open	Interlamellar	0.1939	0.608	1 of 1				57
May16C3	1	Open	Spindle-shaped lamellar	0.4072	0.68	2 of 2			Excluded	64
May16C4	1	Open	Spindle-shaped lamellar	0.1176	0.6428	2 of 2			Excluded	86
May16C5	1	Open	Interlamellar	0.3754	0.6971	2 of 2				94
May16C6	1	Open	Spindle-shaped lamellar	0.3004	0.314	3 of 3			Excluded	102
May24C1	1	AGA-blocked gap junctions	Interlamellar	0.1149	0.721					39
May24C2	1	AGA-blocked gap junctions	Interlamellar	0.1319	0.7464					48
May24C3	1	AGA-blocked gap junctions	Interlamellar	0.4654	0.91					58
May24Cii1	1	AGA-blocked gap junctions	Spindle-shaped lamellar	0.0551	0.3062					34
May24Cii2	1	AGA-blocked gap junctions	Spindle-shaped lamellar	0.0095	0.5588					42
Jul23A1	1	Open perpendicular	Round lamellar	0.0087	0.1249	3 of 4	2 of 2			41
Jul23A2	1	Open perpendicular	Spindle-shaped lamellar	0.0025	0.04	3 of 3	3 of 3			70
Jul23A3	1	Open perpendicular	Spindle-shaped lamellar	0.3358	0.5863	2 of 2	2 of 2			82
Jul23A4	1	Open perpendicular	Spindle-shaped lamellar	0.0959	0.3595	2 of 2	2 of 2			90
Jul23A5	1	Open perpendicular	Spindle-shaped lamellar	0.0065	0.4491	2 of 2	1 of 1			99
Jul23A7	1	Open perpendicular	Spindle-shaped lamellar	0.2875	0.6824	3 of 3	1 of 1			115

Jul23A8	1	Open perpendicular	Spindle-shaped lamellar	0.1735	0.7176	0 of 4	0 of 1		125
Jul23B1	1	Open perpendicular	Interlamellar	0.1236	0.382	1 of 3	0 of 1		70
Jul23B3	1	Open perpendicular	Interlamellar	0.1129	0.7078	0 of 2	0 of 2		89
Jul23B5	1	Open perpendicular	Interlamellar	0.222	0.488	0 of 1	0 of 1		108
Jul23B6	1	Open perpendicular	Spindle-shaped lamellar	0.341	0.565	3 of 3	2 of 2		116
Jul23B8	1	Open perpendicular	Spindle-shaped lamellar	0.0956	0.2796	2 of 2	2 of 2		133
Jul23C1	1	Open perpendicular	Round lamellar	0.079	0.366	2 of 2	2 of 2		58
Jul23C2	1	Open perpendicular	Round lamellar	0.1352	0.501	2 of 2	2 of 2		67
Jul23C3	1	Open perpendicular	Spindle-shaped lamellar	0.02	0.106	2 of 2	1 of 1		76
Jul23C4	1	Open perpendicular	Round lamellar	0.2304	0.5864	1 of 1	1 of 1		83
Jul23C6	1	Open perpendicular	Spindle-shaped lamellar	0.122	0.506	1 of 2	1 of 2		109
May30A1	5	Open	Spindle-shaped lamellar	0.0218	0.3271	1 of 1		Excluded	36
May30A2	5	Open	Spindle-shaped lamellar	0.0016	0.132	1 of 1		Excluded	44
Jun7B1	5	Open	Interlamellar	0.0189	0.1289	3 of 3			34
Jun13A1	5	Open	Spindle-shaped lamellar	0.0637	0.3196	1 of 1		Excluded	30
Jun13A2	5	Open	Round lamellar	0.0343	0.2675	2 of 2			38
Jun13A3	5	Open	Interlamellar	0.005	0.1795	3 of 3			46
Jun13A4	5	Open	Round lamellar	0	0.2092	3 of 3			53
Jun13A5	5	Open	Spindle-shaped lamellar	0.0239	0.3141	3 of 3		Excluded	62
Jun13A6	5	Open	Spindle-shaped lamellar	0.1023	0.4872	2 of 2		Excluded	69
Jun13A7	5	Open	Interlamellar	0.1478	0.3535	4 of 4			77
Jun13A8	5	Open	Interlamellar	0.2389	0.4036	2 of 2			85
Jun13A9	5	Open	Interlamellar	0.0234	0.5084	3 of 4			92
Jun13A11	5	Open	Interlamellar	0.0458	0.5408	2 of 2			109
Jun13A12	5	Open	Interlamellar	0.1832	0.6031	2 of 2			116
Jun13A13	5	Open	Spindle-shaped lamellar	0.0752	0.4099	2 of 2		Excluded	125
May30B2	10	Open	Round lamellar	0.08556	0.2206	1 of 1			40
May30B3	10	Open	Round lamellar	0.0154	0.3839	0 of 1			49
May30B4	10	Open	Round lamellar	0.0007	0.3343	1 of 1			57
May30B5	10	Open	Spindle-shaped lamellar	0.1316	0.3521	2 of 2		Excluded	65
May30B6	10	Open	Spindle-shaped lamellar	0.0009	0.0741	1 of 1		Excluded	73
May30B7	10	Open	Interlamellar	0.0063	0.1548	2 of 2			84
May30B8	10	Open	Spindle-shaped lamellar	0	0.2025	3 of 3		Both long. and lat.	96
Jun13A14	10	Open	Spindle-shaped lamellar	0.0681	0.206	1 of 1		Excluded	39

Jun13A15	10	Open	Spindle-shaped lamellar	0.2517	0.6519	4 of 4		Both long. and lat.	48
Jun13A17	10	Open	Interlamellar	0.0143	0.5403	1 of 2			67
Jun13A18	10	Open	Interlamellar	0.007	0.5878	2 of 2			74
Jun13A19	10	Open	Round lamellar	0	0.4957	2 of 2			82
Jun13A20	10	Open	Interlamellar	0.0132	0.5498	1 of 1			90
Jun13A21	10	Open	Round lamellar	0.0079	0.5232	1 of 1			98
Jun13A22	10	Open	Interlamellar	0.0814	0.4793	1 of 2			106
Jun13A24	10	Open	Interlamellar	0.3275	0.601	2 of 2			122
Jun7A5	15	Open	Round lamellar	0.0139	0.6006	1 of 1			70
Jun7A7	15	Open	Spindle-shaped lamellar	0.0418	0.1475	1 of 1		Excluded	88
Jun7A10	15	Open	Round lamellar	0.0355	0.2041	3 of 3			114
Jun7A11	15	Open	Interlamellar	0.0723	0.3226	4 of 4			122
Jun7A12	15	Open	Round lamellar	0.0977	0.3186	3 of 3			130
Jun7A13	15	Open	Interlamellar	0.0074	0.4211	1 of 1			138
Jun7A14	15	Open	Spindle-shaped lamellar	0.0757	0.1987	2 of 2		Excluded	147
Jun7A15	15	Open	Spindle-shaped lamellar	0.068	0.2575	3 of 3		Both long. and lat.	155
Jun7A16	15	Open	Spindle-shaped lamellar	0.1522	0.288	3 of 3		Both long. and lat.	163
Jun7A17	15	Open	Spindle-shaped lamellar	0	0.1838	1 of 1		Excluded	170
Jun13C1	20	Open	Interlamellar	0.3228	0.3898	3 of 3			77
Jun13C2	20	Open	Interlamellar	0.2104	0.3399	3 of 3			85
Jun13C3	20	Open	Interlamellar	0.1612	0.4428	1 of 1			92
Jun13C4	20	Open	Spindle-shaped lamellar	0.3024	0.4936	1 of 1		Both long. and lat.	99
Jun13C5	20	Open	Interlamellar	0.1164	0.5254	3 of 3			106
Jun13C6	20	Open	Interlamellar	0.3767	0.6192	1 of 3			114
Jun13C7	20	Open	Round lamellar	0.2336	0.708	0 of 2			122
Jun13C8	20	Open	Interlamellar	0.2975	0.3133	2 of 2			130
Jun13C9	20	Open	Interlamellar	0	0.682	0 of 1			137
Jun13C10	20	Open	Interlamellar	0.0388	0.6719	0 of 1			145
Jun13C11	20	Open	Interlamellar	0.4481	0.7085	3 of 3			153
Jun13C14	20	Open	Interlamellar	0.0645	0.3247	3 of 3			178
Jun13C15	20	Open	Interlamellar	0.0725	0.305	3 of 3			185
Jun13C16	20	Open	Interlamellar	0.02189	0.35	3 of 3			193
Jun20A2	25	Open	Spindle-shaped lamellar	0.1166	0.1647	3 of 3		Excluded	51
Jun20A6	25	Open	Spindle-shaped lamellar	0.2512	0.323	4 of 5		Both long. and lat.	94

Jun20A7	25	Open	Spindle-shaped lamellar	0.0836	0.2589	3 of 3		Excluded	101
Jun20A9	25	Open	Round lamellar	0.0999	0.5436	0 of 4			120
Jun20A10	25	Open	Round lamellar	0.2185	0.2635	3 of 4			128
Jun20B5	25	Open	Spindle-shaped lamellar	0.2158	0.478	1 of 3		Excluded	104
Jun20B6	25	Open	Interlamellar	0.287	0.3474	3 of 3			112
Jun20B7	25	Open	Interlamellar	0.3852	0.3957	5 of 5			120
Jun20B8	25	Open	Spindle-shaped lamellar	0.1634	0.1763	3 of 4		Excluded	127
Jun20B10	25	Open	Spindle-shaped lamellar	0.3192	0.5118	2 of 3		Both long. and lat.	142